University of Strathclyde Glasgow

TOWARDS AN ENDOSCOPIC CAPSULE FOR THE DETECTION OF GASTROINTESTINAL BLEEDING: SPECTROSCOPIC SENSING AND OPTICAL DATA COMMUNICATIONS

Submitted by **Maria Katsafadou**

Department of Biomedical Engineering

University of Strathclyde, Glasgow

August 28, 2023

Declaration Of Author's Rights

This thesis is the result of the author's original research. It has been composed by the author and has not been previously submitted for examination which has led to the award of a degree.

Signed: 

Date: 28th August 2023

List of Publications

Conference Papers

July 2022 **Source Multiplexing Enhances the Number of Channels of a Multispectral Sensor**

Katsafadou, M. & Giardini, M. E., 2022, 44th Annual International Conference of the IEEE Engineering in Medicine and Biology Society (EMBC), Glasgow, UK, 2022

[Contribution: contributed to the design of the experiment; designed, fabricated, and assembled equipment; created the samples; 3D designed and printed the setup used; performed the measurements; contributed to data analysis; contributed to manuscript]

Conference Single Page Abstracts/Posters

July 2019 **Optical Communication Through Tissue**

Katsafadou, M. & Giardini, M. E., 2019, 41st Annual International Conference of the IEEE Engineering in Medicine and Biology Society (EMBC), Berlin, Germany, 2019

[Contribution: contributed to the design of the experiment; designed and soldered used PCBs; designed and fabricated tissue phantom; contributed to Monte Carlo coding; run the Monte Carlo simulations]

April 2019 **Spectroscopic Capsule Technology for the Detection of Gastrointestinal Bleeding**

Katsafadou, M., 2019, Annual Medical Research of Scotland Researcher Development Event, Perth, UK, 2019

[Contribution: contributed to the design of the experiment; designed and soldered the used PCBs; contributed the C++ code used; created the used samples; run experiments with external spectrophotometer; analysed the results; created the graphs]

Abstract

Introduction:

Gastrointestinal (GI) bleeding is a common and potentially life-threatening condition that necessitates prompt diagnosis and intervention. While endoscopy remains the gold standard for detecting GI bleeding, it has limitations, notably its inability to reach the small intestine, where critical bleeding may be missed. In 1981, Gavriel Iddan's introduction of the wireless camera pill revolutionized gastroenterology by enabling comprehensive imaging of the entire GI tract. Despite advancements, existing wireless capsules primarily rely on optical sensors limited to two wavelengths, restricting their ability to detect various substances. Furthermore, the communication system using radio frequency (RF) faces bandwidth constraints, hindering data transfer capabilities.

Methods:

This PhD thesis aimed to enhance both the sensing and communication systems of wireless capsule endoscopes. The first objective was the development of an optical sensor with a higher optical channel count than existing capsule-based devices. This is a necessary step for detecting a broader range of substances within the GI tract. The second objective was the development of an optical communication link with high bandwidth. To assess the feasibility of the proposed optical communication system, theoretical simulations were performed to estimate the data transmission rates achievable through biological tissue. Additionally, practical bench tests were conducted using phantoms and biological tissue to evaluate the performance of the new optical communication system.

Results:

The multi-wavelength optical sensor was successfully developed, offering the ability to sense a wider spectrum of wavelengths compared to traditional

systems. In addition to the spectrometer's capabilities, separate theoretical simulations indicated that optical communication could support higher data transmission rates than RF communication. Experimental testing further demonstrated that the optical system was capable of transmitting data through biological tissue at a data rate of up to 12 Mbps. Furthermore, the optical communication system successfully transmitted an uncompressed colour image with a data rate of up to 1 Mbps, demonstrating its potential for high-quality image transmission from the capsule to external receivers.

Discussion:

The results indicate that the number of channels and bandwidth of a multi-wavelength optical sensor can indeed be improved. This shows promise to enhance the diagnostic capabilities of wireless capsule endoscopes. By expanding the range of detectable wavelengths, the new system provides detection with higher specificity. Moreover, the successful implementation of optical communication addresses the limitations of RF communication, enabling faster data transmission and the possibility of real-time high-resolution image delivery. The main limitation of the thesis is that the work is only qualitative, and no reference tests exist to demonstrate the capabilities quantitatively. Future work will need to define reference tasks, test the system under these tasks, and under clinical conditions.

Funding

This thesis has been cofounded by Medical Research of Scotland (grant agreement no. PhD-1048-2016) and Ovesco Endoscopy AG, Germany.

Preface/Acknowledgments

I would initially like to thank my primary supervisor, Dr Mario Ettore Giardini, for his continuous help and guidance through the whole process of this PhD. From the initial days that he explained in detail electronic circuits and programming until now with the writing of this thesis, his continued help and contribution have been extremely valuable. Furthermore, I would also like to thank my second supervisor, Dr Damion Corrigan for supporting me with his knowledge in biology during this project. Additionally, I would like to express my gratitude to Dr Sebastian Schostek, Vice President of Ovesco Endoscopy AG. His help, support and knowledge around capsule endoscopes have been valuable. Ovesco and Medical Research of Scotland funded this project, and I would like to thank them both for all their financial support during these 5 years.

I would also like to thank all the lab members with whom I worked with during these years of my research. It was great to daily work with all of them and to always have someone to talk to during the bad and good days of our projects.

Moreover, I would like to thank my husband Petros, who has been really supportive through these demanding years of doing a PhD. Also, my amazing daughter Nephele and my son Panayiotis for brightening every day of my life.

Finally, I would like to thank my father, mother, and twin sister for always being there for me, believing in me and supporting me through all the years of my life, from my Bachelor towards the fulfilment of this PhD.

IMPACT OF COVID

The Covid pandemic has significantly impacted this project. The initial project plan entailed designing a sensor that would be then encapsulated into a single unit and afterwards to progress with animal testing. My PhD was a collaboration between the University of Strathclyde and Ovesco Endoscopy AG, a medical device company based in Tuebingen Germany that operates in the field of endoscopy. OVESCO had all the necessary facilities and partners to support us with that animal testing that was planned to be conducted in Germany.

However, the onset of COVID-19 brought about significant disruptions. The pandemic led to prolonged periods during which the laboratories were inaccessible, severely impacting my experimental work. Additionally, Brexit introduced uncertainties in the regulatory landscape for conducting overseas animal experiments. These combined factors meant that significant delays were introduced in the experimental work in Scotland and that the planned animal testing in Germany could not be carried out, resulting in the non-fulfilment of these specific aims.

In response to these challenges, we pivoted our approach. Instead of the original plan, a tethered capsule has been developed. This alternative solution allowed us to demonstrate the capsule's performance by successfully transmitting images through a human finger, hand, and arm. Furthermore, instead of doing animal work in Germany, only simulations were able to be run to evaluate the feasibility of the created system. Despite the setbacks, these achievements marked a significant milestone in our research, showcasing the potential of the tethered capsule in practical applications.

Table of Contents

List of Figures

List of Tables

List of Abbreviations

3D	Three-Dimensional
ASIC	Application Specific Integrates Circuits
BER	Bit Error Rate
CAD	Computer-Aided Design
CE	Capsule Endoscope
CMOS	Complementary Metal Oxide Semiconductor
CT	Computed Tomography
DBE	Double Balloon Enteroscopy
EGD	Oesophageal Gastroduodenoscopy
FDA	Food and Drug Administration
FFT	Fast Fourier Transform
GI	Gastrointestinal
LEDs	Light-Emitting Diodes
LGIB	Lower Gastrointestinal bleeding
LVTTL	Low Voltage Transistor-Transistor Logic
MC	Monte Carlo
MRI	Magnetic Resonance Imaging
OGIB	Obscure Gastrointestinal Bleeding
PCB	Printed Circuit Board
RGB	Red Green and Blue
RF	Radio Frequencies
TTL	Transistor-Transistor Logic
UGIB	Upper Gastrointestinal bleeding
VLC	Visible Light Communication
WCE	Wireless Capsule Endoscopy

CHAPTER 1

INTRODUCTION

Gastrointestinal (GI) bleeding is a common and serious clinical problem affecting over 85,000 people each year in the UK and 300,000 in the USA *(Sebastian et al., 2016), (Zuckerman et al., 1998)*. From these cases, approximately 4,000 result in patient mortality. In the following subchapters, a brief anatomy of the GI tract is presented, followed by the causes of bleeding in the GI tract. Then, various techniques used to sense this blood are analysed together with the more recent evolution of this sensing by capsule sensors. Finally, data transmission methods used by these capsule sensors are examined. At the end of the Chapter, the thesis aims, objectives and structure are stated.

1.1. Anatomy of the Gastrointestinal Tract

The digestive system is made up of the digestive tract, also known as GI tract and a variety of accessory organs. The initial part of the GI tract comprises of organs like the oral cavity (mouth) and the pharynx. The rest of the tract can be subdivided into an upper and a lower section. The major organs in the upper GI tract are the oesophagus, stomach, and the upper portion of the small intestine (duodenum). The lower portion of the GI tract includes the lower part of the small intestine, the large intestine and the anus *(Peura, 2020)*. The accessory organs that constitute the digestive system are the teeth, tongue, salivary glands, liver, gallbladder and pancreas *(Martini et al., 2015, Hartwig, 2008)*. A clear visualisation of the main organs of the digestive system is illustrated in Figure 1.1.

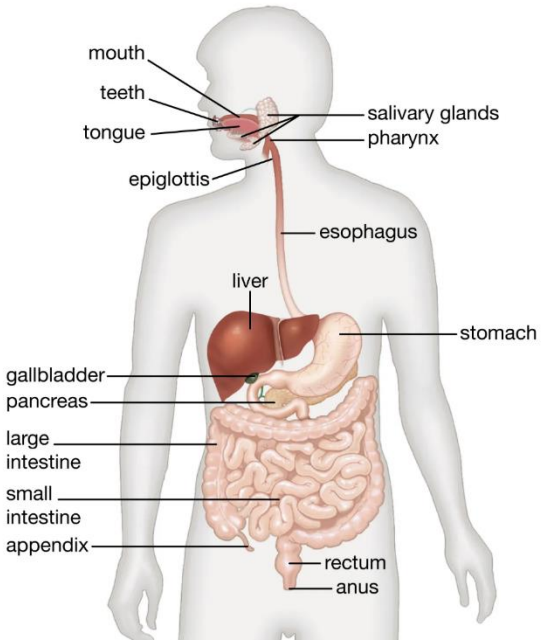

Figure 1.1. The digestive system (Keeton et al., 2023)

The main functions of the digestive system can be grouped under six main categories:

- Ingestion which is the active process taking place when food and water enter the oral cavity.
- Mechanical processing which is the process of breaking the food down into smaller particles in order to move easier along the gastrointestinal tract.
- Digestion is the chemical break down of food by different enzymes produced by the digestive system.
- Secretion takes place when water, enzymes and salts are released by the digestive tract.
- Absorption is the process happening when vitamins, electrolytes and other organic small molecules resulting from digestion, move into the digestive tract's interstitial fluid.
- Excretion is the elimination of wastes from the human body *(Martini et al., 2015), (Seeley et al., 2001), (Waugh et al., 2001), (Mader et al., 2004).*

As abovementioned, the digestive tract consists of a variety of organs and each one of them is specifically designed for a different function. However, nearly all of them, are composed of four layers, and more specifically from the inside to the outside of the tract the layers are the mucosa, the submucosa, the muscularis (including the circular and the longitudinal muscle layers) and the adventitia or serosa or peritoneum (*Martini et al., 2015), (Seeley et al., 2001)*. These four layers are illustrated in Figure 1.2.

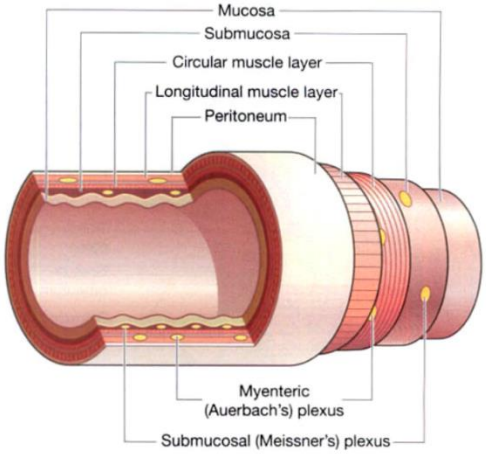

Figure 1.2. General Structure of the gastrointestinal tract (Waugh et al., 2001)

The oral cavity is the first part of the digestive tract. The lips and cheeks are its external boundaries while internally it contains the teeth and tongue. The lips are muscular structures that are covered by skin. Their epithelium layer is thin, almost transparent, and thus their underlying blood vessels are easily visible

leading to their characteristic pink appearance. The lateral walls of the mouth are formed by the cheeks which are supported by layers of fat and the buccinator muscles. Both lips and cheeks are important structures in the process of chewing food, which is also called mastication. They facilitate this procedure by holding the food into place while the teeth crush it. This is the beginning of the mechanical digestion function of the gastrointestinal tract. Furthermore, these two structures play an important role in the speech process by assisting in the formation of words *(Martini et al., 2015), (Seeley et al., 2001), (Mader et al., 2004).*

The internal parts of the oral cavity are the tongue and teeth. The tongue is composed by skeletal muscle, and it occupies the biggest part of the oral cavity. It is attached to the mouth mainly in the posterior part of it and in the anterior by a thin fold of tissue, the frenulum. Its main functions are to manipulate the food inside the oral cavity; to use its sensory receptors to taste food and it is also the most important organ for the speech. Teeth are 32 in number, and they are composed by a mineralized matrix like the one of bones. Teeth are held in their place by ligaments called periodontal (*Martini et al., 2015), (Seeley et al., 2001), (Mader et al., 2004).*

The next part of the gastrointestinal tract is the pharynx or throat. It is a 12 cm long tube between the mouth and the oesophagus, and it consists of three different parts, the nasopharynx, oropharynx and laryngopharynx. The first part is important for the respiration while the other two for digestion. Blood is supplied to pharynx through a variety of branches of the facial arteries. The oesophagus is a muscular tube that joins pharynx with stomach. It is about 25 cm long; its diameter is 2 cm, and it is located behind the trachea and the heart. Food is transferred through the oesophagus by peristalsis which is the rhythmic contraction that facilitates this transfer. Sphincters are muscles located in the upper and lower parts of the oesophagus that act like valves in order to regulate food's movement. The upper sphincter prevents the passage of air into the oesophagus while the lower one (cardiac sphincter) prevents the

reflux of the acid gastric contents of the stomach into the oesophagus. This last procedure is also assisted by the shape oesophagus' last part which curves upwards in order to prevent this reflux *(Martini et al., 2015), (Seeley et al., 2001), (Waugh et al., 2001), (Mader et al., 2004), (Leonhardt et al., 1986).*

The stomach is the J-shaped organ that is connected with the oesophagus by the cardiac sphincter and with the duodenum by the pyloric sphincter. Its length is around 25 cm and its diameter varies according to the amount of food it contains. It has two curvatures, the lesser which is 10 cm long and the long greater curvature which is approximately 40 cm long. The stomach is divided into four main regions, the cardia, which is near the heart, the fundus, which is responsible for holding food temporarily, the body, which is the main part of the stomach and the pylorus, the area leading to the pyloric sphincter and the duodenum. The stomach's wall is comprised of three muscular layers: an outer longitudinal layer, a middle circular layer and an inner oblique layer. These layers produce a churning motion in the stomach which assists the process of digestion *(Martini et al., 2015), (Seeley et al., 2001), (Hartwig, 2008), (Waugh et al., 2001), (Mader et al., 2004)*.

As above-mentioned, the diameter of the stomach varies depending on the volume of food it contains, with a maximum capacity of 4 litres. The stomach acts on the food chemically by producing gastric juice by its gastric glands. There is a daily secretion of 2 litres of this fluid which consists of pepsinogen, HCl and mucus. The HCl is the reason the stomach has an acidic pH of 1.5-2, something beneficial in the process of killing any bacteria existing in the food. In the rare case this HCl acid penetrates the thick layer that protects the wall of the stomach, then the wall starts to break down and an ulcer can be created. Gastric juice is constantly present in the stomach in different amounts. The maximum secretion is reached around 1 hour after swallowing the food and the minimum after approximately 4 hours. After the process of breaking down the food inside the stomach through the gastric juice, the food reaches the

small intestine *(Martini et al., 2015), (Seeley et al., 2001), (Waugh et al., 2001), (Mader et al., 2004), (Leonhardt et al., 1986)*.

The small intestine is 4-6 m long starting from the pyloric valve of the stomach with a diameter of 4 cm until the ileocecal valve of the large intestine with diameter of 2.5 cm. It consists of the duodenum (25 cm long), jejunum (1-2.5 m long) and ileum (2-3.5 m long). In the small intestine, the main processes that take place are the final steps of food's chemical digestion and the absorption of nutrients. The surface area of the small intestine is almost as big as a tennis court. This is achieved by the existence of circular folds, villi and microvilli. Circular folds are folds of the mucosa and submucosa, permanently existing in the intestine. The small intestine contains approximately 800 circular folds. Villi are tiny finger-like projections of the mucosa into small intestine's lumen. They are 0.5 to 1.5 mm long. Their walls consist of columnar epithelial cells which have thousands of tiny extensions called microvilli (1 μm long). A variety of digestive enzymes lodge in the microvilli and together with pancreatic juice, bile and intestinal juice they complete the process of chemical digestion *(Martini et al., 2015), (Seeley et al., 2001), (Waugh et al., 2001), (Mader et al., 2004), (Leonhardt et al., 1986)*.

The digestive process is completed in this part of the gastrointestinal tract. The small intestine receives pancreatic juice from the pancreas and bile from the liver and more specifically the gallbladder. Pancreatic juice consists of water, mineral salts and enzymes and it has an alkaline pH of 8. Bile consists of water, mineral salts, mucus, bile salts, bilirubin (bile's pigment) and cholesterol. Liver secretes 500-1000 ml of bile daily with a pH of 8. Intestinal juice arrives in the small intestine by osmosis through the mucosa or is secreted by intestinal glands. Its pH is alkaline (pH of 7.8). When the acids of the stomach enter the duodenum, they get mixed with the pancreatic juice, the bile and the intestinal juice and the result is a neutral pH between 6 and 8. After the finalisation of the digestion process, the nondigested remains move to the next part of the

gastrointestinal tract, the large intestine, through peristaltic movements *(Martini et al., 2015), (Waugh et al., 2001), (Mader et al., 2004)*.

The large intestine is about 1.5 m long with a diameter of 6.5 cm. It includes the cecum (13 cm long), the colon (1.1 m long), the rectum (13 cm long) and the anal canal (3.8 cm long). The basic four-layer structure described at the beginning of this subchapter exists in the cecum, rectum and anal canal. The colon has a slightly different structure. Its longitudinal muscle fibres are formed into three bands that correspond to the mucosa layer of the other segments of the gastrointestinal tract. These bands of tissue are shorter than the total colon's length and thus they provide a puckered appearance to it. The two main functions of the large intestine are the absorption of food's water, a process that starts at the small intestine and the movement of masses by a wave of strong peristaltic contractions *(Martini et al., 2015), (Waugh et al., 2001), (Mader et al., 2004)*.

1.2. Bleeding in the Gastrointestinal Tract

Gastrointestinal bleeding can occur either in the upper (UGIB) or in the lower (LGIB) part of the gastrointestinal tract *(Whelan et al., 2010)*. The mortality rate for people suffering with UGIB is 6-10% while for people suffering with LGIB it drops to 4% *(Gómez et al., 2011)*. Furthermore, bleeding from the UGIB is four times more common compared to bleeding from the lower part *(Whelan et al., 2010)*. Consequently, UGIB is more severe and common. Both can be divided into chronic (which is light bleeding, continuing over an extended period of time and requires extensive examination to determine its cause) and acute (which is severe, sudden bleeding that can be easily located) *(Gómez et al., 2011)*.

Annually, worldwide there are 100-200 cases per 100,000 of adult population that suffer from UGIB *(Zuckerman et al., 1998)*. This is defined as bleeding from a source close to the Treitz ligament (located in the suspensory muscle of the first part of the small intestine). The main signs of bleeding in the UGIB include

vomit with blood and haematochezia which is the appearance of blood in the stool. In patients with severe blood loss, further symptoms are tachycardia, hypotension and dizziness. When the blood loss is mild, over a prolonged period of time, then additional symptoms are anaemia, malaise, changes in the pulse and blood pressure and even death *(Peura, 2020), (Sung et al., 2012)*.

The statistics for bleeding in the LGIB are lower but still alarming. Annually, there are 21-27 cases per 100,000 of adult population that suffer from LGIB worldwide *(Zuckerman et al., 1998)*. It is defined as bleeding from a source distal to the Treitz ligament. Signs of bleeding in the lower digestive part are haematochezia, black stool or dark blood in the stool. Generally, lower GI bleeding is found more often in men than women and its rate increases with age *(Zuckerman et al., 1998)*. Furthermore, LGIB is less severe compared to UGIB and patients tend to have higher haemoglobin, need fewer transfusions of blood and are more hemodynamically stable *(Sung et al., 2012)*.

Gastrointestinal bleeding is also an alarming problem in infants and children. When it is minor, it can be self-limited due to the robust physiology of children and their small total blood volume *(Bhanu Pillai et al., 2008)*. However, there are times that GI bleeding can be life-threatening. When the symptoms are intensive, immediate evaluation needs to take place in order to estimate the urgency of the situation. The stool and vomit of the child need to be tested for blood. When the child has hematemesis then the source of bleeding is in the upper GI tract, while when it presents blood in the stool then the source is usually the lower GI tract. Further symptoms of GI bleeding are a drop in the haematocrit of more than 10%, tachycardia or orthostatic changes *(Bhanu Pillai et al., 2008), (Fox, 2000)*.

1.2.1. Causes of Bleeding in the Gastrointestinal Tract

Bleeding in the whole gastrointestinal tract is a common problem that, according to the severity of its symptoms, requires immediate attention. Bleeding can occur in any part of the gastrointestinal system. Generally, causes

of bleeding are common to both adults and children. However, some lesions like necrotizing enterocolitis and allergic colitis appear only in children. Furthermore, causes of bleeding change according to the age of the child. The main causes of GI bleeding in neonatal (less than 1 month old) are swallowed maternal blood, gastritis, oesophagitis, gastroduodenal ulcer, coagulopathy, vascular anomaly and haemorrhagic disease (caused by vitamin K deficiency) *(Bhanu Pillai et al., 2008), (Fox, 2000)*.

The main causes of bleeding in adults in the upper part of the GI tract are presented in Table 1.1. In infants and adolescent main causes are similar with the ones of adults. In children, bleeding can also occur due to varioloform gastritis, ruptured pancreatic pseudocyst, mastocytosis, foreign body injury and Munchausen's syndrome by proxy *(Bhanu Pillai et al., 2008), (Fox, 2000)*.

Table 1.1. Causes of UGIB (Whelan et al., 2010), (Palmer, 2002), (Seddik et al., 2017), (Wilkins et al., 2012), (Gralnek et al., 2015)

Cause	**Percentage of Total Cases (N=180) of UGIB Reviewed**
Peptic ulcer	35-50%
Gastroduodenal erosions	8-15%
Oesophagitis	5-15%
Varices	5-10%
Mallory Weiss tear	15%
Vascular malformations	5%
Gastric cancer	3%
Malignant tumour	2%
Other	5%

In 16-20% of these UGIB cases, more than one cause may be identified as the source of patient's bleeding *(Gralnek et al., 2015)*. It can be noticed that the most common cause of UGIB is peptic ulcers. These are defined as wounds in the

gastrointestinal wall. The main difference between ulcers and erosions are their size (ulcers are deeper compared to erosions). The bacterium helicobacter pylori is one of the main factors leading to the creation of both of these lesions *(Van Leerdam et al., 2008)*. Bleeding in 90% of the patients with ulcers stops by the time the person reaches the hospital. However, if appropriate treatment is not given to the patient, bleeding will re-occur in 30-50% of them *(Sung et al., 2012)*. Duodenal ulcers are more common compared to gastric ulcers, but the symptoms are common to both of them *(Kim et al., 2012)*.

Oesophagitis occurs when the muscle that exists between the oesophagus and the stomach does not close properly, leading to stomach's gastric juice to flow back to the oesophagus *(Peura et al., 2020)*. Oesophageal varices are varices located at the lower part of the oesophagus that can be ruptured, leading to massive bleeding. These varices are present in 50% of patients with hepatic cirrhosis and bleeding occurs at 15% of them *(Peura et al., 2020), (Kim et al., 2012)*. Finally, Mallory Weiss tears are the third most common cause of UGIB. They are longitudinal tears in the oesophagus' lining resulting from increased pressure in the abdomen due to coughing, vomiting, hiatal hernia or childbirth *(Peura et al., 2020)*.

The main causes of bleeding in the lower part of the digestive system are presented in Table 1.2.

Table 1.2. Causes of LGIB (Whelan et al., 2010), (Vernava et al., 1997)

Cause	**Percentage of Total Cases (N=187) of LGIB Reviewed**
Diverticular disease	40 %
Inflammatory bowel disease	21 %
Neoplasia	14 %
Coagulopathy	12 %
Benign anorectal disease	11 %

Arteriovenous malformation	2 %

Diverticular disease is the most common cause of LGIB. It occurs by the creation of diverticula, which are pockets formed in the colon's wall and appear to people as they get older. Bleeding's severity in patients with diverticular disease varies from minor spotting to severe haematochezia. Inflammatory bowel diseases include Crohn's disease and colitis (ulcerative, infectious or ischemic). As the name states, they are inflammations of the colon. The most common symptom of these diseases is bloody diarrhoea. Most of the times, bleeding occurring from these diseases is not life-threatening and more than 50% of patients' bleeding stops spontaneously. However, there is a 35% chance of rebleeding to occur. Neoplasia (the uncontrolled growth of abnormal cells in the body) is the third most common cause of LGIB, and it includes benign adenomatous polyps (benign growths in the colon) and adenocarcinoma. Coagulopathy is a disease where the blood is unable to coagulate. Finally, benign anorectal disease includes haemorrhoids (enlarged veins of the anus or rectum that can be raptured), anal fissure (tears in the anus), fistula-in-ano and varices *(Peura et al., 2020), (Vernava et al., 1997)*.

The discrimination of gastrointestinal bleeding is mostly emphasized in the upper and lower parts of the gastrointestinal tract. However, the form of bleeding presentation divides GI bleeding further into visible and nearly undetectable. Furthermore, there is another subcategory, obscure gastrointestinal bleeding (OGIB). This occurs in approximately 5% of the cases and it is persistent bleeding which cause cannot be easily identified *(Bresci et al., 2009).* Obscure gastrointestinal bleeding is in most cases located in the small bowel *(Sung et al., 2012)*. It can be subdivided into overt which is bleeding occurring as vomiting of blood, either fresh (hematemesis) or black and as blood in the stool (haematochezia) *(Gómez et al., 2011)* and into occult which is bleeding that can only be identified by tests that can detect anaemia

of the patient (due to severe blood loss) or blood in the stool *(Rockey et al., 1999)*.

1.3. Sensing Blood in the Gastrointestinal Tract

Bleeding in the gastrointestinal tract is an important and complex problem and it represents one of the most common complications of the digestive tract. A great variety of gastrointestinal diseases have bleeding as a consequence. Generally, blood has different colour (from light to darker red) and not a specific texture or shape. This diversity is dependent on the time of bleeding, the type of disease and other conditions *(Suman et al., 2017)*. Thus, it is of great importance to be able to detect this bleeding as accurately and early as possible. There is a great variety of diagnostic procedures for identifying the source of bleeding, such as traditional endoscopy, enteroscopy, colonoscopy, angiography. These techniques are going to be analysed in this subchapter.

1.3.1 Traditional Endoscopy

The first attempt to visualise the interior of the body has been made by Bozini in 1805 where he used a tin tube and a candle reflecting light to a mirror to illuminate the inside of the human body. This device was called lichtleiter (light conductor) and it was used to test the urethra, urinary bladder and vagina *(Chandrasekhara et al., 2019)*. Traditional endoscopy was firstly introduced in 1853 by Antoine Jean Desormeaux, who is also known as the 'father of endoscopy' *(Mendoza-Trejo et al., 2018)*. Glasgow Royal Infirmary in Scotland was the first hospital that developed a self-illuminated endoscope in 1894. In general, endoscopy is the method of examination of the internal organs and vessels of the upper gastrointestinal tract by an instrument called endoscope (Figure 1.3). This instrument is a long, thin, flexible tube.

Figure 1.3. Endoscope

The main part of this endoscope is its fibre tube, composed by tens of thousands of fine glass fibres, used to carry the reflected images outside of the patient. Further improvements led to the addition of the biopsy's devices to the endoscope in order to extend its role. There is a lighting source in the fibre optic tube in order to illuminate the area and a miniaturized camera to obtain the images *(Pan et al., 2012), (Kohli et al., 2019)*.

During the procedure, a specialized doctor inserts the endoscope through the mouth and that allows the visualisation of the gastrointestinal tract on a screen. The endoscope might also be inserted in the body through the anus or through a small surgical cut (incision) made in the skin where necessary *(Chandrasekhara et al., 2019)*. This procedure allows the physician to examine the inside of the human body and to detect various gastrointestinal diseases. However, it presents some disadvantages, most important of which are the discomfort the patient might experience during the procedure and the sedation which in some cases might be dangerous. Furthermore, traditional endoscopy cannot reach the small intestine, and thus important information might be missed. In an effort to avoid these drawbacks, the idea of a swallowable wireless endoscope that could be used with no need of anaesthetic sedation of the patient, started to appear and will be presented in detail in the next subchapter.

1.3.2 Enteroscopy

Another important examination, leading to the exploration of the small bowel, is enteroscopy. It allows determination of 40% of undiagnosed cases of bleeding and it can examine approximately 50-80% of small intestine. It can be subdivided into push enteroscopy, device assisted enteroscopy (like double balloon enteroscopy), intraoperative enteroscopy which is achieved when the endoscope is guided with surgical assistance and sonde enteroscopy. All these different techniques to visualise part of the small intestine are going to be

analysed in the next paragraphs *(Landi et al., 1998), (Chauhan et al., 2015), (Filippone et al., 2007)*

Push enteroscopy is a procedure where an endoscope passes through the oesophagus, stomach and small intestine. Push enteroscopes are longer versions of the traditional endoscope, with a length of 150-200 cm, external diameter of 10.5-11.7 mm and interior diameter of 2.8-3.8 mm. The test lasts for approximately half an hour. In Figure 1.4 a diagram of the procedure is presented. It is a similar to endoscopy procedure although it allows the physician to examine a bigger portion of the small intestine. Common side effects of this procedure are sore throat, abdominal bloating and nausea while rare side effects include damage to the stomach or bowel and a reaction to the anaesthetic drugs. To undertake this procedure, the stomach needs to be empty to allow its better visualisation. During push enteroscopy, the patient is under mild sedation to help them relax. For 1 to 3 hours after the procedure, the patient is not allowed to drive, work or drink any alcohol. During push enteroscopy, the stomach is filled with air in order for the physician to have a cleared view of the interior. After the end of the test, this air is removed *(Landi et al., 1998), (Chauhan et al., 2015), (Bowen, 2016)*

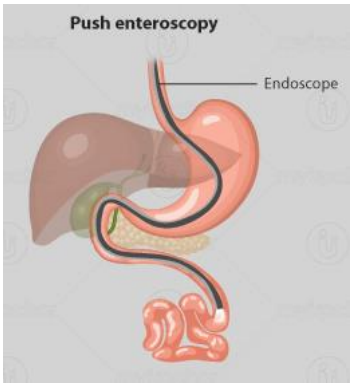

Figure 1.4. Schematic of push enteroscopy (Pandey, 2020)

Sonde enteroscopy (or device assisted enteroscopy) has been introduced in 1980 as an improved method to visualise the small intestine, compared to push enteroscopy. It includes a fibreoptic enteroscope with a balloon on its tip which progresses through the small bowel by peristalsis. A schematic of the procedure is illustrated in Figure 1.5. Sonde enteroscopy allows the visualisation of the remaining part of the small intestine. The examination of the bowel takes place

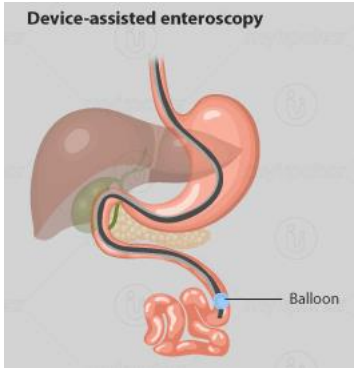

Figure 1.5. Schematic of Sonde Enteroscopy (Pandey, 2020)

when the physician starts to remove the endoscope from the small bowel. This procedure is time-consuming, it makes the patient feel uncomfortable and it does not allow therapeutics. For these reasons, the need to discover a better way to visualise the mucosa of the small bowel has been vital *(Chandrasekhara et al., 2019), (Giordano et al., 2009)*.

Double Balloon Enteroscopy (DBE) was firstly introduced in 2001, a technique that revolutionized the idea of small intestine enteroscopy. It uses a specially designed enteroscope with latex balloons on its ends. The balloons usage is to anchor the endoscope in place in order to allow a deeper insertion. The most commonly used enteroscope for this procedure has a diameter of 9.4 mm and a 200 cm length. Furthermore, it has a pump in order to inflate and deflate the latex balloons and a pump controller to stabilize the pressure to 5.6 kPa. During DBE, the balloons are deflated and inflated in increments of 40 cm each time (Figure 1.6). When the desired maximum insertion is reached, the procedure is finished, and the endoscope is carefully removed in short segments. The whole duration of DBE is 70 to 120 minutes. Before the procedure, the patient needs to be deprived of food for 12 hours and the last 4 needs to only consume liquids. The most common indication for double balloon enteroscopy is mid-gastrointestinal bleeding. This procedure is better compared to push enteroscopy because it has an improved insertion depth. However, two operators are required for DBE and thus more personnel needs to be trained *(Chauhan et al.,2015), (Saygili et al., 2015)*.

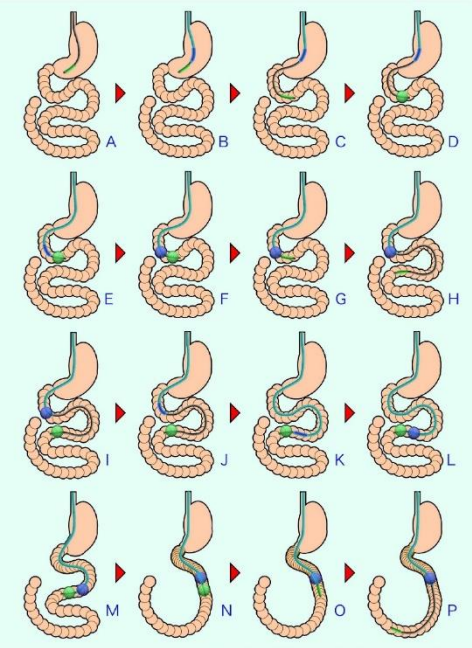

Figure 1.6. Schematic of Double Balloon Enteroscopy (Sunada et al., 2008)

1.3.3 Colonoscopy

Colonoscopy is a procedure introduced in Japan in 1950 that allows the visualisation of the large intestine. Furthermore, it facilitates biopsies and dilatation in case of a stenosis. It is an invasive procedure which requires an intensive preparation from the patient. The quality of this preparation has the greatest effect on its outcome. For the optimal result, a cleansing agent is required. Additionally, an only liquid diet is essential for 24 hours and a fasting period of 2 to 4 hours before the procedure. At the beginning of colonoscopy, the patient is positioned in a left lateral position with bent knees. For the procedure to start, there are three different options: no sedation, conscious sedation or deep sedation according to the preference of the physician, the availability of an anaesthesiologist, the patient's preference and financial reasons. When deep sedation is chosen, the patient feels no discomfort during the procedure and there is a decrease in the hospitalisation time. When, little or no sedation is chosen, the patient is awake and thus can move during the procedure, something that might facilitate the best visualisation of the large intestine *(Chandrasekhara et al., 2019), (Hazewinkel et al., 2011), (Waye et al., 2003)*. A schematic of this technique is illustrated in Figure 1.7.

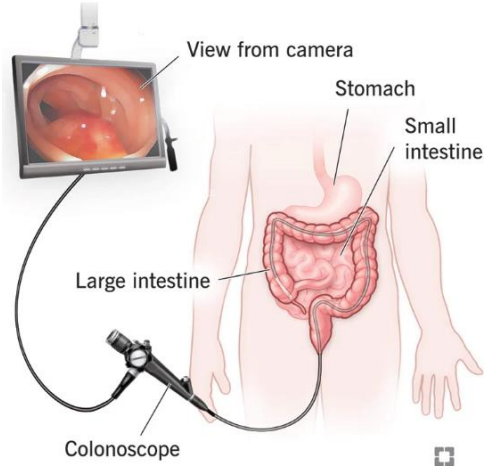

Figure 1.7. Schematic of Colonoscopy (Cleveland Clinic,2023)

One of the most important indications to colonoscopy is a positive faecal occult blood test, associated with colorectal cancer in 2-12% of the cases. This detection through colonoscopy is important because it leads to an early diagnosis of this cancer and thus to higher chance of survival. All persons with a positive faecal occult bleeding test and all persons that suffer with haematochezia or melena with a negative upper endoscopy result, need to undergo a colonoscopy. Complications occur approximately to 2 per 1000

patients that undertake the procedure. There are different contraindications for colonoscopy, and they can be divided into absolute and relative. The first category includes uncooperative patients that are not willing to consent to the procedure or conditions such as toxic megacolon or fulminant colitis. Relative contraindications are situations in which the risk of the procedure is considerably increased such as very large abdominal aortic aneurysm or patients who suffer from pulmonary embolism or myocardial infraction. Generally, when the risks are greater than the potential benefits, then the procedure is cancelled *(Hazewinkel et al., 2011), (Waye et al., 2003)*.

1.3.4 Angiography

Another technique used to detect bleeding in the gastrointestinal tract is angiography. It can detect bleeding of a rate as low as 0.5 ml/min in 50-86% of patients with OGIB. Angiography is a form of X-ray used to examine the blood vessels of the body. A small incision is made over one artery and a catheter is inserted inside it. Then, the catheter is guided to the area under investigation and a contrast medium is injected in the area. While this dye flows through the blood vessels, X-rays are taken. The duration of the test is from 30 minutes up to 2 hours. For the performance of angiography, instead of X-rays, computed tomography (CT) or magnetic resonance imaging (MRI) can also be used. The main contraindication is pregnancy, because radiation might affect the foetus. Furthermore, there is a small possibility of allergic reaction to the contrast medium *(Chandrasekhara et al., 2019), (Rossini et al., 1998), (NHS, 2020)*.

1.4. Capsule Sensors to Sense Bleeding

The procedures used to detect blood in the full gastrointestinal tract have several setbacks, most important of which are the discomfort the patient feels during the procedure, the sedation of the patient and that endoscopes cannot reach the small intestine due to their limited-length cable. Hence, important or

even life-threatening conditions in other segments of the gastrointestinal tract might be missed. The achievement of detecting haemorrhage through the whole gastrointestinal tract can be beneficial and it can lead to faster and more accurate identification of several different diseases *(Van de Bruaene et al., 2015)*. Thus, the creation of a device that would overcome these drawbacks while, at the same time, being able to detect bleeding in the gastrointestinal tract, has been of significant importance.

In 1981, the idea of a wireless camera pill that would be used to image the entire gastrointestinal tract, in a non-invasive way, has been introduced by Gavriel Iddan *(Adler, 2017)*. After that, the rapid evolution of complementary metal oxide semiconductor (CMOS) technology together with the advancement of miniaturised light-emitted diodes (LEDs) and application specific integrates circuits (ASIC) lead to the development of the first swallowable wireless camera pill *(Ciuti et al., 2011)*. This was a major breakthrough compared to conventional endoscopy.

The first wireless capsule endoscope (WCE) device was introduced by Given Imaging Company in 2000 and it received the FDA (US food and drug administration) approval in 2001 *(Cui et al., 2010), (Figueiredo et al., 2013)*. The capsule includes a miniaturized camera that takes photos of the inside of the patient, white LEDs to illuminate the area inside the human body, a battery source to provide a supply to the capsule and a data transmitter. Its dimensions are 11x26 mm, thus the patient is able to swallow it and it weights approximately 4 g. In Figure 1.8 the basic architecture of capsule endoscopes is presented. It is composed of 7 main parts, the optical dome, the lighting source (LED), a short-focus lens, a CMOS image sensor, the radio frequency transmitter, a micro control unit and a battery *(Pan et al., 2012)*.

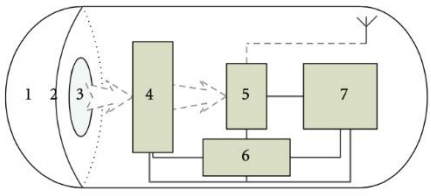

1 Optical dome
2 LED
3 Short-focus lens
4 CMOS image sensor
5 RF model
6 MCU
7 Power model

Figure 1.8. Capsule Endoscope's Main Architecture (Pan et al., 2012)

After the capsule is swallowed, the peristaltic movements of the gastrointestinal tract allow it to move through the tract and take images *(Cui et al., 2010), (Figueiredo et al., 2013), (Sekuboyina et al., 2017)*. The capsule is capturing images with 2-4 fps (frames per second) and then transmits them to a belt (recorder) worn by the patient by using radio-telemetry. The capsules' telemetry system is composed by the transmitter, the propagation channel and the receiver. The transmitter is responsible for the manipulation of the signal in order to be transmitted through a desired channel. The receiver demodulates the incoming signal to obtain the original information *(Figueiredo et al., 2013), (Li et al., 2014)*.

Generally, capsule endoscopy can be used to diagnose several conditions such as Crohn's disease, celiac disease, or tumours. However, its primary use is the detection of obscure gastrointestinal bleeding. This is persistent bleeding of the gastrointestinal tract that cannot be detected by oesophageal gastroduodenoscopy (EGD) or colonoscopy *(Van Turenhout et al., 2010), (Matas et al., 2006)*. Wireless capsule endoscopes have assisted over 1.6 million patients worldwide until now *(Suman et al., 2017)*. The capsule is capable of recording data for approximately 8 hours, which is the lifetime of its battery, and it can capture more than 50,000 useful images. After that time, the belt/receiver around the patient is removed, and the physician uses a specific software to review and analyse the images *(Cui et al., 2010), (Figueiredo et al., 2013)*.

Although there are a lot of indications for the usage of capsule endoscopes (CE), there are also a few contraindications. Patients with implantable electro-medical devices such as cardiac pacemakers or implantable cardioverter-defibrillators have been found not-appropriate candidates for a CE procedure. As above mentioned, these capsules transmit images acquired from the gastrointestinal tract by using a digital radiofrequency communication channel. Consequently, a possible interaction between the capsule's radiofrequency communication channel and the implantable electro-medical

device has been investigated *(Bandorski et al., 2014)*. Several different experiments have been conducted and discussed *(Bandorski et al., 2014), (Harris et al., 2013), (Goenka et al., 2014)*. The results from these studies have been extracted by clinical experiments (in vivo and in vitro) where physicians used a vast variety of different capsules. The overall conclusion has been that the potential for interference can be overcome by ensuring that the capsule endoscope and the implantable device are placed as far away as possible *(Harris et al., 2013)*.

Another contraindication of using capsule endoscopes is the possibility of small bowel obstruction. Generally, there is an increased risk of capsule retention while the capsule is located in the small bowel. Thus, it is important that the procedure will not be performed while there is strong suspicion of presence of bowel obstruction. Furthermore, when the patient presents swallowing disorders, there is the possibility that the capsule would retain in the oesophagus of the patient. To avoid that complication, a specific device called AdvanCE (by US Endoscopy) is used to guide the capsule immediately to the stomach. Finally, pregnant women have been found not suitable for a capsule endoscope procedure due to possible teratogenic effects to the foetus caused by the transmitted microwaves that the capsules use *(Goenka et al., 2014)*.

Capsule endoscopes offer several advantages over cable endoscopy, such as reduced patient discomfort, the fact that they do not require the sedation of the patient, they have little, or no side-effects and they can save a sufficient amount of data due to the sufficient framerate of the capsule endoscope. Furthermore, capsule endoscopy is a simple procedure that does not require the doctor to be present during the scan *(Sekuboyina et al., 2017), (Cui et al., 2010)*. The most important advantage emanated from the usage of these capsules is that they can reach the small intestine, which is one of the most difficult to visualise parts of the gastrointestinal tract due to its length and anatomy that involves complex loops. Before the invention of capsule

endoscopes, the visualisation of the small bowel was only possible by indirect methods such as computed tomography, magnetic resonance imaging or barium examination *(Hara et al., 2005)*.

Although, capsule endoscopes have a lot of advantages compared to conventional blood detection techniques, they also present a set of disadvantages. Capsule endoscopy has a time-consuming reviewing process which takes at least two hours to finish because the physician needs to view over 50,000 images per examination. Furthermore, symptoms of diseases (such as bleeding) may be present only in one or two frames of the video and they might be missed by the physician during diagnosis *(Cui et al., 2010), (Suman et al., 2017)*. Additionally, there is the risk of stagnation of the capsule if the patient suffers from small bowel obstruction *(Van Turenhout et al., 2010)*. Another drawback is that the images typically acquired by capsule endoscopes have a resolution of 256x256 or 320x320 compared to the 720x480 resolution of a conventional endoscope. This resolution is very low to allow the naked human eye to detect any potential abnormality *(Usman et al., 2016)*. Moreover, due to the tissue communication involved, there can be data loss due to communication errors that might distort the disease's diagnosis *(Lee et al., 2012)*. Further disadvantages of capsule endoscopes' ability to detect blood are the intensity of the illumination light source, which is not stable during the whole procedure, the change in blood's colour due to gastrointestinal liquids, the exact localisation of the capsule and the detection of non-bleeding parts of the gastrointestinal part that despite they are healthy, have a reddish appearance *(Mackiewicz et al., 2008)*. Therefore, wireless capsule technology is still an emerging technology, and various technical improvements need to be encouraged.

There are several different capsules for the physician to choose from. Five of them are the most well-known and researched. A brief summary of their properties is given in Table 1.3.

Table 1.3. Summary of existing capsule endoscopes (Pan et al., 2012), (Goenka et al., 2014)

	PILL CAM SB3	**MIRO CAM V2**	**ENDOCAPSULE**	**PILLCAM COLON 2**	**CAPSO CAM SVI**
Company	Given Imaging, Yokneam	IntroMedic Co., Seoul	Olympus Co., Tokyo	Given Imaging, Yokneam	CapsoVision® Inc., Saratoga
Country	Israel	South Korea	Japan	Israel	United States
Field Of View	160^{o}	170^{o}	145^{o}	360^{o}	360^{o}
Lens	Multi element	No	No	No	No
LEDs	4	4	4	4	16
Image Sensor	CMOS	CMOS	CCD	CCD	N/A
Transmission	radiofrequency	Electrical Field Propagation	radiofrequency	radiofrequency	On-board EPROM flash memory
Frames Per Second	2-6	2	2	4-35	16
Dimensions (mm)	11*26	11*24	11*26	11*31	11*31
Weight (g)	3.45	3.2	3.45	2.9	4
Battery (h)	9-11.5	12	8	10	15
FDA Approval	yes	yes	yes	yes	no
Software	Rapid v7	MiroView v2	OLYMPUS WS-1	Rapid Reader v9	CapsoView

An important factor affecting the performance of the capsule endoscope is the sensor used. In the literature, it has been found that optical sensors are mainly used. However, in the past few years spectroscopic technology has been investigated for data extraction. This technology loses imaging capability in favour of a simpler, spectrally resolved optical detection, ideally sensitive and specific to blood. Furthermore, more significant data can be extracted, providing more information to the outer world while minimising the overall data volume. Recently, OVESCO Endoscopy AG *(Schostek et al., 2016)* have introduced to the market a capsule pill that after being swallowed by the patient, is capable of detecting possible life- threatening gastrointestinal bleeding by using optical spectroscopy measuring the differential optical absorption at two wavelengths. The detection is done while the pill is attached to the stomach's wall. A core advantage of this technique is that the capsule can be left in place, able to monitor bleeding for up to a few weeks. However, a major drawback of the above-mentioned pill is the fact that it only operates within the stomach. As a consequence, the extracted information is limited. Hence, important or even life-threatening bleeding in various other segments of the gastro-intestinal tract might be missed.

Capsule endoscopes are an important diagnostic tool. As mentioned in the previous paragraph, the spectroscopic capsule by Schostek et al. managed to overcome a lot of the previous drawbacks of capsule endoscopes. Specificity is an important parameter in a capsule since inside the gastrointestinal tract: blood, bile, and food with variation of colours can be found. However, although Schostek's capsule is highly sensitive, it is not specific since it only utilises two wavelengths for detection *(Schostek et al., 2016)*. At this stage, the creation of a capsule that uses enough wavelengths to be able to detect all these colour/substance variations would be highly welcome.

1.5. Data Transmission from Capsule Sensors

The wireless communication used in capsule endoscopes is crucial for data transmission. The quality of wireless telemetry is defined by power efficiency and data rate. Generally, capsules have a limited power budget while they need to transmit images in an adequate data/frame rate. Most capsules have maximum image resolution of 512x512 with a frame rate of 2-6 frames/s and power budget around 20 mW (two silver-oxide batteries) *(Sushma et al., 2022), (Singeap et al., 2016)*.

To design an efficient telemetric link, the electric power consumption needs to be low, the data rates need to be high while at the same time, the transmission signal's power needs to be kept in medically safe limits *(Toennies et al., 2009)*. There are three most widely known and used technologies to achieve wireless transmission in capsule endoscopes: Radio Frequencies (RF), human body communication and integrated data storage.

Radiofrequency transmission is the most common technique, used in most pill sized capsules. The images that the camera acquires, are transmitted using radiofrequency through an integrated in the capsule antenna to an outside sensing antenna. A schematic of the procedure is presented in Figure 1.9. The sensor is placed on the waist of the patient like a belt, in direct contact with the skin. A portable storage device is connected to the sensor to store the data. A computer's display can be used to illustrate in real-time the received data. After the completion of the diagnosis, the sensor can be detached from the waist of the patient and connected to a computer for data transfer and analysis *(Keuchel et al., 2015)*.

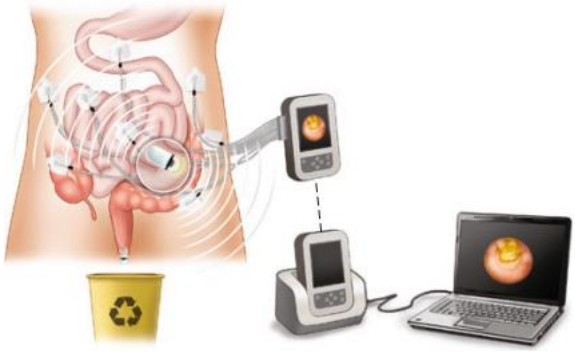

Figure 1.9. Schematic of RF transmission technique (Keuchel et al., 2015)

However, this technique is very highly energy-consuming *(Li et al., 2014)*. Furthermore, due to high absorption from human tissue, radiofrequencies

reduce the transmitted signal. Therefore, the usage of a high-gain antenna is necessary to receive weaker signals *(Park et al., 2018)*. As operational radio frequencies for capsule endoscopes, a range of 400-600 MHz is proposed because in this band the propagation loss in human tissue is limited. Generally, magnetic over electric antennas are preferred because they are less sensitive to the surrounding human tissue *(Miah et al., 2018)*.

MiroCam capsule uses human sensor communication by utilising a spectral exterior bipolar casing and sensor electrodes attached to the skin, thus using the human body as a conductor. This technique requires less power compared to radiofrequencies. However, it is similar to them in the fact that it also requires a portable storage device to be worn by the patient and then connected to a computer for analysis of the data. Furthermore, in both techniques the capsules do not store any information and thus can be discarded after the completion of the procedure. *(Keuchel et al., 2015)*.

The third technique is called integrated data storage communication. It is used by the CapsoCam capsule which uses an integrated Flash EPROM memory to store the images. In this communication type, the existence of a receiver and a transmitter are not necessary. After the completion of the endoscopic procedure, the capsule is returned to the practitioner in order for its data to be restored and analysed *(Keuchel et al., 2015)*. The main drawback of this communication technique is the fact that it does not provide the possibility of live observation of the examined area *(Koprowski, 2015)*. This becomes important if the doctor needs to do any other operation in real time, such as steering or operating the capsule in a specific area. For example, Schostek et al. developed the VECTOR project *(Schostek et al., 2013)* that has been used for active locomotion, wireless therapy, and detection of gastrointestinal bleeding.

The different radio channels are characterized by their Bit Error Rate (BER). The BER is the number of errored bits divided by the total number of the bits that are transferred from the transmitter to the receiver. There are three ways

used to ensure a relevant improvement in the BER characteristics, using noiseless coding, using the checksum or using a confirmation protocol. Noiseless coding, for example Reed-Solomon, adds redundant bits to the message but allows the recovery of the original message when a repeated error occurs. The checksum, where redundant bits are calculated from a specific, controlled set of bits ensuring that when an error occurs in N bits, then the checksum's recalculation will lead to a different result. The last method is the usage of a protocol with confirmation, where the transmitter retransmits a set of bits if the receiver does not confirm its receival for a specific period of time *(Anpilogov et al., 2016)*.

Capsule endoscopes transfer images to the receiver. No significant data compression can be applied to these imaged, as this would impact on the power budge. To transfer an uncompressed square image of 200x200 pixels, at 24 bits Red Green Blue (RGB, 8 bits per colour), in a frame rate of 2 frames/s, the data rate will approximately be 1.9 Mbps. To achieve that, several parameters like transmitting power, frequency of communication, size of the system and modulation method must be carefully selected. The permittivity of the human organs in the low-frequency band (bellow 1 GHz) is high and the conductivity is high in the high-frequency band (above 1 GHz) *(Moon et al., 2014)*. Hence, the attenuation of the signal is high in the high-frequency region and the carrier frequency is barely sufficient in the low-frequency region. When radiofrequencies are used, there is significant loss of signal due to the attenuation of the signal in the different body tissues and due to the reflection in their boundaries.

The human abdomen's anatomy, presented in subchapter 1.1, is highly complex. Each part of the gastrointestinal tract (stomach, small and large intestine) contains a series of different tissues such as muscle, fat and skin in different shapes and thickness and with varying dielectric properties. At each stage of the capsule's journey inside the gastrointestinal tract, different structures are closer to the capsule and thus their influence on its

electromagnetic communication varies. In most simulations, to facilitate the modelling of this highly complex inhomogeneous human body, a simpler, homogenous body model is used. This model is mostly based on muscle's properties, which is the layer closest to the capsule. From literature, muscle's permittivity is ε_r= 56 and its conductivity is σ=0.83 S/m at 400 MHz of operation. *(Wang et al., 2016)*.

1.6. Optical Communication

Radiofrequencies (RF) are the most common technique used in capsules to transfer information. When RF is too expensive, non-viable or too slow for the purposes of a project, free space or guided optical communication can be used. Indeed, this thesis is based on the assumption that optical communication overcomes the problems of limited bandwidth and significant data lost due to the attenuation of the signal in the different types of tissue.

Optical communication is the communication using light to transfer information at a distance. To achieve optical communication, a transmitter, a channel, and a receiver are utilised. The transmitter encodes the information into an optical signal, the channel carries that signal and finally the receiver accepts this signal and reproduces the original information. Semiconductor devices like lasers and light-emitting diodes (LEDs) are most commonly used as transmitters. Photodetectors are used as receivers, to convert light into an electrical signal. Optical fibres, optical amplifiers, lasers, and routers, all make usage of modern optical communication techniques. Their main benefits are high bandwidth, low signal loss, good transmission range and no electromagnetic interference. However, their cost is high *(Rouse, 2011)*.

Optical communications have been used for long time. An example of their usage has been the remote controls on the television. As early as 1994, companies were working together to form an association called Infrared Data Association (IrDA) *(irda.org)*. This association provides specifications for a set of protocols regarding infrared wireless communications. The same name is

used to describe this set of protocols. It is used in data transfer in short distances (less than 1 meter), for example laptops, telephony, cameras and medical devices. The advantages of these protocols are that data can be safely transferred at low bit error rates (less than 10-9). It can operate at the 850-900 nm wavelengths. However, its bandwidth is low. More specifically, it can transfer data with a rate up to 4Mbits/s *(Millar et al., 1998)*.

More recently, with the evolution of technology and sensors, Ferreira et al. *(Ferreira et al., 2016)* have developed a high bandwidth visible light communication (VLC) system. VLC is a rapidly evolving technique that is trying to replace RF at short range. By modulating Gallium nitride LEDs, utilising parallel data transmission and equalisation, they can allow data transmission at a rate above 1 Gbps. Ferreira et al. is using a Gallium-nitride based LED as illumination source, that has a very high electrical to optical modulation bandwidth, exceeding 800 MHz. They used ON-OFF Keying, pulse amplitude modulation and orthogonal frequency division multiplexing modulation and they managed to transmit data through free space at rates of 1.7, 3.4 and 5 Gb/s respectively.

1.7. State-of-the-art

In summary, wireless capsule endoscopy is a rapidly advancing field offering a non-invasive evaluation of the digestive system. Is uses a swallowed capsule-shaped miniature camera for direct visual and diagnostic evaluation of GI diseases. It eliminates the need for sedation and the risks associated with traditional endoscopy. Originally it was intended as a tool to examine the small intestine, which is beyond the reach of conventional endoscopy, but now it is also being used to examine the entire length of the GI tract.

Existing devices face limitations, such as the absence of treatment capabilities or limitations in lesion detection. However, the landscape is changing rapidly with recent breakthroughs in micro-electromechanical manufacturing and computational techniques, paving the way for extensive research into the

integration of advanced technologies into commercial capsule endoscopes *(Cao et al., 2024)*. Some technological advancements that are expected to revolutionize the field of capsule endoscopy are near-field wireless power transmission, magnetic field active drive, intrabody communication, AI-based autonomous lesion detection and magnetic-controlled diagnosis and treatment.

There are various groups working on the limitations of capsule endoscopy. In particular, the group of Mohebbian *(Mohebbian et al., 2021)* presents an innovative approach for detecting gastrointestinal bleeding using on-chip multispectral imaging sensors. The 12 utilised sensors capture images across different wavelengths, providing valuable spectral information beyond what conventional endoscopy offers. Furthermore, the group has created a capsule prototype that uses diodes that can work on 450 nm, 610 nm and 810 nm. In this prototype, another PIN diode is used to collect the reflected light. Their system's performance has been evaluated with tests in porcine intestines.

Their results demonstrate promising performance in detecting bleeding lesions. Mohebbian's research contributes to advancing capsule endoscopy since the proposed system is power efficient and with robust bleeding detection capabilities, according to the 99% result of the F1-score. However, this group used a large number of sensors (12) combined in a PCB, thus the technology they created cannot be miniaturised. Furthermore, they utilised RF communication in their capsule, with all the limitations previously highlighted (more importantly the limited bandwidth and data loss due to the attenuation of the signal inside the human tissue).

The group of Mahmoud et al. *(Mahmoud et al., 2022)* in their research introduce a novel approach to detect UGIB. Their approach is using a disposable swallowed optical sensor capsule and an external receiver. Detection of blood in the stomach is achieved by the optical sensor that measures the absorption of multiple wavelengths of light (including near IR). Data are then transmitted to the receiver wirelessly and an algorithm determines the presence of blood.

They have used various blood and non-blood (food pigments or natural foods) samples for their experiments.

Mahmoud's research represents a significant advancement in the field of GI bleeding detection. His group is near-clinical trials and has developed a disposable swallowable optical sensor capsule combined with an external receiver. However, the paper does not provide specific information about the sensors employed, including whether the group developed custom sensors or utilized preassembled ones. These technical aspects are crucial for understanding the feasibility and limitations of this capsule. Therefore, this work is difficult to be evaluated and also not able to be reproduced since they provide limited information.

Khan et al. *(Khan et al., 2020)* addresses the need for automated bleeding detection in WCE. The proposed system integrates into WCE devices an on-chip bleeding sensor. This sensor performs real-time pre-screening based on blood's optical properties. The study evaluates blood's chromatic properties using a spectrophotometer. Reflection ratio pairs at specific wavelengths (700 nm to 630 nm and 480 nm to 530 nm) are crucial for distinguishing blood from non-blood samples.

The authors validate their findings by implementing hardware using small LEDs and photodiodes. This sensor system can be integrated into a WCE device for rapid and real-time GI bleeding detection. The introduced sensor seems promising, and this paper proves its feasibility. However, more robust studies need to be performed to address its accuracy, sensitivity, and specificity. The group does not provide detailed information regarding the design of the sensor and the used algorithms. Therefore, once again, this work cannot be reproduced. Furthermore, the sensor introduced by this group has limited detection channels due to the small number of LEDs employed in their system.

Another team that conducted interesting research is Varotsos' group. They calculated the theoretical bandwidth in different optical communication

channels *(Varotsos et al., 2019)*. This work is only theoretical with no experimental demonstration. Their simulated system was consisting of an out-of-body unit as transmitter, the skin (epidermis, dermis and hypodermis) and then a number of M in-body units in a straight-line configuration (Figure 1.10).

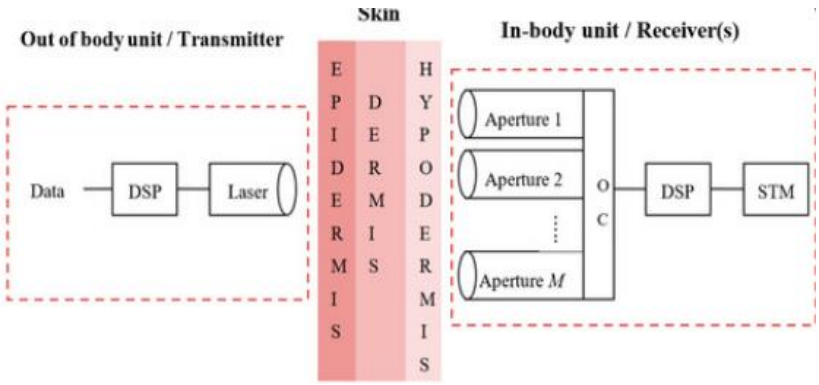

Figure 1.10. Block Diagram of Varotsos setup (Varotsos et al., 2019)

The geometry being used on this paper, with the out of body transmitter and the in-body units in a straight-line configuration is not anatomically compliant with what I wanted to simulate during my experiments. Furthermore, they did not simulate appropriately the bandwidth reduction due to the multipath effects that are analysed in the rest of this thesis. In my experiments I wanted to simulate a geometry that would replicate as closely as possible the idea of an in-body transmitter and an outside-body receiver. More specifically, a geometry where the transmitter would be placed in the middle of an ellipsoid prism while the receiver would be placed all around that ellipsoid. This setup was chosen to reflect the clinical scenario of an in-body device communicating with an external receiver, which is a common configuration in emerging medical technologies.

Other groups also expressed interest in the field of capsule endoscopy, but they are only limited in literature reviews. In this part of the subchapter, the work of Moglia's group is going to be briefly presented. They concentrated on existing capsule sensors, thoroughly examining their respective advantages and limitations.

The group of Moglia et al, conducted a review of existing endoscopic capsules as well as their main limitations and ways to overcome them *(Moglia et al., 2009)*. It emphasizes on the characteristics, differences and usability of the main capsules existing today. Then, it describes the main challenges these capsules face like the detection of their position, the control of their movement, the control of the camera's orientation. Lastly, Moglia emphasizes on the main desirable functionalities an endoscopic capsule should include like the ability to collect biopsy samples, deliver optical biopsy devices, drug delivery, sense of oncological markers and the development of technologies for bleeding control and thermal ablation. This has been a beneficial review to understand the current state of capsule endoscopy and to envision its future trajectory.

1.8. Hypothesis, Aims and Objectives

My research has been centred around two critical gaps. The first one pertains to the limited number of channels of spectrometric sensing in existing capsule endoscopes, as clearly evident from the studies conducted by Khan and Mohebbian. The second one involves challenges associated with the widely used, in capsule endoscopes, RF communication which is too slow, resulting in poor video quality and resolution, limited data transmission efficiency and limited battery life.

We believe it is possible to design a multispectral sensor, intrinsically capable of higher specificity, without increasing the power budget existing in a capsule. Furthermore, we believe that, by using the optical transparency of tissue in the infrared range, it is possible to increase the communication bandwidth by transmitting data optically, yet with a power budget compatible with a capsule.

My thesis has been structured around three specific aims:

1. To increase the number of sensing wavelengths of a multi spectral sensor without increasing the size, the power budget and the number of optical channels in this sensor. This has been presented in Chapter 2,

where the number of channels has been increased by an appropriate method which uses source multiplexing.

2. To examine the feasibility of increasing the speed of the communication link by using optical data transmission. This has been achieved by the conduction of Monte Carlo simulations of the optical bandwidth of a data transmission system, presented in Chapter 3.
3. To implement a demonstrator of an optical data communication system for data transmission through tissue. This included the design, build and demonstration of a custom system that comprises of a receiver and a transmitter. This is the work presented in Chapter 4.

The three primary objectives to address the aims mentioned above are as follows:

- to design a bench top optical sensing system that with a commercial multispectral sensor and a small number of additional parts achieves a high number of detection channels
- to perform a computational estimation that optical data transmission through thick human tissue at high bandwidth is possible and
- to design and physically build a demonstrator for this data transmission channel that would result in the optical transmission of an image through tissue.

1.9. Thesis Structure

In the 1st Chapter entitled "Introduction", a general introduction to the problem this PhD is trying to solve is given. The anatomy of the gastrointestinal tract is presented together with the most common reason that lead to its bleeding. Then, the techniques that facilitate sensing of blood are analysed together with the most recently developed and used capsule sensors. At the end, the most commonly used communication techniques from these capsules are presented and the assumptions, objectives and structure of this thesis are outlined.

The 2nd Chapter, "Design of a multispectral sensor", focuses on increasing the wavelengths that a 6-Channel, commercially available sensor can detect to a much higher number of wavelengths. The goal has been to prove that this increase in the number of channels a sensor can detect, can be achieved by using a very small number of additional parts without altering the power budget. This has been accomplished by employing a set of multiplexed spectrally colored illumination sources (LEDs).

The 3rd Chapter is entitled "Simulations of optical data transmission through tissue". For my research, I wanted to use optical communication to transfer information from the inside of the human body to the outside world. However, the different types of tissue inside the human body lead to scattering of the signal that limits the bandwidth and the absorption of light through tissue leads to attenuation of the signal. Thus, to estimate if the problem of optical data transmission through tissue is well posed, simulations have been conducted before my actual system has been built. These Monte Carlo simulations are presented in this Chapter.

Chapter 4 is entitled "Design of the Subsystems". After my simulations have showed that the problem of transmitting optical signal through tissue is well posed, I have built the physical system that would achieve that. In this 4th Chapter I describe the implementation of a tethered capsule that transmits data through tissue using an optical link, show that this capsule achieves a high data transmission rate several orders of magnitude higher than the state-of-the-art for endoscopic capsules and demonstrate the actual transmission of an image at high data rates through tissue.

Chapter 5 presents how the thesis as a whole relates to the current state of the art. Then the limitations of this work as well as recommended future work are stated.

CHAPTER 2

DESIGN OF A MULTISPECTRAL SENSOR

Parts of this chapter have been published at the Annual International Conference of the IEEE Engineering in Medicine and Biology Society (EMBC 2022), with reference: Katsafadou M, Giardini ME. Source multiplexing enhances the number of channels of a multispectral sensor. Annu Int Conf IEEE Eng Med Biol Soc. 2022 Jul;2022:2455-2458. doi: 10.1109/EMBC48229.2022.9871570. PMID: 36086097.

2.1. Introduction

2.1.1. Addressing Capsules' Specificity Limitations

Endoscopic techniques are benefitting from a rapid evolution of miniaturised sensing technologies, to be deployed on board of in-body sensing capsules. Amongst these, optical spectroscopic and colorimetric sensing play a key role *(He et al., 2021)*.

The most recent evolutions in UGIB detection use telemetric capsule-based differential optical sensing at two wavelengths *(Schostek et al., 2016)*, that can be either swallowed for active bleeding detection or anchored to the gastrointestinal wall for rebleeding detection. A CAD rendering of this capsule is presented in Figure 2.1. It has a diameter of 6.5 mm and a length of 25.5 mm. This Figure presents a general diagram of a capsule that uses optical absorption measurements for sensing substances using two wavelengths *(Schostek et al., 2016)*. The capsule has an LED in one side, a gap in the middle for the entry of the sample under investigation and a photo transistor on the other side.

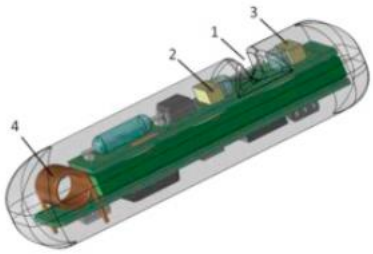

Figure 2.1. CAD model of telemetric capsule. 1. recess for the entry of blood, 2. photo transistor, 3. LEDs, 4. helical antenna (Schostek et al., 2016)

The sensitivity of the capsule presented in Figure 2.1 is high, albeit the specificity could benefit from an increase in the number of wavelengths, moving towards a multispectral/spectroscopic system. Yet, commercial

wavelength-resolved sensors for capsule sensing, either exhibit a low number of wavelengths, 8 being the practical maximum for a single compact device (AS7341 sensor), or rely on bulky external spectrometers *(Ehrlich et al., 2017)*. Ideally, a spectrometric detector that is small enough while at the same time exhibiting a high number of optical detection bands to allow the detection of different chromophores would be the desired solution.

The number of detection bands (channels) needed depends on the number of substances needed to be differentiated from. Inside the gastrointestinal tract, there are two types of blood, oxygenated and de-oxygenated, bile, and at least 3-4 colours of foods *(Schostek et al., 2016)*. Thus, neither the 2 wavelengths of existing sensing capsules, nor the 8 wavelengths of the commercial sensor are sufficient for an accurate detection (AS7341 light/colour sensor). Additionally, the substances needed to be detected have signatures in the visible but also in the near infrared range. This means that the number of channels the sensor can detect needs to be increased in the order of 10 or more, while at the same time keeping the power budget the same.

For this initial step of my research, I could not build a capsule, because the miniaturisation of my system would be time consuming and access to labs was restricted during COVID. Therefore, the primary objective during this phase has been to use an existing sensor and by time multiplexing the light sources with the sensor's channel sensitivities, to increase the number of wavelengths this physical sensor can measure. For this purpose, a simpler demonstrator has been developed to evaluate this core concept.

2.1.2. Beer-Lambert Law

Spectrometry is a technique widely used to measure the concentration and intensity of a particular colour present in a complex mixture. The principle behind this technique is that monochromatic light is emitted by a source, for example by filtering an LED using a band pass filter and then this light passes through a cuvette containing the examined sample consisting of a substance

(e.g. blood). The filter ensures that the sample is illuminated only by the wavelength of interest. The intensity of light, after it passes the sample, is smaller compared to the light that entered the cuvette. This loss of light equals with the absorption of the sample, and it is related to the concentration of the measured sample *(Sherwood Scientific Ltd, 2020)*.

This technique follows the principles of Beer-Lambert law which states that when a light of a specific wavelength passes through a sample, the transmitted light decreases as the concentration increases. Additionally, Lambert's law states that light transmission decreases as the sample's thickness increases *(Mar Athanasius College, 2020)*. More precisely, the Beer-Lambert law creates a relationship between the attenuation of light passing through a sample and the optical properties of that sample. In the case of monochromatic light, the intensity of the incident light is defined as I_0 and the transmitted light's intensity as I. The transmittance T is described in Equation 2.1 and has values between 0 and 1:

$$T = \frac{I}{I_0} \qquad 2.1$$

The absorbance A is dimensionless and is defined by Equation 2.2 as:

$$A = \log_{10} \frac{I_0}{I} = -\log_{10} T \qquad 2.2$$

When the absorbance is 0, the transmittance is 100% while when the absorbance equals to 1, the transmittance is 10%.

The light absorbance can also be calculated by Beer-Lambert law as shown in Equation 2.3

$$A = \varepsilon C d \qquad 2.3$$

where, ε refers to molar absorption coefficient (mol^{-1} cm^{-1}), C is the molar concentration of the sample (mol) and d represents the optical path length of the sample (cm). This law states that there is a linear relationship between absorbance and concentration of solution. That facilitates the calculation of the solution's concentration by initially calculating its absorbance *(McNaught et al., 1997)*.

In the context of a multi-substance system, the Beer-Lambert Law can be applied to each individual substance. In this case of the multi-substance system, Equation 2.3 is extended as follows:

$$A_\lambda = \varepsilon_\lambda C d \qquad 2.4$$

where A_λ is the absorbance at a specific wavelength λ and ε_λ is the molar absorption coefficient at that specific wavelength. The total absorbance of the system is then the sum of the absorbances of each individual substance, like described in Equation 2.5:

$$A_{total} = \sum_1^i A_i \qquad 2.5$$

where A_i is the absorbance of each of the i individual substances in the system. This assumes that the substances do not interact with each other in a way that significantly changes their individual absorbance characteristics.

It needs to be noted that according to Equation 2.3, Beer-Lambert's law clearly states that the absorbance of a sample is directly proportional to its concentration. As the concentration of the sample increases, more radiation is absorbed and thus the absorbance is increased. However, the peak wavelengths of the spectrum are not affected by the concentration of the sample. This peak corresponds to the colour of light that is mostly absorbed by each sample. It is determined by the energy transitions inside the molecules of the sample. These energy transitions are unique for each molecule and are not affected by concentration. Therefore, while the concentration of each sample can indeed affect the intensity of absorption (the heigh of the peak in the absorption spectrum), it does not affect the position of that peak *(Wormell et al., 2013)*.

Chromophores are molecules that have the ability to selectively absorb light at specific wavelengths. According to Equation 2.3, the absorbance of any given substance or chromophore at a particular wavelength is directly proportional to its concentration. Equations 2.4 and 2.5, taken simultaneously for all chromophores, define therefore a set of independent linear equations, where the different concentrations of the chromophores represent the

unknowns. The number of equations needs to at least match the number of chromophores, meaning that the number of wavelengths required must at least match the number of chromophores. Therefore, to comprehensively detect all chromophores, a detection system must be equipped with the capability to discern at least 10 to 12 distinct wavelengths.

At the time of writing the thesis, new sensors designed for spectrometric applications, have been made available in the market (like the AS7341 11-channel light/colour sensor). However, on the time of doing the experiments, only a few sensors were available. These were the ones I investigated. In this chapter, I initially present a list and comparison of these commercial multispectral sensors capable of identifying blood concentration. After identifying the most suitable for this application sensor, tests have been done to increase the number of spectral bands sensed by it. This has been achieved by using the sensor that has certain spectral sensitivities and combining it with a set of light sources with different spectral sensitivities. Then, by time-multiplexing these sensitivities, the peak sensitivity of each sensor channel has been shifted. A simple set-up is described and tested on a set of multiple dye solutions. Then the linearity of my setup is presented.

2.2. Methodology

2.2.1. Experimental Setup

In the market there are compact sensors capable of detecting visible light with some form of spectral resolution. However, they can detect a limited number of wavelengths. We believe it is possible to design a multispectral sensor, intrinsically capable of higher specificity, without increasing the power budget of our system. Specifically, three LEDs are going to be used, combined with a 6-channel sensor. The spectral region investigated by each LED-channel pair is effectively given by the product of the source spectrum and the channel

spectral sensitivity. In practice, therefore, with this multiplexing, each detector channel can detect three independent spectral regions.

To evaluate my idea, I have built a setup which optically is analogous to a capsule that uses optical communication. In Figure 2.2, a diagram of this setup is illustrated. In one side the used source of light (an LED) is placed. An Arduino (Arduino S.r.l., Italy) board is used to power and control this source. The light is then scattered inside the designed integrating sphere and then passes through the used sample. The sample's volume is 4 ml, and it is placed inside a plastic transparent cuvette with a 10 mm light path. At the end of my setup all the light is collected by the detector. This detector is controlled by a Raspberry pi Pico (Raspberry pi Ltd, Wales) board.

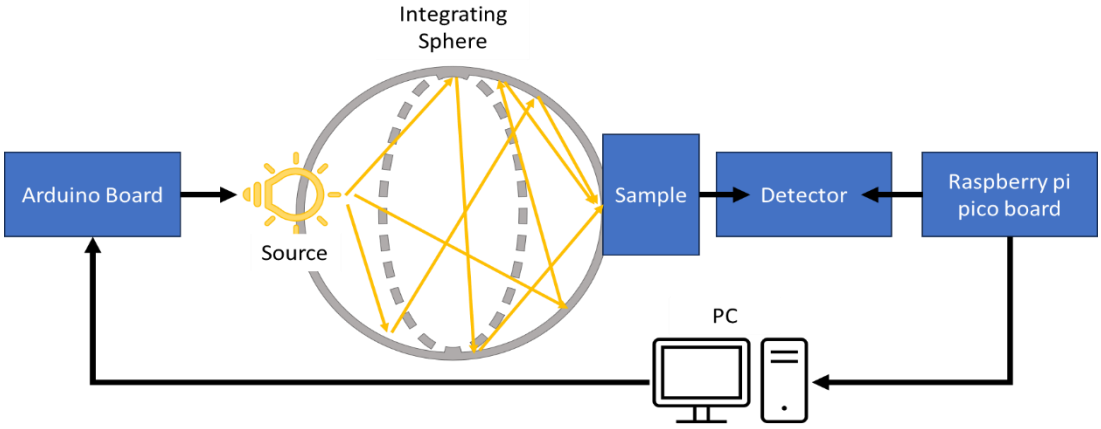

Figure 2.2. Diagram of used Setup. An Arduino Board is used to drive the light source. Then this light travels through the integrating sphere and passes through the sample to be finally collected by the used detector. The detector is driven by a Raspberry pi Pico board. Both boards are controlled by a PC.

To initiate the experiments, it has been critical to select the optimal sensor for conducting the tests. Four different sensors have been tested, which effectively were, to our knowledge, all the sensors commercially available at the period these experiments took place. The main characteristics of the sensors under investigation are presented in Table 2.1.

Table 2.1. Main characteristics of sensors under investigation.

No.	Name of Sensor	Dimensions (mm)	Sensing Area	Channels
1	AMS OSRAM TCS34725	2.0 x 2.4 x 0.65	0.406 x 0.369 mm^2	Red, Green, Blue, Clear
2	Vishay VEML6040	2.0 x 1.25 x 1.0	0.36 x 0.29 mm^2	Red, Green, Blue, White
3	AMS AS7262 6-channel Spectral Sensor	4.7 x 4.5 x 2.2	4.40 x 4.50 mm^2	Red, Orange, Yellow, Green, Blue, Violet
4	AMS AS7265x Smart Spectral Sensor	4.5 x 4.7 x 2.5	Each sensor has Ø 0.75 mm	3 chip set delivering 18 VIS and NIR channels from 410nm to 940nm

From the four sensors, the third and fourth have the highest number of channels. However, sensor number 4 is using three chips to detect a total of 18 channels (each chip detects 6 channels). Sensor 3 has one single chip and the highest number of channels in the wavelengths I want to investigate. From these four sensors, I have concluded to use sensor number 3 for my experiments. Indeed, Mohebbian at al. *(Mohebbian et al., 2021)* used this sensor (the AS7262) to conduct two in vitro experiments, concluding that this is an ideal sensor for blood detection with various haemoglobin concentrations in either occult or severe bleeding.

The AMS AS7262 6-channel Visible Spectral sensor can detect wavelengths at 450 nm (Violet), 500 nm (Blue), 550 nm (Green), 570 nm (Yellow), 600 nm (Orange) and 650 nm (Red). This sensor has been purchased in a preassembled board by Pimoroni (Pimoroni Ltd., Sheffield). This board consists of the AS7262 sensor together with two white LEDs with colour temperature of 4000 ^oK, which in this work were not used. The board's dimensions are 19x21x4 mm. The sensor is connected to a Raspberry Pi

Figure 2.3. Pimoroni AS7262 Board. Dimensions 19x21x4 mm

Pico and a code written in Micro Python *(https://micropython.org/)*, (Appendix 1) is used to control and power it. The board is illustrated in Figure 2.3.

The experimental set-up used for my experiments is illustrated in Figure 2.4. Three LEDs with different wavelengths are coupled into a 4 cm integrating sphere. More specifically a 465 nm (blue, NSPB510AS, Nichia Corp., Japan), a 525 nm (green, NSPG500DS, Nichia Corp., Japan) and a 600 nm (amber, NSPA510BS, Nichia Corp., Japan) LEDs have been used. The choice of the LEDs wavelengths has been based on the sensor's spectral sensitivities, ranging from 450 nm to 650 nm. I wanted to use LEDs with wavelengths in close proximity but not identical to the sensor's peak sensitivities.

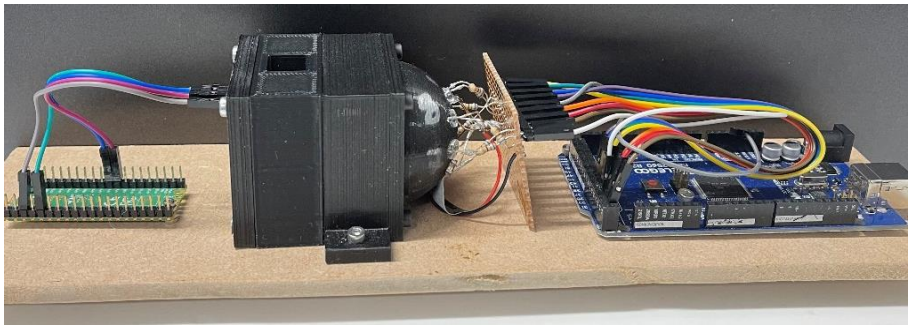

Figure 2.4. Photograph of the experimental set-up

These LEDs are connected with load resistors of 680 Ohm to the 5 V digital outputs of an Arduino MEGA board. The circuit is illustrated in Figure 2.5. The resistors' values have been chosen so that they would yield drive currents of approximately 4 mA. The output voltage capabilities of the Arduino are above the threshold voltages for all these LEDs.

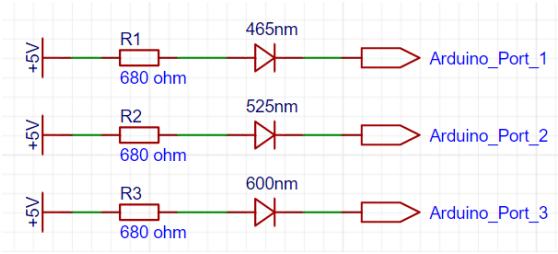

Figure 2.5. Schematic Diagram of LEDs connected to Arduino

An Arduino code (Appendix 2) has been written to power and control these LEDs, implementing time-multiplexing of the sources. Their light is scattered inside a 3D-printed integrating sphere (Figure 2.6.a) with 40 mm diameter,

brush-coated with 3 coats of titanium white colour (Winsor & Newton Professional Acrylic PW6), mounted in the sphere in 5 mm input ports (as illustrated in the cross section presented in Figure 2.6.b). It has been assumed that titanium white is practically spectrally white at all the different wavelengths we are investigating at this experiment. The sphere has a 6 mm output port, protected from the LED line of sight by a baffle. The ratio between total port surface and total sphere surface is 3.6 %. This percentage is within the acceptability range for integrating spheres *(Labsphere, 2022)*. The output port is proximity-coupled to a cuvette, in turn proximity-coupled to used sensor, that measures the transmitted light intensity at its spectral bands. The sensor's outputs are pre-calibrated by the manufacturers for linearity and offset. The system has been 3D-printed on a Creality Ender 3 Pro FDM printer (Creality, China) using a black PLA/PHA blend (colorFabb B.V., The Netherlands).

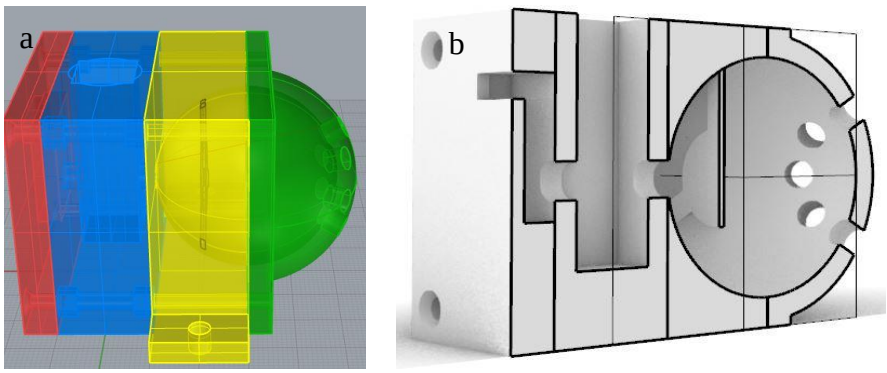

Figure 2.6. Schematic of integrating sphere used in the experimental set-up, a: CAD Design, b: Cross Section of Design.

The sensor communicates through a 3.3 V I^2C interface, and this communication is achieved by using a Raspberry Pi Pico (Raspberry Pi Foundation, UK) board, which operates at 3.3 V LVTTL (Low Voltage Transistor-Transistor Logic) levels. This is substantially simpler than e.g., using a logic level converter on an Arduino board, that operates at 5 V TTL levels. To perform a measurement of the light transmitted by the sample, each LED is switched on by the Arduino, warmed up for 1 s, the signal from each

channel of the senor is read by the Pico, with a 10 ms integration time, and the LED is then switched off. The process is repeated for each LED, one at a time. The light-tightness of the system is such that the impact of the ambient light is, effectively, negligible.

2.2.2. Sample Preparation

In order to test the set-up illustrated in Figure 2.4, a set of 18 samples with independent absorption spectra have been prepared. A set of 18 aqueous solutions of pure pigment solid watercolour paints (Winsor & Newton Artist's Professional Watercolours), which we assume having linearly independent spectra as traditionally used in painting, and not possible to emulate by mutual mixing, have been prepared at concentration of 0.05% w/w. The identificatory names and their manufacturer codes of these colour dyes are presented in Table 2.2. The reason professional water colours have been used to create the samples is that they only contain pure pigment, a small amount of binder and traces of a biocidal. Specifically, the half-pan preparation contains gum Arabic or synthetic glycol as a binder, and traces of 2-methyl-1,2-benzothiazol-3(2H)-one(MBIT) as a biocidal. While detailed information of the type of binder used is not available, both types of binder and the biocidal are, by definition, optically transparent as they are designed not to affect the colour of the paint. Therefore, their absorption spectrum can be neglected.

Table 2.2. Sample Pigments

Number of Sample	Pigment Name	Preparation	Manufacturer code
1.	Winsor yellow	Half-pan	PY154
2.	Lemon yellow	Half-pan	PY175
3.	Trans yellow	Half-pan	PY97
4.	Winsor orange	Half-pan	PO62
5.	Winsor red	Half-pan	PR149
6.	Alizarin crimson Hue Red	Half-pan	PR179
7.	Permanent rose	Half-pan	PV19
8.	Winsor violet	Half-pan	PV23

9.	Winsor blue	Half-pan	PB15
10.	French ultramarine	Half-pan	PB29
11.	Indanthrene blue	Half-pan	PB35
12.	Permanent sap green	Half-pan	PY139
13.	Winsor green	Half-pan	PY110
14.	Raw umber	Half-pan	PBr7
15.	Burnt umber	Half-pan	PY42
16.	Indigo	Half-pan	PB29
17.	Payne's gray	Half-pan	PB15
18.	Ivory black	Half-pan	PBk9

More specifically, each half pan of colour has been taken outside of its packaging with a tweezer. Then, a 50 ml sterile transparent plastic tube has been placed on top of a high precision scale. Using a small knife, each half-pan has been slowly ground until 5 mg of each colour, in the raw solid format, has been added to the sterile tube. 50 ml of room temperature distilled water had been pipetted to the tube. A small magnet has been placed inside each sample and the samples have been stirred for 5 minutes at room temperature using a Stuart UC151 magnetic analogue stirrer at a speed of 1000 rpm. Following the stirring, the solutions have been stored in dark glass jars (Belle Vous Round Amber Glass Jars, 240 ml with Black Screw-On Lids) to protect them from fading due to long-term light exposure. Out of this 50 ml master solution, 5 ml have been pipetted into sterile cups. To avoid scattering of the light due to particulate, the 5 ml samples have been filtered through polyethresulfone membrane filters with polypropylene housing, with pore size 0.45 μm (UK-PES25, AllPure Biotechnology, UK) in combination with Terumo 2.5 ml luer-lock syringes. The resulted 5 ml filtered samples have been stored in sterile cups.

Furthermore, samples with different concentrations have been prepared. Each of the 18 primary samples have been further diluted to create additional samples. As it will be verified later, on the results section, the initial

concentration chosen is the highest concentration compatible for appropriate measurements of absorbance. After this has been verified, I have created dilutions at 50% and 25% of the original concentration. From the 50 ml master solutions, I have pipetted into sterile cups 2.5 ml samples and 2.5 distilled wated to create the 50% samples and 1.25 ml sample and 3.75 ml distilled water to create the 25% samples. As before, to avoid scattering, the new 5 ml samples have been filtered through the polyethresulfone membrane filters and the luer-lock syringes.

To measure the samples absorbance, 4 ml square plastic cuvettes with a 10 mm light path and four clear sides have been used, covered with a lid to avoid sample contamination and evaporation (Figure 2.7). In order to calculate the standard deviation of our measurements, each cuvette has been rotated clockwise in order to have measurements from each of the 4 directions available from the cuvette.

Figure 2.7. Prepared filtered samples.

2.2.3. Testing

As abovementioned, the samples absorbance has been measured for each of the 18 samples and their dilutions. The reference light intensities were determined performing a measurement on a cell filled with distilled water, and then transmitted light signals were measured for each sample. The related absorbance A has been computed as defined in Equation 2.6.

$$A = \log_{10} \frac{I_0}{I} \qquad 2.6$$

where I_0 is the intensity of the light passing through the reference cell filled with distilled water and I is the intensity of light passing through the sample.

The primary issue aimed to be addressed through these experiments is to understand how many independent wavelengths channels the system can measure. This is achieved by using Matrix rank analysis, as per the following. We note that this analysis works only in the assumption that the system behaves linearly. For this reason, as a starting point, the linearity of the sensor needs to be verified. To achieve that, the normalized absorbance of the different concentrations in relation to the normalized absorbance of the 100% concentration of each sample has been plotted. The absorbance is calculated using Equation 2.1.

The sensitivity of the sensor is not particularly relevant in our case because we are dealing with heavily absorbent substances at high concentrations. The described sensor will detect blood (which is a bright absorber) into a situation where other high absorbers exist. The system's performance will be stretched to the highest absorbance it can handle and then the linearity between a value of 0 and the highest absorbance will be evaluated. In a spectrophotometry measurement, the absorbances handled should be lower than 1 *(Rodger et al., 2013)*. If the calculated absorbance is higher than 1, then the gap between transmitter and receiver needs to be reduced. Otherwise, there will be noise issues in the system.

Under these conditions, the sensor should have an output that is in linear proportion to the input. In reality, there is a deviation from this ideal linear dependence between input and output signal. The ratio between the maximum deviation between real and ideal curve (Δ_{max}) where the ideal curve is taken as the straight line joining the transfer function endpoints, and the full-scale value of the sensor (Y_{fs}) expressed as a percentage, is called End Point Straight Line (EPSL) nonlinearity. This nonlinearity is given by Equation 2.7:

$$Nonlinearity(\%) = \frac{\Delta_{max}}{Y_{fs}} * 100 \qquad 2.7$$

To calculate the nonlinearity of the sensor, I used Equation 2.7. I first plotted the normalised absorbance versus the different concentrations using the data from all the 18 samples. The ideal curve is represented as a straight line joining the endpoints of the observed data. Then, I determined the maximum deviation (Δ_{max}) between the real and ideal curves. This deviation was then divided by the full-scale value (Y_{fs}), and the result was expressed as a percentage.

By time-multiplexing each of the three used LEDs, each spectral channel of the detector reads three signals, associated with the three individual LED sources. For each of the three LEDs and for each detector channel, I have reconstructed from the datasheets the nominal spectral emissivity and sensitivity respectively, quantitatively retrieved from the datasheets using WebPlotDigitizer which is a utility that takes a graph and reverses it into data points *(Rohatgi, 2023)*. At this stage, the number of independent channels need to be established. To achieve that, I have created the absorbance matrix of these 18 pairs of all the 18 samples. In the absence of noise, the source-detector channel pairs measure independent information. Thus, the rank of the absorbance matrix can be used to calculate the number of independent channels. To evaluate the rank of the matrix, the number of non-zero eigenvalues need to be calculated.

To calculate the eigenvalues Matlab 2022a (The Mathworks, USA) has been used. However, in any physical measurement, noise is inevitably present, albeit small such as in our measurements, and it is independent from channel to channel. So, the estimation of the number of independent channels cannot be achieved by looking at how many independent signals exist, because due to their noise, all signals will be independent from each other. Therefore, the calculation of the rank of the matrix is not indicative of linear independence.

In general, the problem of estimating eigenvalue/es in the presence of an additive random noise is a non-trivial problem *(Edelmann et al., 1984)*, well beyond the scope of my PhD. In practical terms, however the eigenvalue

modulus remains above the order of magnitude of the noise level for a number of eigenvalues equal to the number of independent spectra, and the first eigenvalue is higher compared to the rest. The point where there is a decline in the value of eigenvalues, corresponds to the number of independent channels *(Edelmann et al., 1984)*.

2.3. Results

The 18 resulting products between source spectra and detector sensitivities are plotted in Figure 2.8, alongside a table of the peak wavelengths for readability.

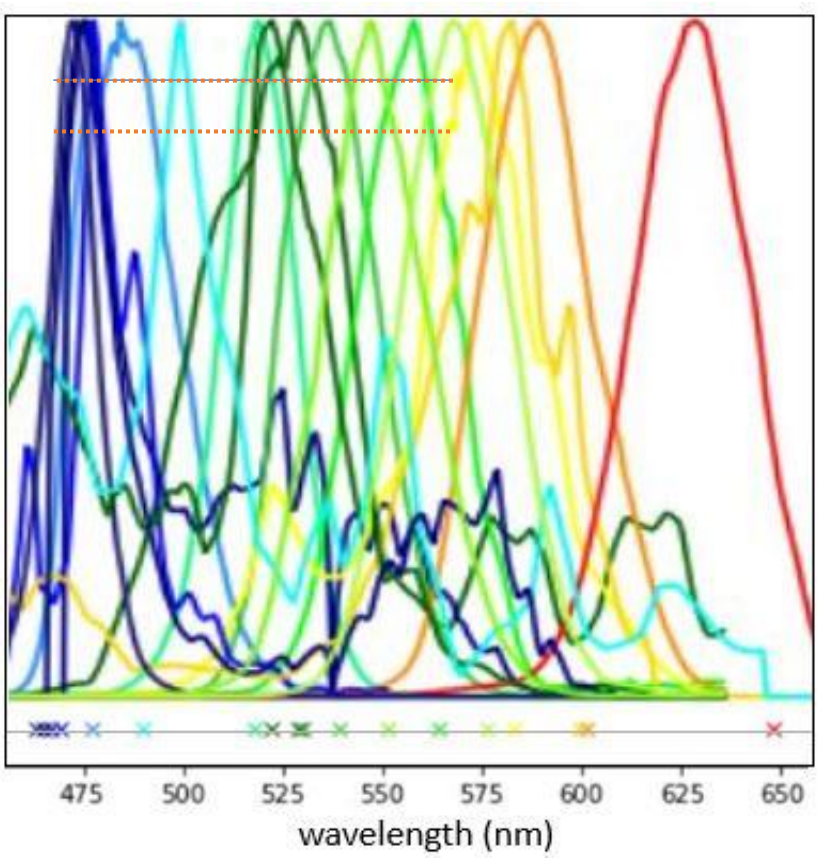

463	465	467	469	477	490	518	522	529	530	539	551	564	576	583	600	601	648

Figure 2.8. Normalized product between source spectra and detector sensitivity spectra, peak positions, and table of the peak wavelengths in nm.

The measured absorbance matrix, ordered by peak detection wavelengths numbered as in Figure 2.8 (columns) and sample numbers as in Table 2.2 (rows) is reported in Table 2.3. More specifically, the columns of the table

represent the peak wavelengths that have been calculated as the maximum of each spectrum extracted from the product between the three sources' spectra and the six detector's sensitivity spectra. Each row is one of the 18 used samples. The noise levels, as derived from the four measurements per sample, are below the limit of detection for most points, and reach a maximum of 0.5% of the mean spectral value.

Table 2.3. Absorbance Matrix. Rows represent the used samples and columns represent peak wavelengths

nm	463	465	467	469	477	490	518	522	529	530	539	551	564	576	583	600	601	648
1.	0.544	0.772	0.556	0.592	0.916	0.342	0.302	0.544	0.301	0.544	0.579	0.439	0.426	0.269	0.443	0.444	0.400	0.397
2.	0.447	0.530	0.515	0.509	0.535	0.497	0.500	0.544	0.602	0.544	0.559	0.564	0.574	0.554	0.506	0.542	0.520	0.560
3.	0.368	0.555	0.345	0.332	1.501	0.064	0.049	0.211	0.090	0.354	0.152	0.087	0.125	0.036	0.104	0.092	0.076	0.071
4.	0.243	0.345	0.278	0.262	0.372	0.152	0.087	0.301	0.067	0.243	0.278	0.196	0.146	0.069	0.211	0.198	0.134	0.126
5.	0.669	0.651	0.653	0.720	0.601	0.740	0.626	0.669	0.602	0.512	0.728	0.643	0.699	0.488	0.728	0.806	0.828	0.871
6.	0.192	0.247	0.278	0.262	0.225	0.196	0.106	0.269	0.163	0.192	0.306	0.196	0.247	0.081	0.339	0.342	0.348	0.284
7.	0.146	0.230	0.283	0.243	0.167	0.196	0.088	0.336	0.125	0.114	0.408	0.263	0.234	0.056	0.426	0.412	0.075	0.248
8.	0.368	0.304	0.477	0.447	0.171	0.865	0.668	0.637	0.426	0.269	0.942	0.740	0.699	0.388	1.198	1.184	1.089	0.954
9.	0.243	0.049	0.141	0.208	0.057	0.497	0.934	0.146	0.602	0.211	0.074	0.263	0.316	0.860	0.189	0.303	0.495	0.682
10.	0.192	0.182	0.195	0.208	0.192	0.228	0.296	0.243	0.275	0.211	0.213	0.246	0.275	0.296	0.213	0.241	0.280	0.302
11.	0.447	0.249	0.368	0.419	0.219	0.831	1.112	0.447	0.845	0.415	0.394	0.564	0.544	1.015	0.553	0.662	0.773	0.916
12.	0.301	0.311	0.255	0.262	0.362	0.196	0.294	0.243	0.243	0.336	0.249	0.263	0.243	0.438	0.194	0.202	0.208	0.230
13.	0.447	0.238	0.255	0.306	0.353	0.439	0.923	0.204	0.660	0.544	0.168	0.342	0.331	1.286	0.172	0.227	0.287	0.429
14.	0.192	0.243	0.199	0.196	0.270	0.112	0.108	0.160	0.125	0.172	0.199	0.138	0.145	0.104	0.156	0.156	0.140	0.138
15.	0.669	1.179	0.836	0.763	1.384	0.439	0.356	0.813	0.391	0.637	0.866	0.564	0.574	0.313	0.653	0.586	0.502	0.471
16.	0.669	0.463	0.602	0.669	0.452	1.041	1.639	0.637	0.845	0.637	0.579	0.740	0.813	1.150	0.772	0.958	1.233	1.513
17.	0.572	0.438	0.515	0.582	0.431	0.865	1.017	0.512	0.778	0.512	0.502	0.564	0.637	0.762	0.603	0.712	0.845	0.969
18.	0.257	0.288	0.265	0.276	0.300	0.228	0.155	0.269	0.079	0.254	0.279	0.263	0.176	0.152	0.256	0.261	0.177	0.178

In Figure 2.9, the normalised absorbance for all the 18 samples versus their different concentrations is presented. This allowed me to calculate the maximum deviation (Δ_{max}) between the two curves and compute the EPSL nonlinearity. With red line, EPSL is represented. Using Equation 2.7, the Nonlinearity is calculated.

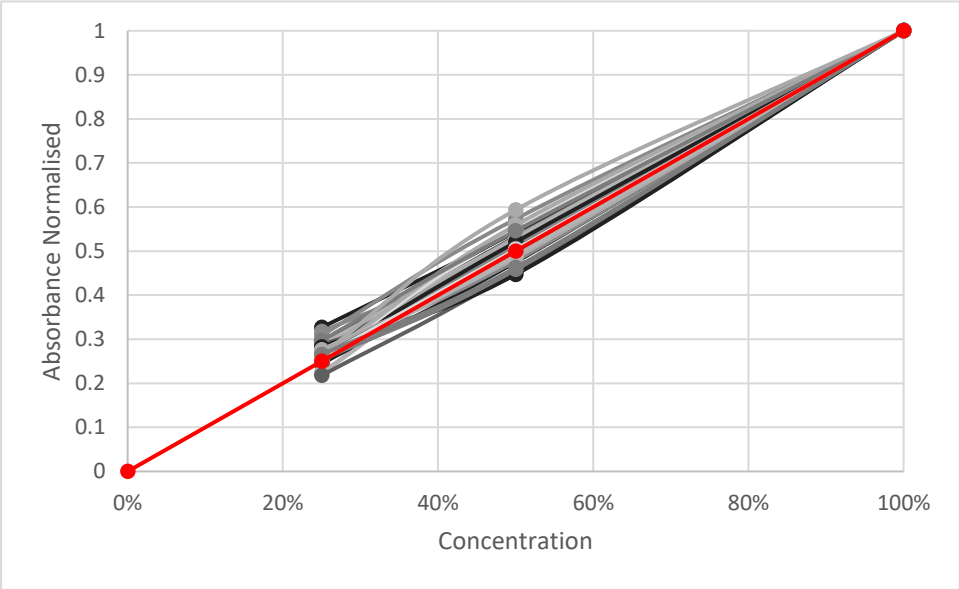

Figure 2.9. Normalised Absorbance versus different concentrations of the 18 samples. With red the best fit End Point Straight Line is represented.

$$Nonlinearity(\%) = \frac{0.6 - 0.49}{1} * 100 = 11\%$$

This calculation gives an 11% nonlinearity for the sensor's response, which reflects the deviation from the ideal linear behaviour.

Then, the matrix eigenvalue modulus vector, ordered by magnitude, is reported in Table 2.4.

Table 2.4. Eigenvalues of The Absorbance Matrix

3.8990	0.3432	0.3432	0.1257	0.1079	0.0974	0.0974	0.0772	0.0772	0.0729	0.0729	0.0476	0.0476	0.0281	0.0281	0.0220	0.0220	0.0037

Higher values

Lower values

In Table 2.5, the first eigenvalue (darker green shading) is close to 4, and the next 10 (light green shading) are in close proximity with each other. Their value does not significantly drop until after the 11th eigenvalue. The exact cutoff place is somewhat arbitrary and can only be calculated by considering the total error, which includes both noise and nonlinearity errors. Here, the cutoff is determined when the lower eigenvalues deviate from the linearity range. According to Edelmann *(Edelmann et al., 1984)*, this estimation suggests that the cutoff lies between the 11th and 13th eigenvalues, indicating that the number of independent channels ranges from 11 to 13.

2.4. Discussion

Commercial sensors for capsule sensing currently have limitations in terms of the number of wavelengths they can detect, with a maximum of six for compact devices. The ideal solution would be a small spectrometric detector with a high number of optical detection bands to identify different chromophores. Given the variety of substances in the gastrointestinal tract, including two types of blood, bile, and various food colours, the number of channels in existing sensors are insufficient for accurate detection. The substances to be detected have signatures in both the visible and near-infrared range, necessitating an increase in the sensor's detection channels to at least ten, without increasing the power budget.

Mohebbian and his team *(Mohebbian et al., 2021)* had created a system by combining three LEDs as transmitters and one diode as receiver. In their work they also conclude that having a sensor that is able to utilise more channels is important. They have combined two 6-channel sensors, and they proved that with this setup it is possible to distinguish between a sufficient number of different substances. Schostek and his team *(Schostek et al., 2016)* presented a capsule that is attached to the stomach and is able to detect bleeding, however it only utilises 2 LEDs, thus limiting the specificity of detection.

In this chapter, the main objective was to enhance an existing sensor's capabilities by creating a custom setup to increase the number of measurable wavelengths. At the time of my experiments, the sensors presented in Table 2.1 were commercially available. Of these four sensors, there is one that can detect 6 channels, using only one chip, at the power budget available in a capsule sensor. The AS7262 is chosen. At the time of writing the thesis, the commercial situation has not changed substantially. Advancements in sensor technology have led to the development of new sensors, yet they remain restricted to detecting only 8 channels. The AS7341 11-channel spectral colour sensor holds the record for the highest number of channels as per existing literature. However, it's important to note that out of the 11 channels this sensor claims to detect, only 8 are relevant. The remaining 3 channels, which are associated with flickering and white light, do not contribute any spectroscopic information.

In this thesis we have chosen the LEDs so that their wavelengths would avoid the peak wavelengths of the filters existing on the detector. This ensures that the products between the LED's spectra and the detector's spectra wields new and different curves from the original filters. By time-multiplexing these LEDs, each of the 6 spectral channels of the detector reads three signals, associated with the three individual LED sources. By utilizing this technique, the number of channels detected by the sensor is increased. The products of the source spectrum and the channel spectral sensitivity are illustrated in Figure 2.8.

There, we have 18 theoretical independent peaks. However, as already noted, some of the peak wavelengths are at close proximity with each other. Moreover, these peaks are difficult to be estimated quantitatively and reliably since the reconstruction of the source spectra and detector's sensitivity spectra had been based on the reconstruction of the peak shape from nominal datasheet plots and not on the actual data. 11 isolated wavelength peaks or

peak clusters are clearly identifiable. This tallies with the fact we identified 11 (or possibly 13) independent eigenvalues.

This is all based on the assumption that the used detector behaves linearly. Indeed, from Figure 2.9 the linearity is calculated. In this graph, the normalised absorbance versus the different measured concentrations for the 18 samples are being presented. It has been established that the rank of the matrix alone is insufficient to identify the number of distinct detectable by my system. Consequently, the eigenvalues have been computed. However, this calculation is only applicable under the assumption that my system behaves linearly. While the mathematics involved in calculating the eigenvalues is beyond the remit of this thesis, the most substantive outcome is that I can assess the differences between the eigenvalues only within a margin of error corresponding to my linearity error. Therefore, the non-linearity error of 11% implies that any differences in the eigenvalues less than approximately 11% are inconsequential for my experiment. I examine eigenvalue differences on the order of 50% (as per Table 2.4). Therefore, the level of nonlinearity is sufficiently low to permit progressing with further discussion of the eigenvalues. In conclusion, the detector exhibits satisfactory linearity in its performance.

In Table 2.4 the calculated eigenvalues are presented. From that table it is visible that their value does not significantly drop until after the 11^{th} value, indicating that the signal sequences for at least 11 source-detector channel pairs are linearly independent with each other. This is in agreement with the result acquired from the table with the peak wavelengths in the bottom of Figure 2.8. From this table it is clear that there is coherence between some wavelength peaks. The peaks are close to each other in certain paths of the spectrum. Thus, the detected channels are independent from each other but there is correlation between them.

Table 2.3 represents the absorbance matrix. The matrix consists of 18 rows, each corresponding to one of the 18 samples used in my experiments. Each

column in the matrix signifies a peak wavelength. The values of the absorbance on the matrix validates that the experiments are being conducted within the appropriate absorbance range. More specifically, the peak absorbance value measured is 1.513. These measured absorbances serve as a sanity check, confirming that the absorbance calculations conducted are within the acknowledged range for well-posed absorbance measurements *(Rodger et al., 2013)*.

At this point, this check assures me that I'm working with the correct concentrations. The ideal calculated concentration is one that yields a matrix within a range of 0 and 1. Within this suitable range for my experiments, I dilute to the necessary levels for the linearity tests I intend to conduct. It's important to note that I'm not aiming at detecting trace amounts of substances. The focus of this chapter is on determination of the proper number of absorbance channels within the absorbance ranges normally found within the intestine, aiming to optimize the accuracy and efficiency of spectral analysis for better understanding of intestinal health.

The experiments conducted in this chapter mark the initial phase in the construction of a capsule. They demonstrate that the number of channels in a commercially available sensor can be increased without augmenting the number of detectors used, but merely by expanding the number of utilised sources. This, both from a size and a power budget point of view is a much better approach. The next steps involve reducing the setup size and testing its ability to quantify blood in the presence of other chromophores.

These tests cannot be conducted in-vitro as the optical absorbance of blood alters once it leaves the body due to changes in the microenvironment *(Taylor-Williams et al., 2022)*. Hence, these tests need to be performed in-vivo. Although these tests have been planned, limited lab access due to COVID has necessitated the use of artificial dyes.

The next steps should address these two primary limitations. The miniaturization issue can be resolved by constructing a tethered capsule.

Afterwards, an in-vivo experiment with a tethered capsule should be conducted. Once the geometries and data processing are finalized, an untethered capsule should be built for the final experiments.

2.5. Conclusions

This chapter has shown a method to increase the number of channels in an optical detection system by using a wavelength sensitive detector and a set of optical sources appropriately chosen with respect to the wavelengths detected by the sensor. As far as we know, the idea and results presented in this Chapter are all a novel approach since we have been invited to the Annual International Conference of the IEEE Engineering in Medicine and Biology Society in 2022 to present them.

In the pipeline to develop a capsule, this Chapter has proven that by a simple, small system a high number of independent spectral detection channels can be achieved. The core limitations of this Chapter have been the miniaturisation of the system and the in-vivo testing to verify its ability to quantify blood. The next steps should be the construction of a tethered capsule and finally the in-vivo experiments. In any case, however, even with this initial demonstration, the results are suggestive that indeed, the number of independent multispectral channels has been augmented using multiplexed spectrally coloured sources. This idea can be used to explore the design of a new sensing capsule, with better specificity than the state-of-the-art.

By increasing the number of channels of a receiver, the data throughput is also increased, hence pushing the need to higher data rates. Since the RF communication utilised in existing capsule sensors has various limitations, it became essential for my research to design and construct a bespoke transmitter/receiver system. Prior to that, the first step would be to simulate the performance of this optical channel. If the simulations prove that optical communication through tissue is possible, then the optical channel can be

designed and built and then the technique presented in this Chapter can be utilized to increase my systems' performance even more.

CHAPTER 3

SIMULATIONS OF OPTICAL DATA TRANSMISSION THROUGH TISSUE

Parts of this chapter have been presented as an invited communication at the Annual International Conference of the IEEE Engineering in Medicine and Biology Society (EMBC 2019), entitled "*Optical communication Through tissue*" *(Katsafadou et al., 2019)*.

3.1. Introduction to the Chapter

The previous chapter focused on the experiments done to increase the number of channels in an existing sensor by incorporating a set of selected LEDs. The next step would have been to create a tethered capsule to miniaturise this setup. To achieve that, the primary objective would be to design a custom transmitter/receiver system. If a high-speed signal can be optically transmitted using this transmitter/receiver system, the detector's sensitivity can be improved by adding more LEDs to the transmitter and applying the method discussed in the previous chapter. However, there are significant challenges that could hinder the design's progress. One major concern is that optical communication through tissue might not be feasible due to the low signal strength that can be achieved after attenuation in biological materials. The inherent scattering and absorption properties of tissue can diminish the optical signal to levels that may be insufficient for reliable detection. Additionally, the limited speed of light transmission through tissue could introduce latency, further complicating high-speed signal transmission. These factors must be carefully considered when evaluating the practicality of this optical communication system. Thus, the initial step involves simulating the performance of this optical channel. If the simulations confirm the feasibility of optical communication through tissue, the optical channel can be designed and constructed.

The main idea of my PhD is that light is created by a transmitter, then it is scattered and absorbed by the patient's different tissue types and finally is collected by the receiver. Generally, photons in order to reach the receiver travel through various types of tissue with different optical properties. That

leads to significant loss of signal due to absorption of light from tissue. Furthermore, scattering causes light between a source and a detector to travel through multiple paths of different lengths, so that a narrow pulse of light at the source gets spread into a much wider pulse on the detector. This reduces the bandwidth of the signal, and it is a phenomenon known as multipath effect.

Thus, before progressing with the complex and time-consuming design and construction of this optical data link, simulations have been necessary to establish if after transmission of light through thick human tissue, the absorption and bandwidth are appropriate for data communication. Indeed, the bandwidth and the total signal reaching my receiver after traveling through thick tissue have been estimated. For these reasons, Monte Carlo simulations have been conducted to estimate these parameters to a level appropriate for a qualitative sanity check.

Steady State and Time Resolved Monte Carlo simulations have been conducted. The first set of simulations allows a first approximation of the total signal that reaches the receiver. The second set has been conducted to estimate the system's bandwidth limitations. While the exact calculation of the bandwidth would have been too complex for this PhD, it was essential to understand at least if the order of magnitude expected for the bandwidth is sensible for my application, or if we were committing some gross misestimate which would have halted the experimental work downstream.

Both types of simulations have been coded in C++ using Microsoft Visual Studio with heavy usage of multithreading on an 18-core computer with an Inter i9-7980 processor, to speed up the simulation. For the purposes of the simulations, the human body has been simulated as an elliptical prism, the transmitter has been placed in the centre

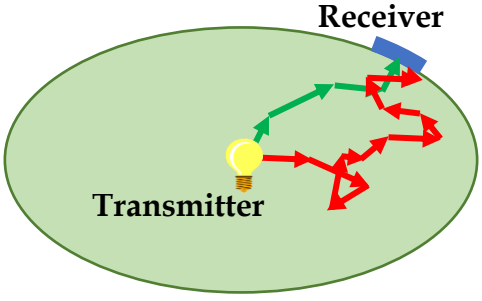

Figure 3.1. Cross-sectional view of the simulation of photons traveling through the body

of the prism and the detectors have been placed on its full outer surface, like illustrated in Figure 3.1.

After these initial simulations, a multilayer geometry has been simulated. For that geometry, the abdomen and the palm of the hand have been used. The abdomen is the main structure under investigation for my transmitter/receiver modules, when used to detect bleeding in the gastrointestinal tract. The palm of the hand has been simulated because it is easier to access it experimentally and it is indeed being used on the next Chapter as a test of the performance of my system. Furthermore, it is a structure with multiple tissues, similar to the abdomen, but it is thinner, and thus a detector could, theoretically, easier receive the signal passing through it. Therefore, the palm of the hand provides a simpler test case for my simulations. These simulations lead to an estimation of the total signal able to be received by my designed circuit after passing through the tissues under investigation.

3.1.1. Theory

Biological tissues are complex structures. They can be considered as turbid media, which is heterogeneous and has strong scattering properties. Hence, the propagation of light through tissue is a complex process. *(Halder, 2020)*, *(Jacques et al., 2013)*. When light transmission through tissue occurs, light is absorbed and scattered by the different constituents of the tissue (cells, cell organelles, blood vessels etc.) *(Abita et al., 2004), (Ackermann et al., 2008)*. In order to describe the process of light propagation through tissue, it is useful to define the tissue's optical properties.

The main absorbers of human tissue are haemoglobin, melanin, bilirubin and betacarotene *(Jacques et al., 2013)*. An absorption coefficient μ_α can be defined as the probability of photon absorption per unit path length *(Wang et al., 1995)*. It can be calculated by equation 3.1:

$$\mu_\alpha = \frac{1}{l_\alpha} \qquad 3.1$$

where l_α is the absorption length, which is the average free path before an absorption event occurs. The units for μ_α are mm^{-1} *(Halder, 2020)*.

The highly anisotropic, heterogeneous biological tissue makes describing light scattering a challenging task. We can define a scattering coefficient μ_s as the probability of photon scattering per unit path length *(Wang et al., 1995)*. This can be calculated by equation 3.2:

$$\mu_s = \frac{1}{l_s} \qquad 3.2$$

where l_s is the scattering length which is the average free path before a scattering event occurs. Units for μ_s are mm^{-1} *(Halder, 2020)*. In most cases, the absorption coefficient of tissue has lower values compared to the scattering one. Thus, scattering is the dominant process taking place in light travelling through biological tissue *(Ritter et al., 2014)*.

Another useful parameter used to characterize light transmission through tissue is the anisotropy factor (g). After light is scattered, the amount of the light that follows a forward trajectory is deflected by an angle θ. Anisotropy g is used to describe the fraction of forward direction scattering and it can be calculated by the following equation 3.3:

$$g = \int_0^\pi \rho(\theta) * cos(\theta) * 2\pi \sin(\theta)\, d\theta =< cos(\theta) > \qquad 3.3$$

where $\int_0^\pi \rho(\theta) * 2\pi \sin(\theta)\, d\theta = 1$.

Here, the anisotropy g is used to describe the direction of scattering, and it is dimensionless with values ranging from -1 (backward scattering) to 1 (forward scattering) *(Halder, 2020)*. In tissue, forward scattering is the most common one and g typically varies between 0.8 and 0.95 *(Ritter et al., 2014)*.

Human tissue contains various light scattering and absorbing constituents, each with specific optical properties that change depending on the wavelength of the light that passes through them *(Stevenson, 2009)*. There is a specific region of wavelengths, an optical tissue window in the range of 600-1300 nm where photon absorption and scattering from human tissue are minimum *(Abita et al., 2004), (Ackermann et al., 2008)*. This region is optimal for the more

efficient transfer of light through tissue. For this reason, in this thesis light with peak wavelength at 850 nm has been used for my experiments.

Another parameter used for long-distance propagation is the reduced scattering coefficient μ'_s. This is defined as in Equation 3.4:

$$\mu'_s = \mu_s(1 - g) \qquad 3.4$$

For long-distance propagation (many times the mean free scattering path, which is in the order of 0.1mm), it is possible to describe scattering as isotropic, with scattering coefficient μ'_s instead of μ_s, and neglecting g.

3.1.2. Monte Carlo Simulations

The growing number of applications of light in various medical areas and the inhomogeneous nature of the skin led to the requirement of designing models used to measure optical properties of tissue, such as reflectance and transmittance. Historically, Monte Carlo is the gold standard for short scale simulations of propagation of light through biological tissue while Photon Density Waves are for longer scale simulations *(Fishkin et al., 1993)*. Using modern computing technology, native processor speed and multithreading capabilities, allow Monte Carlo to be used more often even for longer scale simulations.

The Monte Carlo (MC) method is widely used to provide a numerical solution in various fields, such as astrophysics and ocean optics, but it is also applied to tissue optics. The main idea of MC method is to solve the propagation problem by simulating the local interactions of photons travelling through the tissue. These photons are launched in the position of an optical source. They travel in a straight line, until they undergo a collision, that causes scattering and/or absorption, and then are scattered randomly until they undergo another scattering event, absorption event or exit the tissue. For scattering, the polar angle θ and the azimuthal angle φ represent the change in the photon's direction.

$$p(\theta) = \frac{1}{4\pi} \frac{1-g^2}{(1+g^2+2g\cos\theta)^{3/2}} \qquad 3.5$$

$$\varphi = 2\pi\eta \quad 3.6$$

where η is a uniform random number between 0 and 1.

Generally, multilayer types of tissue are simulated by assigning different values for μ_α and μ_s in different positions. This allows simulation of non-homogeneous tissue, such as skin, vascular, urinary bladder, and uterine walls. Simulations through MC are highly accurate. However, the main drawback of this method is that for the large number of photons, necessary for an acceptable variance of the simulation results, it needs a prolonged computation time *(Tuchin, 2015), (Baran et al., 2019)*.

There is a great variety of problems that can be solved by Monte Carlo simulations. It can be used to simulate the reflectance and transmittance of one or multiple wavelengths for simple or more complex, multilayer geometries and depending on the researcher's needs various results can be extracted. However, in all the different types of simulations, the initial idea is that rather than simulating individual photons, a set of photons starting off in the same direction are bundled together as a packet with a weight proportional to the energy of the total photons in the packet. The packets travel in the tissue and collide with inhomogeneities. At each collision, they are scattered and partly absorbed. Part of the packet energy is lost at each absorption event. Next, the next travel step length is chosen by following the equation:

$$l = -\frac{ln(\xi)}{\mu_a + \mu_s} \quad 3.7$$

where ξ is a random number between 0 and 1. At each step, the photon packet loses part of its weight due to absorption from the tissue. This weight W is given by equation 3.6.

$$W = W_{initial} * (1 - \Lambda) \quad 3.8$$

$W_{initial}$ is the initial weight of the packet. Λ is called albedo and it ranges from 0 when the medium absorbs light completely to 1 for a completely scattering medium. Its value is given by the ratio between the scattering cross section (σ_{sca}) and extinction cross section (σ_{ext}) by the equation:

$$\Lambda = \frac{\sigma_{sca}}{\sigma_{ext}} \quad 3.9$$

The remaining packets are the ones that get scattered. When the weight of the remaining packets is lower than a pre-chosen threshold, there is the need to decide whether a packet needs to be terminated or propagated. Packets of photons cannot just be killed when the weight is below the threshold because this will not result in energy conservation. To maintain the energy, an algorithm called 'roulette' is used. In this algorithm, not all packets are terminated when their energy becomes too low. Rather, packets with a weight that fall below a set threshold are terminated with a probability (1-p), where p is a positive constant smaller than 1, typically in the order of 0.01. When a packet below threshold is not terminated, its weight is multiplied by 1/p. On average, therefore, the packet energy is conserved, while, indeed, sooner or later all packets are terminated, avoiding divergence of the computation time. When the packet of photons passes the external boundary of the medium, the remaining weight of the packet contributes to the measured reflectance or transmittance. In the case of reflection, the photon packet returns back to the medium for further propagation. In the case of transmission of the packet, it is captured, and a new packet is launched, and the procedure is repeated.

3.2. Methodology

3.2.1. Steady State Simulations

For the purposes of my PhD, both steady state and time resolved simulations have been conducted. I have simulated the human abdomen as an elliptical prism with different dimensions. For the two axes of the ellipse model (axis a and axis b) ten different dimensions have been tested, with ratio of a:b=1:2, covering the range from small test samples to an average adult (a axis varied from 1 cm to 10 cm in an 1 cm step) *(Ergonomics Center of North Carolina, 2017)*. This setup allowes for a broad investigation of light propagation through tissues of varying thicknesses, reflecting the diversity of clinical scenarions.

For my simulations, the transmitter has been placed in the centre of the prism and the detectors are placed on the full outer surface of the prism. This configurations gives the highest possible signal but also the worst possible multipath effect, simulating a worst-case scenario in terms of signal distortion due to multipath effect propagation. For the initial Monte Carlo steady state simulations, muscle and fat tissues have been used to simulate the path that the light will travel through. This provides an initial understanding of the signal that reaches the receiver after interacting with the different tissues. From these simulations, the Relative Integrated Intensity for the different dimentions of the ellipse model have been calculated.

Integrated Intensity refers to the total strength of the signal over a specified surface. In this case, it is the sum of the individual signal intensities from all the different packets of photons that are reaching the receiver. Relative Integrated Intensity means that the integrated intensity is compared to a reference value, in this case to the signal produced by the transmitter. By comparing the input and the output signals, the original signal reaching the detector can be determined. This gives a measure of the efficiency of the data transmission. A higher ratio indicates that a larger portion of the transmitted signal is reaching the detector, suggesting a more efficient transmission. Furthermore, Relative Integrated Intensity is a measure of how much light is left, after being absorbed and scattered by the different types of tissue.

After demonstrating that the type of tissue indeed affects the quantity of the signal reaching the detector, a multilayer geometry code has been written and used in order to simulate the human palm of the hand and the human abdomen. These types of tissue have been simulated as an ellipse with the dimensions presented in Table 3.1 for each layer of tissue. A diagram of the multilayer geometry used is presented in Figure 3.2.

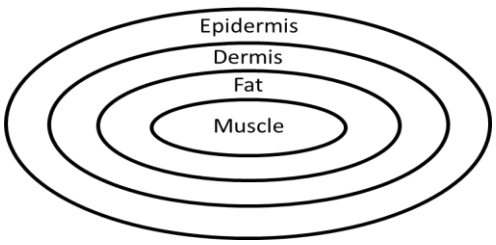

Figure 3.2. Diagram of Multilayer geometry used.

Lundstrom et al. *(Lundstrom et al., 2018)*, Morimoto et al. *(Morimoto et al., 2017)*, Kim et al. *(Kim et al., 2012)*, Derraik et al. *(Derraik et al., 2014)* and Khiao et al. *(Khiao et al., 2019)* report that the average thickness of each layer of tissue for the palm of the hand and the abdomen are as presented in Table 3.1.

Table 3.1. Average dimensions of each layer of tissue (Lundstrom et al., 2018), (Morimoto et al., 2017), (Kim et al., 2012), (Derraik et al., 2014), and (Khiao et al., 2019)

Type of Tissue	Epidermis thickness (cm)	Dermis thickness (cm)	Fat thickness average (cm)	Muscle thickness average (cm)
Palm of hand	0.15	0.3	0	0.43
Abdomen	0.006	0.2	2.38	1.03

The three optical properties of human muscle, fat, dermis and epidermis at 940 nm have been assumed from the literature *(Prahl, 2017), (Chatterjee et al., 2019), (Dai et al., 2004)* and are stated in Table 3.2. These properties are crucial for accurately simulating light propagation through these tissues.

Table 3.2. Properties of different Tissue at 940 nm (Prahl, 2017), (Chatterjee et al., 2019), (Dai et al., 2004)

Tissue	Absorption (cm^{-1})	Scattering (cm^{-1})	Anisotropy
Epidermis	0.2446	105.57	0.91
Dermis	0.2577	105.57	0.91
Fat	0.170	54.2	0.8
Muscle	0.401	58.1	0.5

For these simulations, N packets are assumed to be initially launched from a position (x, y, z) set to (0, 0, 0) (centre of the prism) with a weight of 1. For this simulation, packets have been launched in batches by using multi-threading coding. The number of threads, number of photon batches and batch size are all variable parameters in the written code and can be altered accordingly. The objective of my study has been to conduct a simulation that would simulate the emission of the maximum number of packets. Nevertheless, it was imperative that these simulations were designed to conclude within a

reasonable timeframe in the order of less than 24 hours, thereby avoiding prolonged periods of operation resulting in multiple days of waiting for a result. Additionally, it was crucial that the simulations yielded a variance that was qualitatively significant in the order of less than 10^{-5}, which would allow for meaningful interpretation and application of the results.

To proceed with my experiments, a total number of 10^{10} packets of photons per simulation have been chosen. This number was determined based on preliminary tests that balanced computational efficiency and accuracy. The thread count is approximately four times the number of system cores as per standard C++ practice. This has been used to compute the batch size I used.

These packets of photons take steps and they interact with the biological tissue. After each step, part of their original weight is lost. The program allows the user to select the absorption and scattering coefficients as well as the anisotropy according to the type of tissue used (Table 3.2). The Monte Carlo codes I used are presented in Appendix 3 (Steady-State) and 4 (Time-Resolved). A flowchart of the steady state code is given in Figure 3.3.

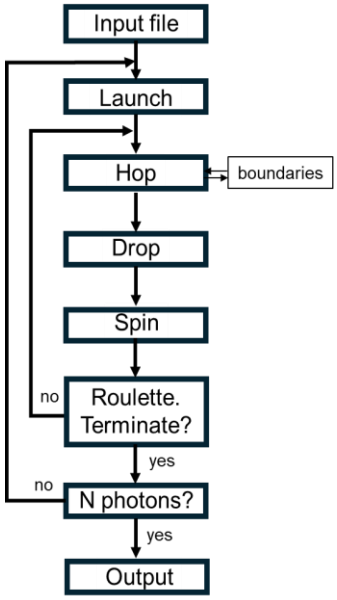

Figure 3.3. Flowchart of Monte Carlo Steady-State simulations

During the transmission of the packets through the tissue, each packet of photon is allowed to *HOP* to another position, *DROP* weight to the absorption, *SPIN* into a new direction and check if the process of *ROULETTE* has killed the packet. After the *HOP* command takes place, the packet is moved by a stepsize *s* to a new position (ux, uy, uz). The stepsize is randomly calculated by a pseudo-random number generator function (*RandomNum*). For that purpose, we created our own generator, using Knuth's portable linear congruential algorithm *(Knuth et al, 1981)*, since we wanted to ensure that there

is negligible autocorrelation of any order through our algorithm and the native C++ algorithm did not offer that.

After the movement of the packet, it interacts with the tissue and part of its weight is dropped due to absorption. The *DROP* function calculates the new weight of the packets of photons that continue to get scattered and absorbed in a new trajectory. If g=0 then the scattering is isotropic, while if g>0 then the Henyey-Greenstein *(Zhang et al., 2016)* function is used to mimic the scattering in anisotropic biological medium. During the *SPIN* function, the deflection angle theta of the packet and the azimuthian angle psi are randomly selected. Afterwards, their cosine and sinusoidal values of both angles are calculated and used to generate the new trajectory of the packets' movement. Finally, the previously mentioned *ROULETTE* method is used to decide whether a packet is terminated or not. If the weight of the packet is less than a predetermined by the user threshold, then roulette is followed. By using the *RandomNum* generator, a number is selected and if it lower than *CHANCE* (a number chosen by the user), then termination of the packet occurs. In the opposite case, the packet's weight is increased by a factor of *1/CHANCE* and the propagation continues. After the termination of the packet, a new packet of photons is launched *(Prahl, 2017)*.

The next step of the steady-state Monte Carlo C++ code is to use the necessary equations to calculate the total power (W) of the signal reaching the surface of the model ellipse together with its standard deviation. These equations are presented here. Equation 3.10 gives the total power and Equation 3.11 shows how the standard deviation of the power has been calculated.

$$P = \sum_{i=1}^{N} \frac{E_i}{dt} \qquad 3.10$$

where E_i is the energy of the i-th photon packet, N is the total number of photon packets and dt is the time interval.

$$\sigma_P = \sqrt{\frac{1}{N-1}\sum_{i=1}^{N}(\frac{E_i}{dt} - \bar{P})^2} \qquad 3.11$$

Where $\bar{P}$ is the mean power calculated as in Equation 3.12:

$$\bar{P} = \frac{1}{N}\sum_{i=1}^{N}\frac{E_i}{dt} \quad 3.12$$

The number of packets that contribute to each signal are also extracted. The results of these simulations will provide valuable insights into the behavior of light in tissues, informing the design and optimization of light-based medical devices.

It is worth to note that at this Chapter I am doing an estimation check, so only order-of-magnitude noise considerations have been made. In my system I will have the optical shot noise and the noise of my electronics (transimpedance amplifiers, preamplification stage etc). To calculate the power spectral density of the optical shot noise, the following equation is used:

$$S(f) = 2h\nu\bar{P} \quad 3.13$$

where $h\nu$ is the photon energy with h being the Planck's constant and ν the frequency of the light and $\bar{P}$ is the average power of the signal. As abovementioned, for my simulations I have used the optical properties of human tissue at 940 nm. This resulted in a frequency calculated from Equation 3.14 as:

$$\nu = \frac{c}{\lambda} \quad 3.14$$

where c is the speed of light in vacuum and equals to $3*10^8$ m/s and λ is the wavelength. Thus, the frequency of light equals to 319 THz. The Planck's constant is 6.62607015×10^{-34} J*Hz^{-1} so the photon energy is calculated as $2.11*10^{-19}$ J.

3.2.2. Time Resolved Simulations

Another important factor of my optical data link has been to establish its bandwidth. Previous research by Fishkin and Gratton *(Fishkin et al., 1993)* calculated the attenuation of a sinusoid using Photon Density Waves. However, their work was limited to a semi-infinite, homogenous tissue and for a sinusoidally intensity-modulated point source of light. Additionally, Varotsos et al. later calculated the theoretical bandwidth in different optical

communication channels *(Varotsos et al., 2019)*. However, given that the multipath effect depends on the relative positioning of sources and detectors, the geometry of this positioning and of the tissue affects the bandwidth. Indeed, the geometry they were using on this paper with the out of body transmitter and the in-body units (photodiodes) in a straight-line configuration was different compared to the geometry I was simulating at the time. I wanted to simulate a geometry that would replicate as closely as possible the idea of an in-body transmitter and an outside-body receiver.

For the time-resolved simulations, the code and procedure are similar with the above mentioned. The main difference is that at time zero there is an impulse of photon energy delivered from the transmitter towards the receiver (Appendix 4). This energy is isotropically delivered towards the human tissue through time. The transit time is estimated by accumulating the pathlength through the whole simulation. From this, we can reconstruct the pulse propagation time for each packet path. This allows a reconstruction of the pulse shape when it exits the tissue. As the body is modelled as an ellipsoid, different positions on the ellipsoid correspond to different geometrical paths, in turn yielding different packet paths. For this reason, the output packet's pulses have been collected over 100 positions on the surface and averaged. The procedure after the spatial distribution of packets of photons is similar to the steady state simulations (subchapter 3.2.1.).

The frequency response of the system is the Fourier transform of the pulse response. Therefore, after these time-resolved Monte Carlo simulations, a custom-made Matlab code has been used to determine the Fast Fourier Transform (FFT) analysis of the resulted normalised signals. From the resulting FFT, the -3 dB point, which is where the signal is halved, has been found. The frequency corresponding to this point gives the bandwidth of the channel.

3.3. Results

3.3.1. Steady State Simulations

Upon conducting a series of trials, I determined that the optimal configuration for achieving these objectives was to utilize 80 threads and 1000 batches, with each batch comprising 10,000,000 packets. This configuration resulted in a total of 10^{10} packets of photons per simulation. This approach effectively balanced the need for a high package count with the practical considerations of simulation duration and meaningful output.

After the above-mentioned simulations have taken place, the results illustrated in Figure 3.4 have been obtained. The y axis is in logarithmic scale, and it represents the relative integrated intensity of the signal. The x axis represents the dimensions of the a-axis of the ellipse model. For each value of the a-axis, the corresponding value on the b-axis is double. From these graphs, it can be noticed that as the detector moves further away from the transmitter (ellipse's dimensions increase), the signal's amplitude is decreased.

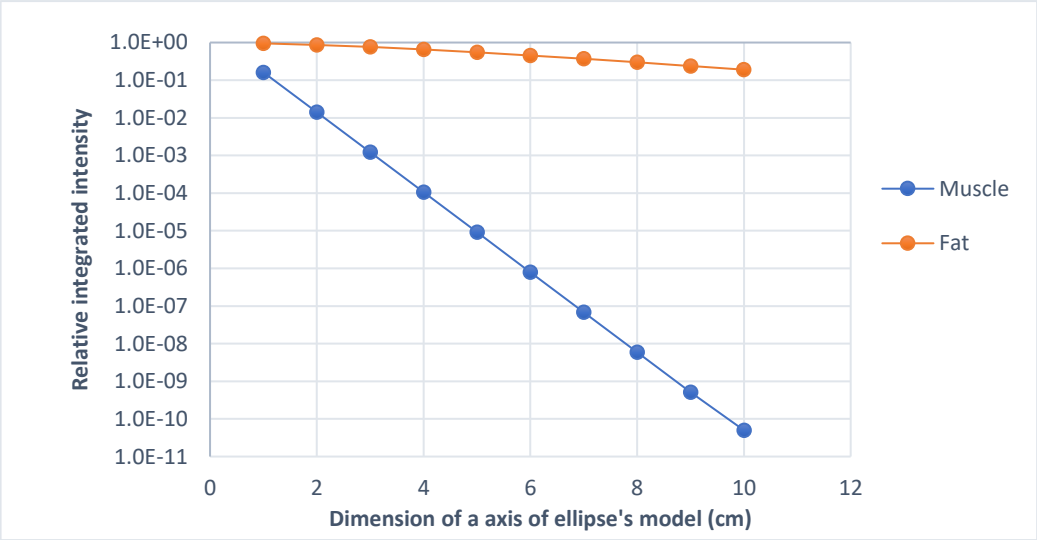

Figure 3.4. Graph presenting the relative integrated intensity in fat and muscle tissue in relation to the dimensions of the a axis of an ellipsoid model. Error bars are smaller than the dots in the diagram and thus are not visible.

For all the different signals represented in Figure 3.4, their standard deviation has been calculated. Since each signal corresponds to 10^{10} packets of photons

reaching the detector, each of these packets of photons corresponds to a calculated signal intensity. For a geometry with specific dimensions, in a specific type of tissue, all the contributed signals from the packets have a standard deviation that is automatically calculated from the MC code. Because these values are small, they cannot be noticed in the graphs and thus they are presented in Table 3.3.

Table 3.3. Standard Deviation of Total Signals for Muscle and Fat.

a-axis (cm)	b-axis (cm)	Standard Deviation of Signal for Muscle g=0.5	Standard Deviation of Signal (W) for Fat g=0.8
1	**2**	± 4.7980E-10	± 1.6430E-10
2	**4**	± 9.0644E-10	± 4.2511E-10
3	**6**	± 1.0001E-9	± 5.7847E-10
4	**8**	± 9.5225E-10	± 8.9179E-10
5	**10**	± 9.6505E-10	± 9.4916E-10
6	**12**	± 2.2822E-10	± 9.9976E-10
7	**14**	± 2.0548E-10	± 1.0924E-9
8	**16**	± 1.7943E-10	± 9.8980E-10
9	**18**	± 2.5549E-10	± 9.1514E-10
10	**20**	± 7.0868E-11	± 9.1194E-10

After demonstrating that the type of tissue indeed affects the quantity of the signal reaching the detector, a multilayer geometry code has been written and used. The Monte Carlo simulation resulted that when a batch of 10^{10} photon packets is launched, the ratio between the output power and the input power is calculated as presented in Table 3.4.

Table 3.4. Calculation of the ratio between the resulted from the simulations signal reaching my detector and the resulted from the simulation signal produced by the transmitter in the palm of an average hand and an average human abdomen.

Type of tissue	Output power in mW	Joules in 1 second	Output Photons in 1 second	Output Photons in 1 period	Out / In
Palm of average hand	0.9215	$0.9215*10^{-6}$	$0.37*10^{13}$	$0.37*10^{7}$	$0.37*10^{-3}$

Average human abdomen	0.9977	$0.9977*10^{-6}$	$0.401*10^{13}$	$0.401*10^{7}$	$0.401*10^{-3}$

3.3.2. Time Resolved Simulations

The next step has been to run the time resolved simulations in order to understand the bandwidth limitations of my system. The same simulation conditions have been used for pure fat tissue, pure muscle tissue and multilayer tissue in the palm of hand and in the abdomen. The time resolved simulation for fat and muscle for a circular geometry with radius of 5 cm and 20 cm have been plotted. The results are illustrated in Figures 3.5 and 3.6 respectively. The y axis in all graphs represents the normalised total amount of signal reaching the detector. The x axis represents time intervals in seconds on the left parts of the graphs and frequency in Hz on the right parts of the graphs. This shows how the signal's amplitude changes over time and across different frequencies. With a red line, the -3 dB point is illustrated.

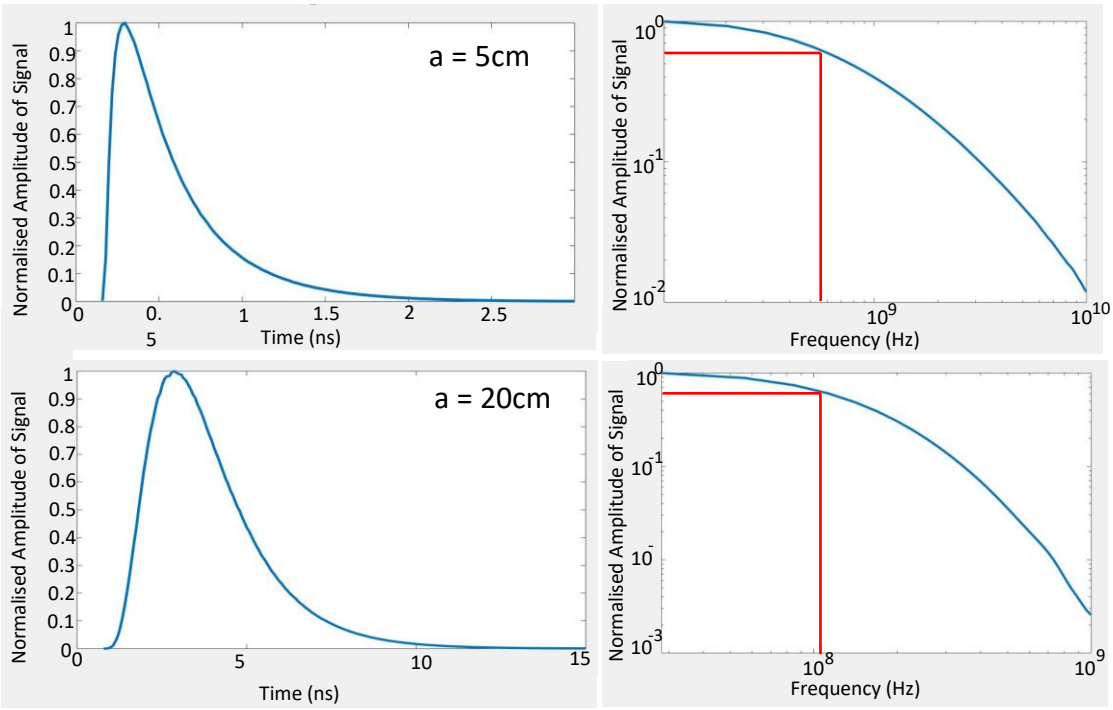

Figure 3.5. Fat tissue. Left: Normalised amplitude of signal through time, Right: FFT analysis of signal in logarithmic scale. With red, the -3 dB point is illustrated. Top: a=5 cm, Bottom: a=20 cm.

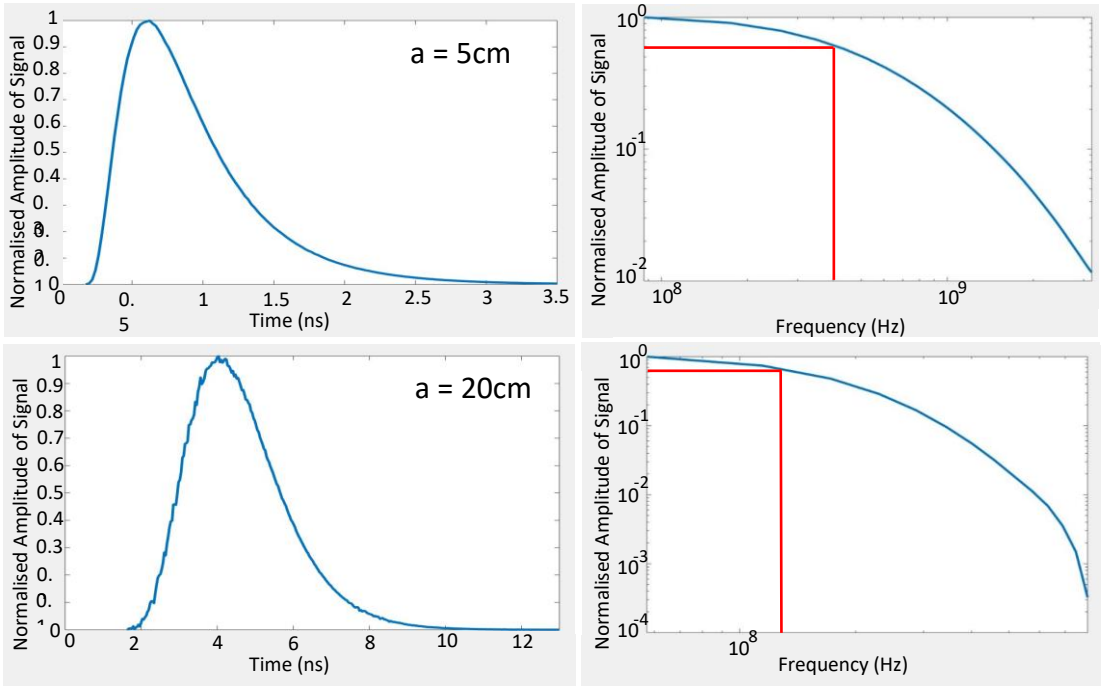

Figure 3.6. Muscle tissue. Left: Normalised amplitude of signal through time, Right: FFT analysis of signal in logarithmic scale. With red, the -3 dB point is illustrated. Top: a=5 cm, Bottom: a=20 cm.

From Figures 3.5 and 3.6 it can be noticed that as the thickness increases, the signal attenuation also increases, which is evident from the steeper decline in the bottom graphs. With a red line, the 3 dB point, which is where the signal power has halved, is illustrated. The resulted frequencies have been 5.5 GHz in 5 cm of fat, 100 MHz in 20 cm of fat, 2.5 GHz in 5 cm of muscle and 200 MHz in 20 cm of muscle.

To conclude if the calculated attenuation is low or high, the noise density of the acquired signals needs to be calculated. At an average value of 5 cm of fat tissue, from my simulations, when I launch 10 billion packets of photons, the total output signal is 0.552 mW (Figure 3.4) and the bandwidth 5.5 GHz (Figure 3.5 upper right part), resulting in a $7.4*10^{-9}\ W/\sqrt{Hz}$ noise spectral density, while for 5 cm of pure muscle the output signal is 0.1 mW (Figure 3.4) in a bandwidth of 2.5 GHz (Figure 3.6 upper right), resulting in a $2*10^{-9}\ W/\sqrt{Hz}$ noise spectral density.

To calculate the power spectral density, Equation 3.13 has been used. For 5 cm of fat tissue, the average power is $0.552*10^{-3}$ J/s and for 5 cm of muscle it is $0.1*10^{-3}$ J/s. Thus, the power spectral density of the optical shot noise for fat equals to $7.32*10^{-31}$ J^2/s and for muscle equals to $1.33*10^{-31}$ J^2/s.

3.4. Discussion

After having finalised the simulations and having acquired the results, the next step has been to understand if these results are consistent with the literature and if the signal is indeed sufficient to allow me to move forward in the creation of a similar system in the lab.

For the simulations, I placed the transmitter in the centre of the ellipsoid tissue phantom because I wanted to simulate the worst possible conditions. Placing the transmitter in the centre results in the maximum distance the light can travel from my transmitter to my receiver and to the worst multipath effect. Therefore, if the receiver is able to collect sufficient amount of signal under those conditions, then the creation of a system that would be functioning in even better, in reality, conditions is justified for the next steps of my PhD.

Figure 3.4 presents the relative integrated intensity of signal for only muscle and only fat tissue for different dimensions of the ellipse phantom I used as geometry. More specifically, if I launch photon packets that will pass through 6 cm of pure muscle tissue, the relative intensity of my signal will be 10^{-6}. This means that the signal strength is reduced significantly as it travels through muscle tissue. If the initial power of the launched packets of photons is 1 mW, the power of the received signal will be 1 nW. If the signal passes through a greater depth of muscle tissue, for example 9 cm, the intensity drops further to 10^{-9}, resulting in a received signal power of 1 pW.

Using a standard silicon photodetector with a sensitivity of 0.5 A/W means that for every watt of optical power incident on the detector, 0.5 A of electrical current is generated. With a received signal power of 1 pW, the resulting current would be in the order of pA. However, it's essential to assess this

current relative to the noise present in the system to determine its adequacy. By applying Ohm's law to a typical load of 100 MΩ, the corresponding voltage would be in the microvolt range. To understand whether this signal can be effectively distinguished from noise, we can utilize the noise estimate from equation 3.12 to compute the signal-to-noise ratio. A ballpark estimate suggests that while this setup might work for larger signal sources, it may not be sufficient for weaker signals. Therefore, building a physical device for experimental validation may be more practical than refining simulations at this stage.

The propagation distance for a source placed in the middle of the human body and collected on the skin surface in the closest point, is approximately 8-10 cm. As a conclusion, according to the above graphs, in fat I will not have any problem to transfer my signal, I have no noise issue. However, when I have an only-muscle tissue, I will not be able to get almost any signal. The human body is somewhere in between. Additionally, in real world, the capsule will never be in the exact centre of the human body. This in combination with the fact that the tissue under investigation will never be just pure muscle led to the conclusion that realistically, we are in a region that progressing in an experimental phase will make sense.

More specifically, muscle tissue absorbs and scatters light more than fat tissue, leading to a rapid decrease in signal strength with increasing depth. Therefore, under regions with significant muscle bulk, the signal transmission could indeed be very low. However, it might still be possible for this to work under certain conditions. For example, using more powerful light sources can help to ensure that light reaches the detector even after passing through thick muscle tissue. Also, by using light at wavelengths that are less absorbed by muscle tissue the transmission can be improved and finally even when the signal is weak, it might still be possible to detect it by using advanced signal processing techniques to extract the signal from the noise.

Figures 3.5 and 3.6 present the time resolved simulations results and their -3 dB point. This is a critical parameter for analysing signal attenuation and propagation characteristics within specific mediums like biological tissues. From the comparison between only fat and only muscle tissue, it can be concluded that the propagation of the signal appears to decrease the bandwidth. Furthermore, the bandwidth in thick muscle tissue is higher than in thick fat tissue which means that the pulses in muscle are slower, meaning that I have an increased absorption of signal in that type of tissue and thus worse multipath effect.

The shape of the pulses received by the detector, is not a Gaussian pulse. Additionally, there is a significant zero-frequency component (DC component) and thus the modulated signal is going to have both DC and AC components that affects the shape of this graph. From the presented frequency response, I get the response from the AC component. But I do not get my DC component. In principle, the DC component increases the noise of a signal. In this calculation, I am neglecting it as I am only estimating orders of magnitude for my noise. Generally, the detectors I wanted to use, need to be AC coupled because they need to cut off the ambient light that could affect my measurements. But even in the absence of ambient light, from these graphs it seems that my attenuation is going to give a DC component and thus the detectors need to be AC coupled.

The frequency response of the signals is presented in the right part of the graphs. Fishkin and Gratton (*Fischkin et al., 1993)* experimentally measured that the frequency in a semi-infinite tissue geometry (after 10 cm of tissue thickness) would be 120 MHz, so similar values to the ones I found from my simulations. This range is enough to allow me progress to the experimental phase of my PhD, as it gives some reassurance on a reasonable chance of success.

3.5. Conclusions

This chapter has shown the simulations taken place to establish if it is possible for an optical signal to be transmitted through thick human tissue. Monte Carlo simulations were conducted to estimate these parameters. Steady State simulations provided an initial approximation of the total signal reaching the receiver, while Time Resolved simulations estimated the system's bandwidth limitations. These simulations, coded in C^{++} and run on an 18-core computer, modelled the human body as an elliptical prism with the light source in the middle and the detectors on its surface. Further simulations used multilayer geometries of the abdomen and palm of the hand to estimate the signal received by the detectors.

There are challenges in using light for communication through biological tissues. The signal strength decreases with the depth of the tissue, resulting in very weak signals, even for relatively thin tissue. Furthermore, light-based techniques in medical imaging and communication face additional challenges, as the light often has to pass through various layers of different types of tissue. This necessitates the use of sensitive photodetectors and amplification techniques to detect and measure the signals. Understanding tissue-specific differences in light absorption and scattering is crucial for the development and optimization of light-based techniques.

At the time the work was done, the findings that the bandwidth, signal intensity, and noise levels appeared compatible with data transmission from inside the abdomen to an outside receiver were considered novel, and this work was presented, as an invited presentation, to the 2019 session of the IEEE Engineering in Medicine and Biology Conference.

Upon using the Monte Carlo simulations to confirm that the intensity and the bandwidth of an optical signal passing through human tissue can be sufficiently detected by an out-of-body receiver, the next step has been to design and construct a bespoke transmitter and receiver system. This process

and the test conducted with that system are presented in the following Chapter.

CHAPTER 4

DESIGN OF THE SUBSYSTEMS

4.1. Introduction to the Chapter

Building upon the foundation laid in the first Chapter, the next step has been to present the evolution of a variety of capsule sensors in the second Chapter. Most of them rely on RF communication to transmit data, which inherently limits the bandwidth they can achieve. This limitation has been highlighted in numerous studies, including those by Swain et al. *(Swain et al., 2010)* and Ciuti et al. *(Ciuti et al., 2011)*. However, as concluded in the third Chapter, there is a compelling case for the development of a system that employs optical communication to relay information from within the body to the external environment.

On the basis of Chapter 3, in this chapter I describe the implementation of a tethered capsule that transmits data through tissue using an optical data link. This capsule has demonstrated a data transmission rate superior to the current state-of-the-art for endoscopic capsules at the time of my experiments. Herein, I outline the process of constructing my system, the methods employed to evaluate its performance, and the approach taken to validate its functionality. During the limited time of my PhD, I did not want to deal with the problem of miniaturisation of my system. I wanted to build something that I could then test with a reasonable amount of effort while still being able to control its performance.

My system is based on the transmission of a signal from a tethered capsule to an external receiver. The tethered capsule would be placed inside the human body while the receiver goes outside of the body. The tethered capsule is attached with a wire to a controller/driver. The receiver is consisting of an array of 40 photodiodes. It is attached to an amplifier system and to an offline decoder. A diagram of my system is

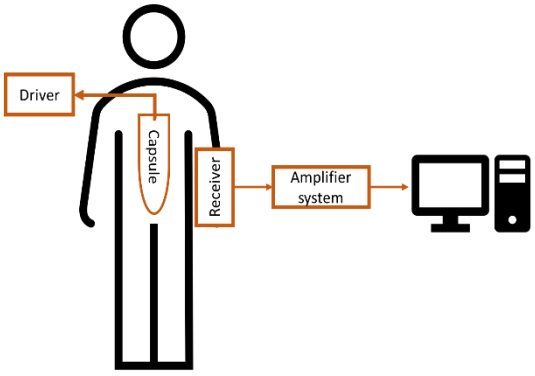

Figure 4.1. Diagram of my system

presented in Figure 4.1. Once I built this system, I tested it. For my tests I initially used a tissue phantom, and I transmitted a square wave through it. Then, I used biological tissue and more specifically my finger, palm of hand and arm and I transmitted a square wave through them. The final step has been to transmit an image through biological tissue from the internal capsule to the outside receiver and then to decode it.

4.2. Methodology

In the upcoming chapter, I will detail the process of constructing and testing the designed tethered capsule for optical signal transmission. The first step involved building the capsule, which consists of a transmitter and a receiver. The transmitter integrates a VSMY1850X01CT-ND infrared LED, selected for its optimal wavelength of 850 nm, ideal for minimizing photon absorption in human tissue. The receiver consists of a series of photodiodes BPW34FS (OSRAM, Germany) and amplification circuits. Following assembly, I conducted initial tests in air to evaluate signal performance and determine the optimal operating conditions. Subsequently, I implemented optical filters to refine the signal quality further. The next sequence of experiments involved testing the capsule's signal transmission through a liquid tissue phantom created from milk, facilitating a controlled environment to simulate biological tissue properties. This rigorous testing phase enabled me to assess the capsule's capability to transmit data through various mediums, laying the groundwork for trials on actual biological tissues. Therefore, the final phase of the testing involved my finger, palm of the hand and arm to test the performance of the designed tethered capsule.

4.2.1. Tethered capsule

The circuit diagram of the designed tethered capsule is reported in Figure 4.2. The tethered capsule contains a single infrared LED. The used LED is the

VSMY1850X01CT-ND emitter (Vishay Intertechnology inc., USA) with specifications presented in Table 4.1.

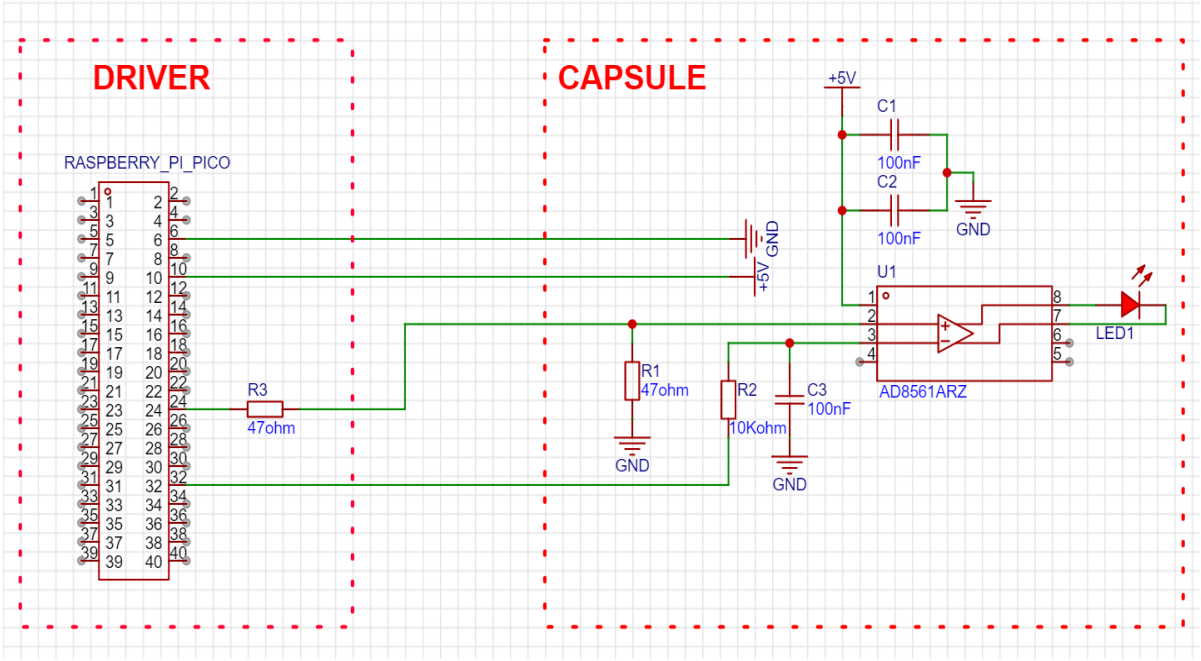

Figure 4.2. Circuit diagram of tethered capsule.

Table 4.1. LED specifications

Wavelength (nm)	Dimensions (mm)	Forward Voltage (V)	Rising time (ns)	Radiant Power (mW)
850	2x1.25x0.85 (package form 0805)	1.65	10	50

The 850 nm wavelength has been chosen because, as mentioned in the previous chapter, there is a tissue optical window in the range of 600-1300 nm where photon absorption and scattering from human tissue are minimal. Thus, this region is optimal for the most efficient light transmission through tissue.

To drive this LED, an ultrafast single supply differential output comparator, the AD8561 (Analog Devices, United States), has been used, with 7 ns propagation delay and supply voltage at +5 V. The comparator has two inputs

and a single differential output. As a component, a comparator compares its two inputs with each other and gives a positive output when signal 1 is greater than signal 2 while negative output when signal 1 is smaller. Therefore, it creates at its output on-off pulses. I used a single differential output comparator because it is faster in depleting the stray capacitance of the LED compared to a single ended comparator. Basically, the LED has a stray capacitance in parallel with the LED. If I was using a single ended comparator, it would need more time to discharge this capacitance. Thus, the differential output comparator speeds up this process.

In my circuit, as can be noticed from Figure 4.2, I have connected a 5 V signal to the positive input of the comparator, which acts as a reference voltage and a square wave to the negative input of the comparator. The purpose of applying a square wave to the negative input is to compare it with the reference voltage at the positive input. Furthermore, I have incorporated a low-pass filter R_2C_3 (R_2=10 kΩ and C_3=100 nF) into the circuit following the square wave signal. This low-pass filter has a cut-off frequency of 158 Hz. The inclusion of the low-pass filter serves to remove any high-frequency components present in the square wave signal, allowing only the desired low-frequency components to be input into the comparator. This ensures that the comparator is making its comparison based on a clean, noise-free signal, thereby improving the accuracy and reliability of its output. When the signal of the square wave is above a threshold voltage, the positive output of the comparator is high, while when the signal of the square wave is below that threshold, the negative output of the comparator is high. This threshold voltage has been set from the output of my filter. By connecting the two ends of my LED to the two outputs, the LED is flashing according to the frequency of the patterns of the drive signal.

The LED's light intensity is controlled by a bit stream signal, generated by a Raspberry pi Pico (code in Appendix 5) in a data rate ranging from 10 kHz up

to 15 MHz. Pin 24 is connected to a 5 V signal and Pin 32 to the square wave, both generated by the Raspberry pi Pico.

The LED and the circuit that drives it, have been assembled in a tethered PCB with dimensions of 20*9.3 mm. This PCB has been encapsulated using a water clear epoxy (832WC). For the bit stream signal, the ground, and the power supply to reach the capsule, two 2-way ribbon cables have been used, transferring the signal from the Raspberry pi Pico. The combination of these units is illustrated in Figure 4.3.

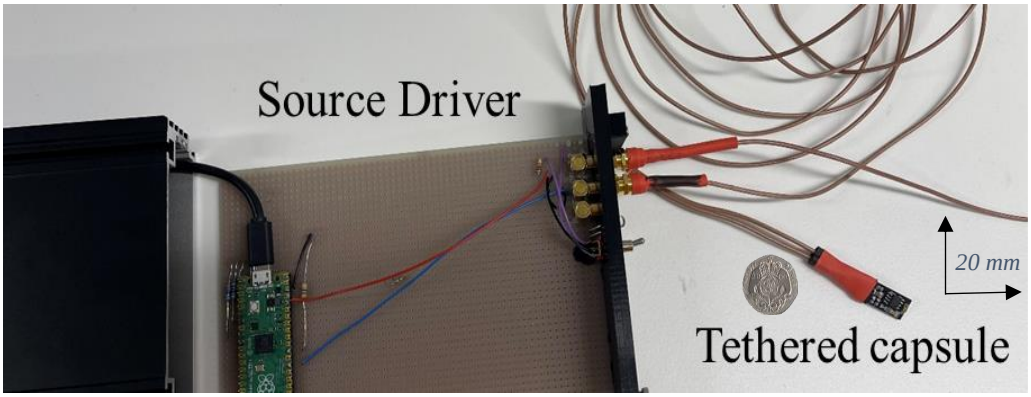

Figure 4.3. Capsule with source driver. A 20 pence coin is added for reference.

4.2.2. Receiver

After having finalized the tethered capsule, the next step has been to design and test the receiver. This receiver contains two major circuits, the on-patient antenna circuit, and the amplification circuit. The on-patient antenna circuit contains the photodiodes and the transimpedance amplifier circuit which is responsible for converting the received optical signal to voltage with a lead impedance appropriate to drive the connecting cable to the receiver. This circuit contains in total 40 photodiodes and 4 transimpedance amplifiers with outputs in parallel. The photodiodes used for my circuit are the BPW34FS (OSRAM, Germany) silicon photodiodes with rise time of 20 ns and active area of 7 mm^2.

As transimpedance amplifier, the OPA380 precision, high speed transimpedance amplifier (Texas Instruments, United States) has been chosen, with a low input voltage noise of 5.8 nV/$\sqrt{Hz}$ for a frequency f>1 MHz. For an optimum result, each transimpedance amplifier circuit is driven by 10 photodiodes that have been connected in parallel with each other. This results in a bigger surface area of detection while at the same time not reducing the bandwidth. This circuit is presented in Figure 4.4. The PCB with the 40 photodiodes is presented in Figure 4.5.

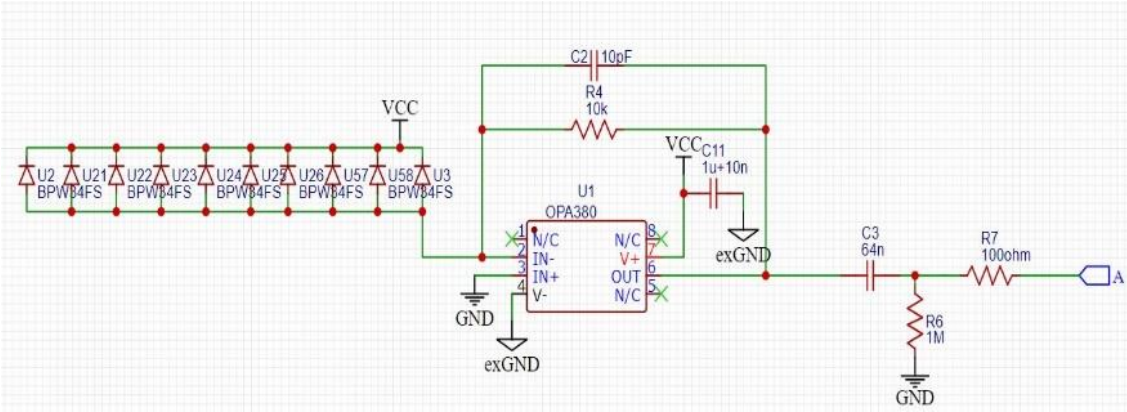

Figure 4.4. Transimpedance amplifier circuit with 10 BPW34 photodiodes. This circuit has been replicated 4 times.

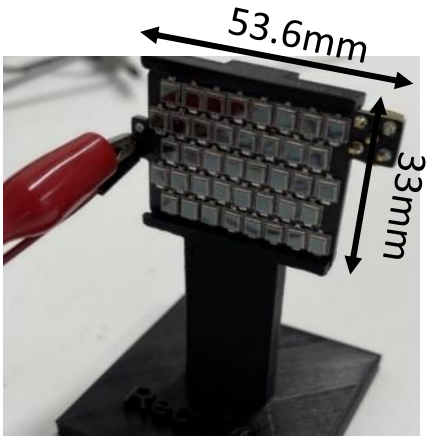

Figure 4.5. PCB comprised by 40 photodiodes.

A passive high pass RC filter is used after each transimpedance amplifier, created by the C_3 capacitor and the R_7 resistor with a cut-off frequency of 25 kHz. This capacitor is also used for AC coupling of my signal. AC coupling

has been used to filter out the DC signal coming from the output of the op-amp. Finally, a resistor connected with the capacitor towards the ground is used. That resistor (R_6) acts as a pull down and it normalises the ground to avoid a floating output.

4.2.3. Amplifier system

The signal collected by the 40 photodiodes, after passing through the transimpedance amplifier, moves to the amplification circuit which is responsible for the amplification of the received signal. The same transimpedance op amp (OPA380) has been used for that purpose. In order to amplify the signal, expected to be small as per the simulations in Chapter 3, we know by experience that a dynamic range of approximately 20 dB is required. Therefore, to obtain the best signal to noise ratio (SNR), the gain has been set in order to have a noise level of 10% of the output range. Basically, I am using all the output range I can use.

The first amplification stage is presented in Figure 4.6. The circuit in Figure 4.4 is replicated four times. The symbol B is used to show where all these four replications are connected.

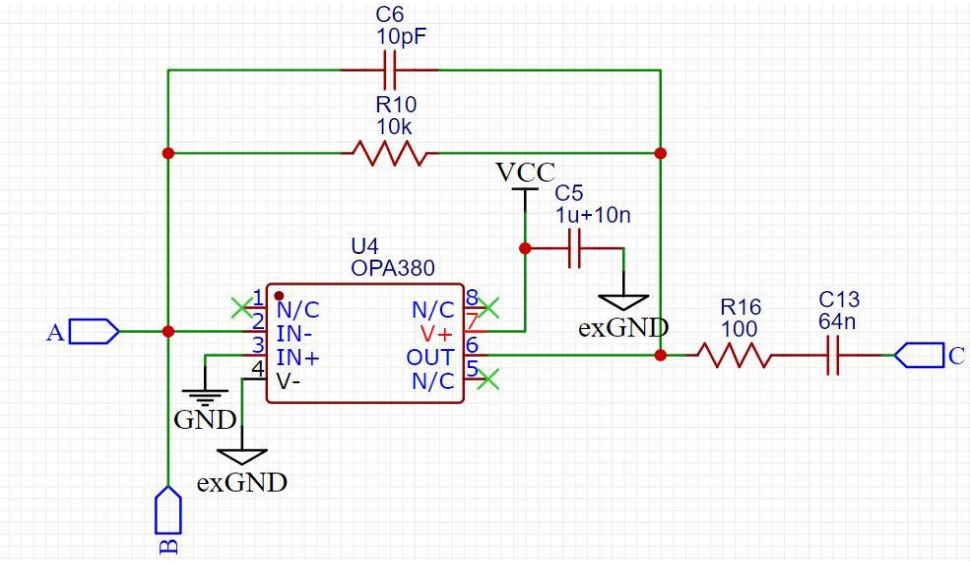

Figure 4.6. First stage amplification circuit

In the amplification stage, the gain of the inverting op-amp configuration is being set by the two resistors R_7 and R_{10} as G=100. The feedback resistor and capacitor of each op-amp have been set following guidance from the datasheet. The resistor's value has been set to 10 kΩ to achieve the desired gain. The feedback capacitor has been calculated to give a GBW=$90*10^6$ as C=5 pF, which is an estimate of the stray capacitance of resistor R_{10}. This theoretical calculated value of 5 pF resulted in slightly noisy signal, so after trials we concluded that 10 pF, in combination with the 10 kΩ feedback resistor, has been a better compromise between bandwidth and noise for this circuit's performance.

After each gain stage, another RC filtering has been added together with the 1 MΩ pull down resistor. Then, the second gain amplification stage is introduced with an identical configuration, presented in Figure 4.7.

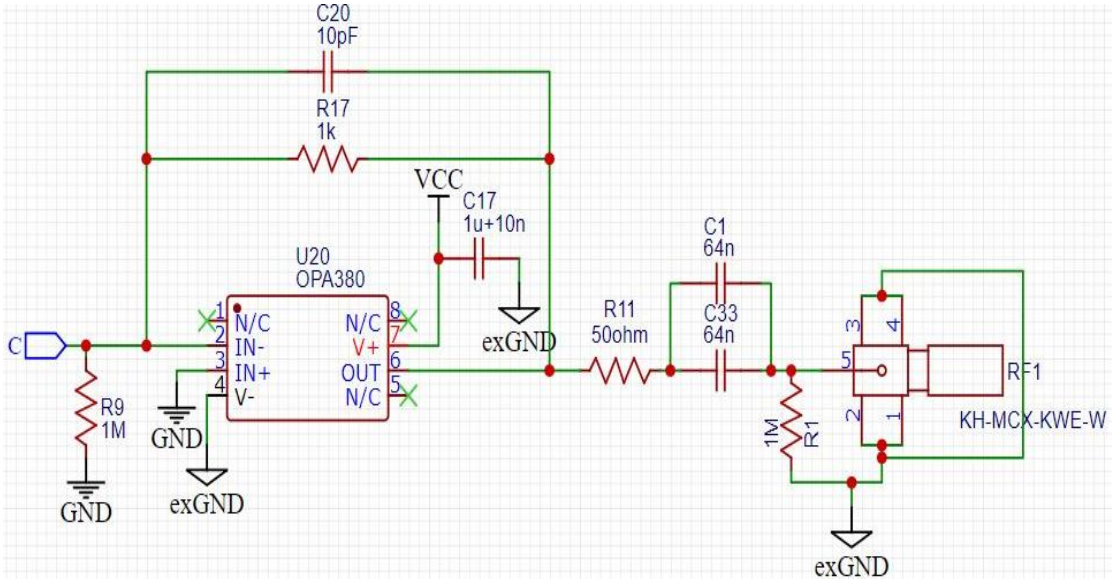

Figure 4.7. Second stage amplification circuit and termination of signal.

At the end of the circuit, an MCX connector is coupled to R_{11} resistor (50 Ω) for impedance matching. This MCX connector leads to a coaxial cable with impedance of 50 Ω. Thus, this R_{11} resistor, which value matches the impedance of the cable, acts as a load resistor, and helps the minimisation of the reflections through this transmission line.

In a real-life configuration, multiples of the PCBs described are going to be used. They are designed to be placed in a belt configuration around the waist of the patient with the photodiodes facing the patient's body and the output connectors facing the opposite direction.

All the PCBs presented in this Chapter have been designed in EasyEDA software (Shenzhen Jieli Technology Co Ltd, China) and have been printed by JLCPCB manufacturer (China). Then, I soldered them in our lab by using the SMD291SNL10 solder paste SAC305 in a 10-cc syringe 35g T3 Mesh (Chip Quik, United States). After applying the solder paste to the pads of my PCB, I placed it inside a reflow oven. The oven has been initially turned on at high temperature for 90 seconds until it reached 150^{o}C. Then, the temperature has been increased to 175^{o}C for another 90 seconds. When it reached the highest temperature of 249^{o}C (approximately after 240 seconds in total), the oven has been turned off and its door has been left open for 1 minute, for the oven and PCB to reach room temperature. The Figure with the temperature profile of the solder paste used is presented in Figure 4.8.

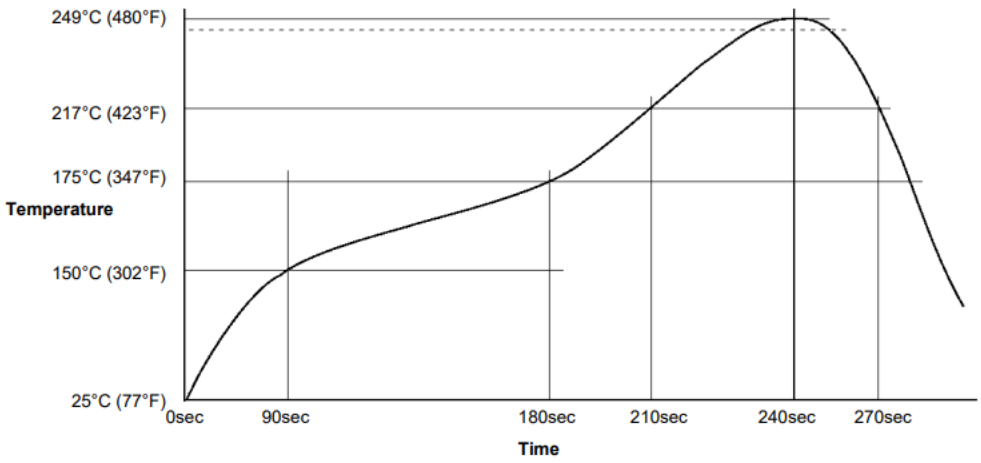

Figure 4.8. Reflow profile for Sn96.5/Ag3/0/Cu0.5 solder assembly (SAC305 solder paste).

4.2.4. Testing

During the first year of my PhD, a tissue phantom has been built to perform tests prior to testing my system on tissue. Tissue phantoms are widely used in order to simulate optical properties and different geometries of tissues. Generally, a stable and reproducible tissue mimicking phantom is required to establish reliability of an experiment's results *(Lualdi et al., 2001)*. There are two types of phantoms, liquid, and solid ones, both with advantages and disadvantages. When the propagation of light through tissue is studied, phantoms consisting of separate scattering and absorbing components are often used.

The most commonly used liquid tissue phantom is based on Intralipids which is a standard fat emulsion of phospholipids micelles and water and is used as a scattering medium. In most experiments it is used in combination with India ink which acts as an absorber. Other commonly used substances utilized as scatterers are homogenized milk, non-dairy cream, wax, agarose, a blood and yeast suspension, polyester microspheres, and micron-sized latex spheres *(Lualdi et al., 2001), (Firbank et al., 1993), (Wagnières et al., 1997)*. As absorbers, inks, food colouring or industrial dyes have been mostly used *(Hebden et al., 2006), (Firbank et al., 1993)*.

The main disadvantage of the materials used for the construction of liquid tissue phantoms has been that they are not stable over prolonged periods of time. Furthermore, due to their liquid nature, another material needs to be added to them in order to acquire a non-homogenous phantom *(Firbank et al., 1993)*. The main advantages of liquid tissue phantoms are that they are readily available, they are reproducible and cost effective *(Pogue et al., 2006)*.

Solid phantoms overcome the above-described disadvantages. In most cases they are constructed either by transparent hosts (polymers, silicon, or gelatine) or by light-scattering materials like wax *(Beck et al., 1998)*. Most common materials used as solid tissue phantoms *(Hebden et al., 2006)* are Delrin (highly scattering plastic), RTV rubber, colouring pigment added in paraffin wax, ink

and intralipids added in agar, and haemoglobin and intralipids added in gelatine.

Their main advantages are that they are resistive to weathering, they have good melting properties, heat resistance, resistance to chemical and durability. The main disadvantages are poor tear resistance, low thermal conductivity, poor tear strength and high viscosity.

For the purposes of this PhD, milk is used as a liquid tissue phantom due to its ease of production, reproducibility, cost effectiveness and its properties which are similar to intralipids.

To fabricate the tissue phantom, cast acrylic sheets have been ordered and cut to a specific round shape by a laser cutter. The design of the phantom is presented in Figure 4.9. Creo software (PTC, Boston) has been used to create it. The phantom's diameter has been designed to be 200 mm. The acrylic sheets have a thickness of 6 mm each. In order to manipulate the thickness of the device, and thus the thickness of the tissue, different number of acrylic sheets have been used for the experiments conducted.

In Figure 4.9.a, the top plate of the phantom is illustrated. With LEDs placed in the opal window of the top plate, light is going to be sent inside the phantom. In Figure 4.9.b, the bottom plate is shown. After the light passes through the phantom, it is collected by photodiodes placed outside of the opal window of this bottom plate. From two small holes at the top and bottom plate, milk is going to be dropped inside the phantom's internal cavity. In

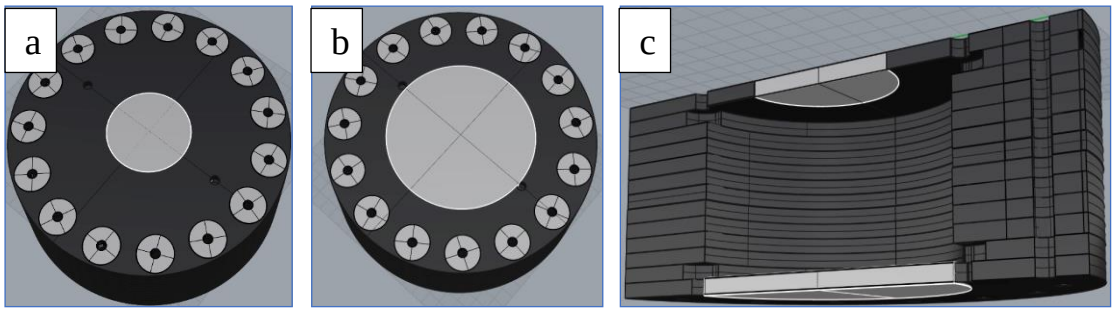

Figure 4.9. Design of Tissue Phantom. a) top plate b) bottom plate c) slice.

Figure 4.9.c, this cavity is presented. The photodiodes detect the light that passes through the milk.

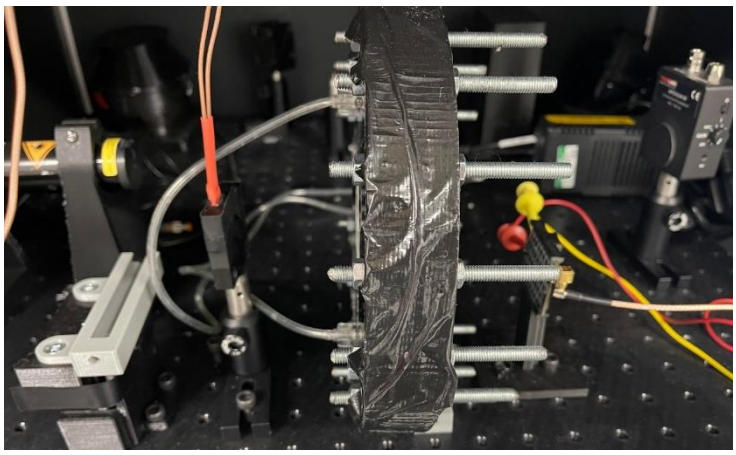

Figure 4.10. Data transmission setup through tissue phantom

Once the system presented in Figure 4.1 has been built, I tested it. For my tests, I placed the transmitter on the one side of my sample and the receiver on the other. For initial measurements, I transmitted a signal through 5 cm of air and then through the tissue phantom. The tissue phantom has been filled with 450 ml of full-fat milk by a syringe and has been placed on the optical bench, stabilised by 3D printed holders (Figure 4.10).

To run the experiment to test the performance of my system through the air, my transmitter and receiver have been placed inside the black out box (Figure

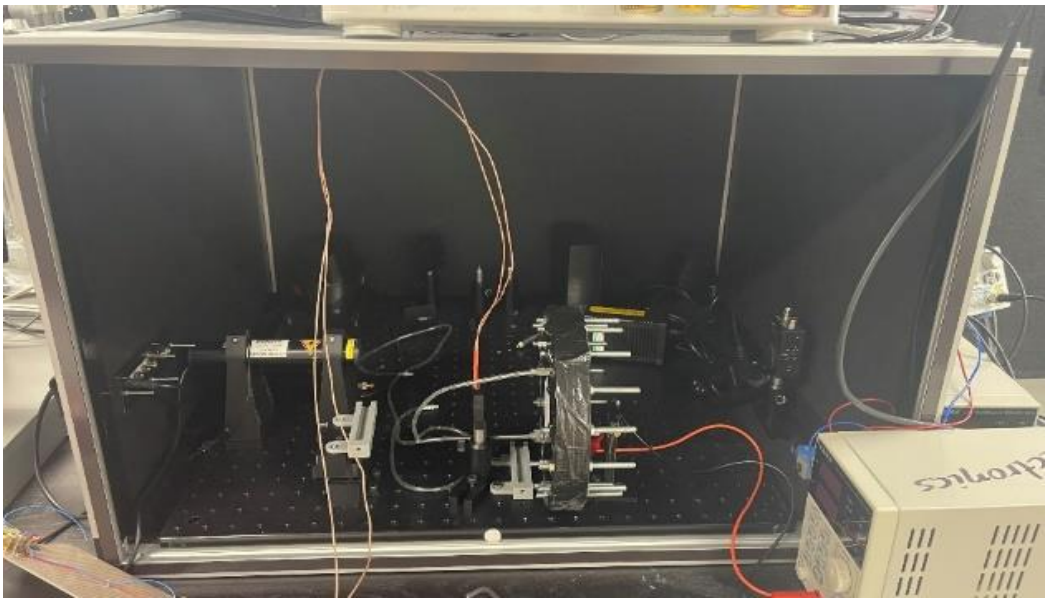

Figure 4.11. Black out box

4.11) placed on top of the optical bench in the lab with 5 cm distance between each other (Figure 4.12). 3D printed holders have been used to keep them stable and in the correct alignment with each other.

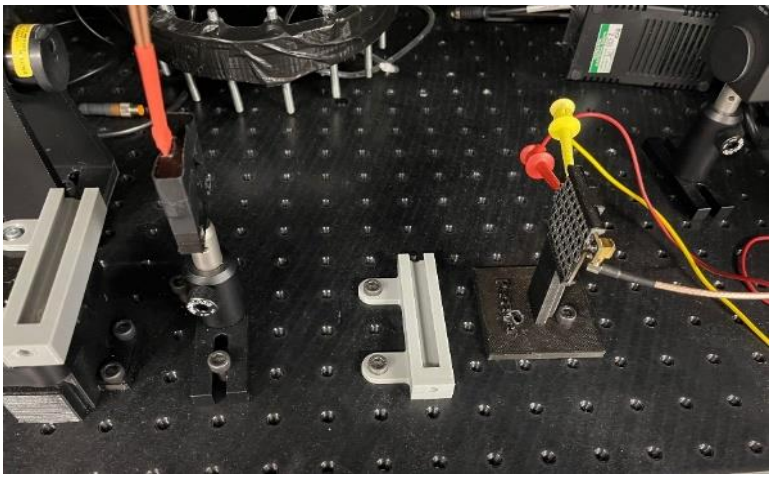

Figure 4.12. Transmitter and receiver placed on the optical bench.

The next step has been to use the tissue phantom to test the performance of my transmitter and receiver. The phantom has been placed inside the black out box on top of the optical bench and has been filled with 450 ml of milk. The transmitter has been placed in one side of the tissue phantom and my receiver on the other. Initially, the eye diagram has been plotted using the oscilloscope specifications mentioned in subchapter 4.2.4.

After the tissue phantom measurements validated that the transmission of signal through tissue can be achieved, I moved to data transmission through biological samples. More specifically, my finger, palm of hand and arm have been used. To keep my transmitter and receiver, in a stable position for the human tissue measurements, I used black tape to place them on the tissue under investigation (an example of this configuration is presented in Figure 4.13).

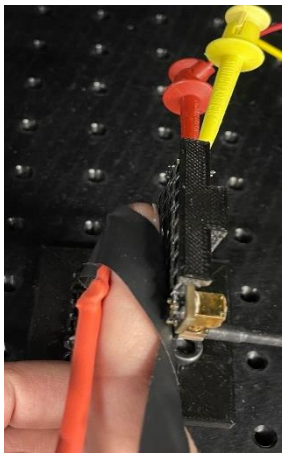

Figure 4.13. Data transmission setup through my finger

For my tests, I initially used a Raspberry pi Pico to send a square wave with data rate of 1 Mbps through the different types of tissue.

The receiver acquired the transmitted signal, and I was able to see and validate the signal through a Keysight high speeed, mixed signal Oscilloscope (InfiniiVision MSOX3104T Mixed Signal oscilloscope with bandwidth of 5 GHz and sample rate of 5 GS/s).

For the purposes of my PhD, it has been beneficial to have an indication of the quality of the transmitted signal, specifically in the high-speed data rates the capsule is working. To achieve that eye diagrams have been constructed. Eye diagrams are a common indicator of signal's quality by allowing key signal parameters to be visualised. This diagram is constructed by an oscilloscope that superimposes different segments of the data stream into one single graph. This graph has signal's amplitude on the vertical axis and time on the horizontal one. By repeatedly overlaying many different segments, the eye diagram will occur, a diagram that resembles an eye. To generate an eye diagram, the oscilloscope samples the digital signal at a high rate to accurately capture its waveform. The oscilloscope then overlays multiple waveforms, representing different bits or symbols of the transmitted signal, to form the eye pattern. The triggering edge may be positive or negative, but the displayed pulse that appears after a delay period may go either way; there is no way of knowing beforehand the value of an arbitrary bit. Therefore, when many such transitions have been overlaid, positive and negative pulses are superimposed on each other. This overlapping of wavefronts creates the characteristic shape of the eye diagram. The width of the eye provides an estimate of the uncertainty in discriminating between positive and negative pulses, highlighting the signal integrity at high data rates.

In order for the oscilloscope to display the diagram, the trigger must be set to the clock signal and not the data signal. For this purpose, the clock signal from a pattern generator or the clock signal of the data signal can be used *(ONsemiconductor, 2015), (Behera et al., 2011)*. In my experiments I used the clock signal of the data signal. More specifically, the oscilloscope has the ability to automatically recover the clock from the incoming data stream,

ensuring accurate synchronization for the eye diagram generation. The signal point used to acquire the eye diagrams has been the output of my receiver, which processes the incoming data signal. This output is illustrated in Figure 4.7, where the connector named KH-MCK-KWE-W has been employed to collect the signal. This connector facilitates a secure and efficient connection to the receiver's output, minimizing signal loss and ensuring that the integrity of the signal is maintained during all the measurements. The resulting data captured by the oscilloscope allows for precise analysis of the signal quality through the constructed eye diagrams.

Eye diagrams can reveal important information regarding the transmitted signal. They can used to identify the optimal sampling point, calculate the signal to noise ratio (SNR), provide an initial indication of the Bit Error Rate (BER), indicate the amount of jitter and estimate the time variation at zero crossing.

To our knowledge, there is no indication in the literature of what would be an acceptable BER for the transmission of endoscopic images. Indeed, the presence of random image defects would superimpose a "snow" effect on the image, without necessarily masking clinically-relevant information. We therefore decided to perform an empirical test: we have tried to transmit an image.

OVESCO (the company I cooperate with for the fulfilment of this PhD) provided me with endoscopic videos of the gastrointestinal tract. By using Visual Studio, a C^{++} code has been written (Appendix 6) in order to convert these videos to a bit stream. Then, the same code added random bit errors to the bit stream with different percentages of error each time. The final step was

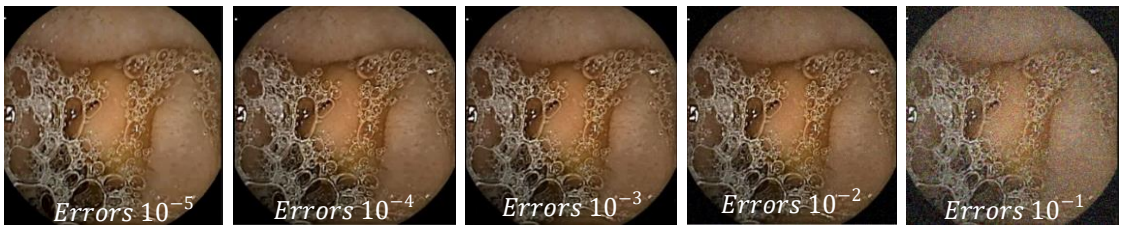

Figure 4.14. BER Simulations from 10^{-5} up to 10^{-1} errors added.

to reconstruct videos from these new bit streams with the errors. In Figure 4.14, five frames of these videos can clearly be observed. In the first one, error bits have been added with a 10^{-5} Bit Error Rate, and then in the rest, the Bit Error Rate is increased to 10^{-4}, 10^{-3}, 10^{-2} and 10^{-1}.

It can be observed that even when a lot of errors are added to the videos (10^{-1} meaning 10% of the transmitted bits is wrong), the oesophagus' frame can clearly be observed in detail. This shows clearly that the BER alone is not a good indicator of the quality of the data transmission. Indeed, the problem of describing the quality of a clinical image is still widely debated in the literature *(Menolotto, 2020)*.

For the testing of the capability to transmit an image, we therefore decided to proceed opportunistically, choosing a reference image, and qualitatively estimating if it could be transmitted through the tissue, maintaining readability. The Strathclyde logo (Figure 4.15) has been encoded into a bitstream sequence using the Raspberry pi Pico. This bitstream has then been transmitted through bit banging through tissue. The transmitted signal has not been compressed because I would not be able to do that on a real-life capsule due to the power budget available on the capsule that limits the processing able to be performed on the capsule itself. After the sequence of bits has been received by my receiver circuit, a C^{++} code (Appendix 7) has been used to recover the clock and then decode these bits into a new image. To determine that the transmission has been successful, I qualitative looked at the quality of the received image.

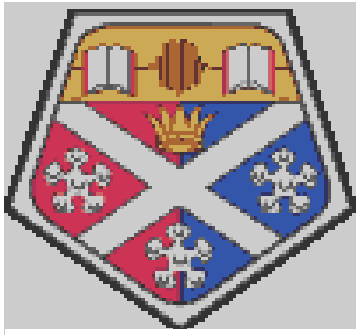

Figure 4.15. Strathclyde logo used for transmission

4.3. Results

At this stage, it is important to note that in this thesis, one set of results is presented for each different circumstance. However, the same transmission tests have been repeated at least 20 times for all the different parameters (air, tissue phantom, finger, palm of the hand and arm) with similar results. The differences were in the order of 1% and thus have not been considered on the following descriptions.

4.3.1. Raw performance

For the experiment through the air, the Raspberry pi Pico code has been used to send a square wave signal at 1 Mbps. The optical signal propagates in air and is received by the receiver. This is the lowest possible attenuation, and the transmission results are the best possible with this transmitter and receiver, giving a baseline clean signal against which to compare any other result. The result is illustrated in Figure 4.16. In yellow, the transmitted square wave is presented while with blue the received one. It can be observed that when the signal passes through air, the result is a clear square wave with identical frequency. It can be noticed that while the duty cycle of the drive signal is 50%, the duty cycle of the received signal is not. The reason for that is that in air, I have saturation of the internal stages of my circuit. Similarly, there is a phase shift between the two signals that is also due to saturation and additionally due to all the filtering I have used.

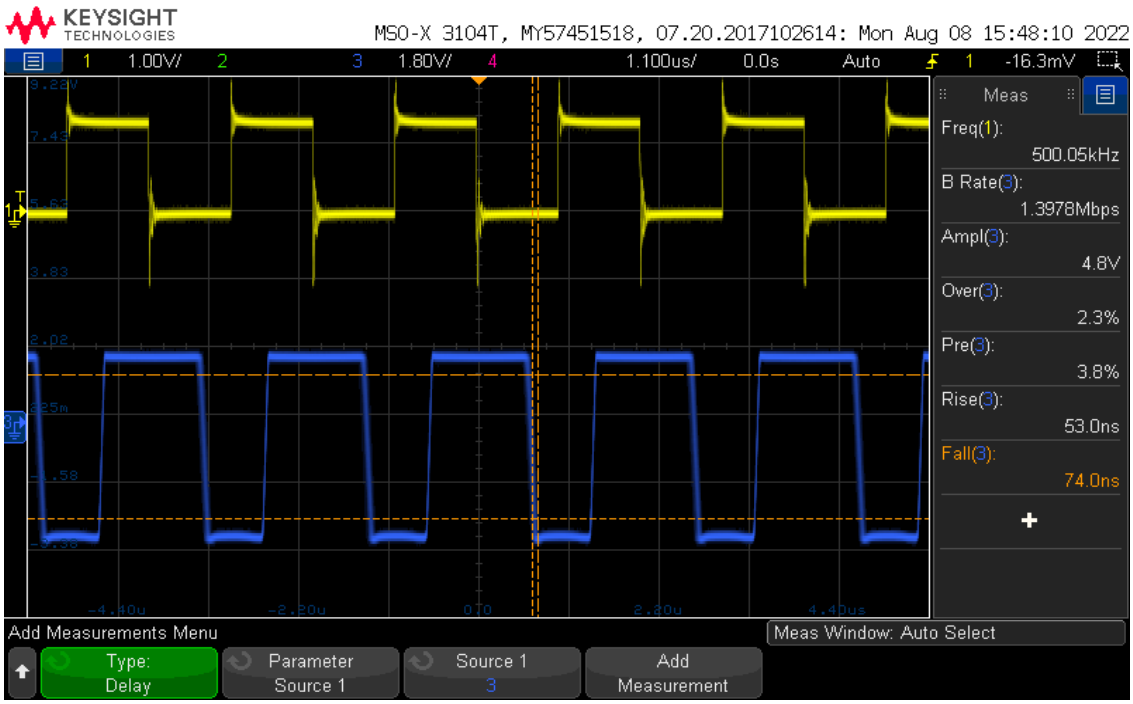

Figure 4.16. 1 Mbps square wave transmitted through air. Yellow: transmitted signal, Blue: received signal

More specifically, the components within my circuit are receiving a signal that is beyond their linear operating range and so they cannot handle it properly. As a result, these components cannot increase the output proportionally to the input, leading to a phenomenon known as clipping. This clipping distorts the signal, altering its characteristics. The main effects of this saturation are distortions on the duty cycle and a phase shift.

In tissue, I am not expecting that distortion. When the signal is transmitted through air, it encounters less attenuation compared to transmission through tissue. This means the signal remains strong and can easily exceed the linear range of the circuit components, leading to saturation. In contrast, when the signal is transmitted through tissue, it will be attenuated more significantly. This attenuation reduces the signal strength, preventing it from saturating the internal stages of the circuit. As a result, the received signal in tissue is less likely to be distorted.

To mitigate the effects of this saturation the amplitude of the drive signal can be reduced to ensure that it stays within the linear range of the circuit

components, the gain settings of the used amplifiers can be properly configured to prevent overloading, and finally the implementation of attenuators could also reduce the signal's strength before this reached the sensitive stages of the circuit.

High-density optical filters have been interposed between the transmitter and the receiver, bringing the detected signal into linear range. A twelve-station dual filter wheel has been used purchased by Thorlabs (FW2AND). This is compatible with a Ø1" (Ø25 mm) absorptive neutral density (ND) filters. Filters with Optical Density of 0.2, 0.3, 0.4, 0.6, 1.0, 2.0, 3.0, and 4.0 have been used and attached to this wheel.

In Figure 4.17 part of the data transmission stream for the image is presented. To transmit the full image, 1,000,000 points have been saved, it is not visually possible to extract information by presenting all of them. Therefore, 0.05 ms of the transmitted image is presented. The transmitted signal is illustrated with blue and the received with orange. It can be observed that both signals have a good alignment with each other.

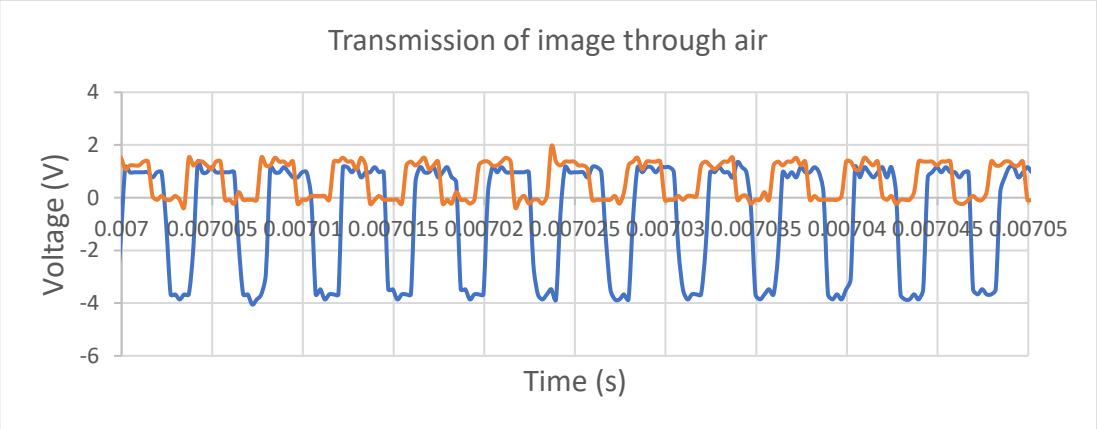

Figure 4.17. Part of transmitted bitstream image through air. Blue: transmitted bits, orange: received bits

In Figure 4.18, the transmitted through air image and the received one are presented for comparison. It can be noticed that they are identical.

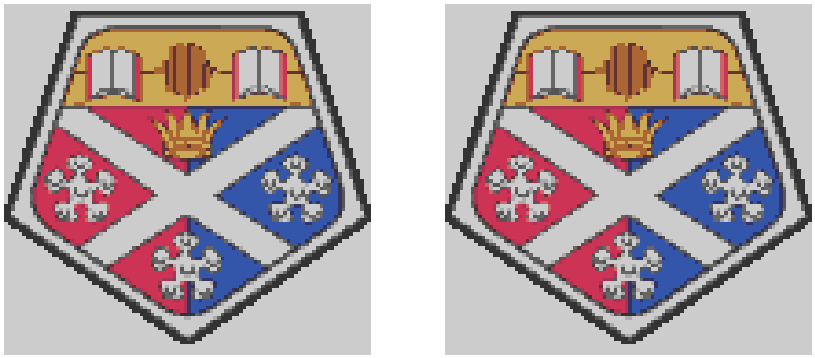

Figure 4.18. Transmission of image through air. Left: transmitted image, right: received image

After achieving the transmission of the image, I wanted to test the bandwidth limit of my system. To do that, I used the Raspberry pi Pico to send square waves with higher frequencies in order to understand up until what data rate my receiver was able to detect. In Figure 4.19 the yellow is the drive square wave signal and with blue the received one. From these graphs it can be noticed that up until 12 Mbps my signal can be clearly detected by the photodiodes.

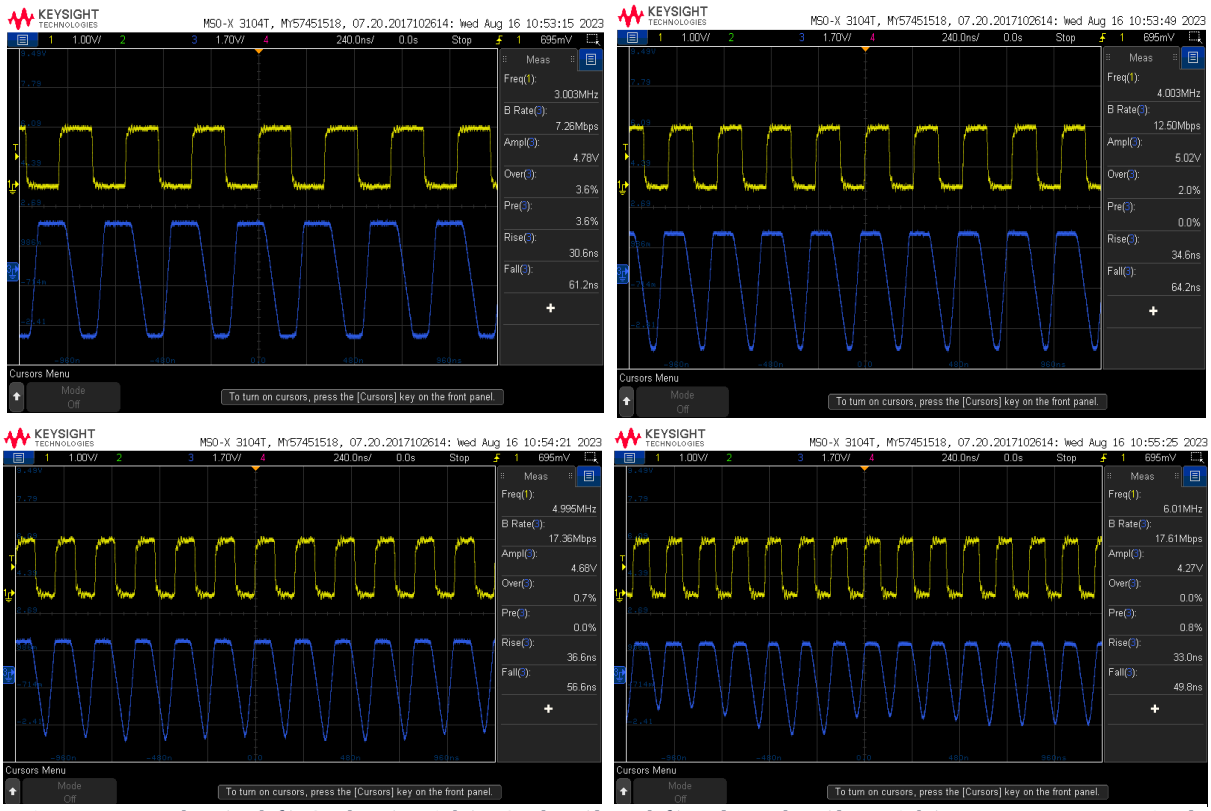

Figure 4.19. 6 Mbps (up left), 8 Mbps (up right), 10 Mbps (down left) and 12 Mbps (down right) square waves transmitted through air. Yellow: transmitted signal, Blue: received signal

4.3.2. Performance on Phantom

The next step has been to use the tissue phantom I have designed. The eye diagram created from the usage of my transmitter/receiver setup and the tissue phantom is presented in Figure 4.20.

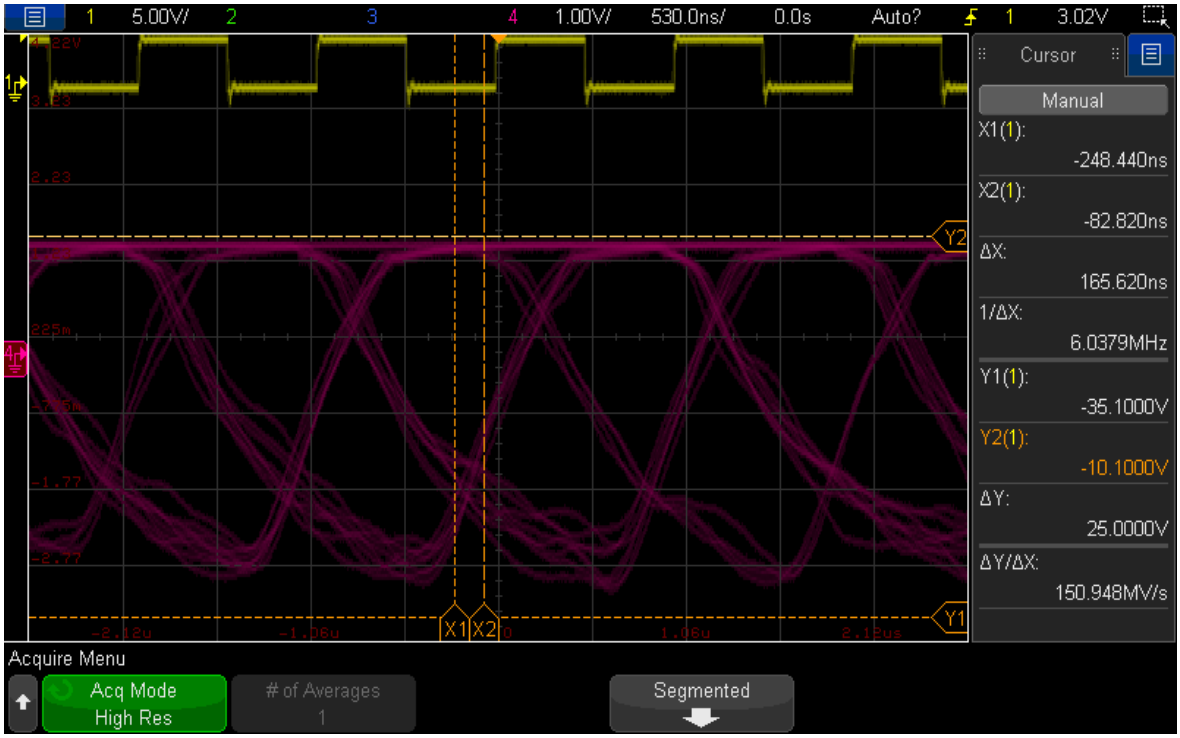

Figure 4.20. Eye Diagram through tissue phantom

Then, using the same setup, in Figure 4.21 a 1 Mbps signal transmission is presented. With yellow we can observe the clock signal, with blue the transmitted signal and with pink the received signal after being transmitted through 450 ml of milk inside the tissue phantom. The eye diagram is still open, i.e., there is a significant time region where positive and negative fronts do not overlap. While a quantitative analysis of the eye diagram is beyond the scope of this thesis, this structure of the eye diagram indicates that reconstruction of the signal with low BER is possible, as positive and negative fronts can be well differentiated.

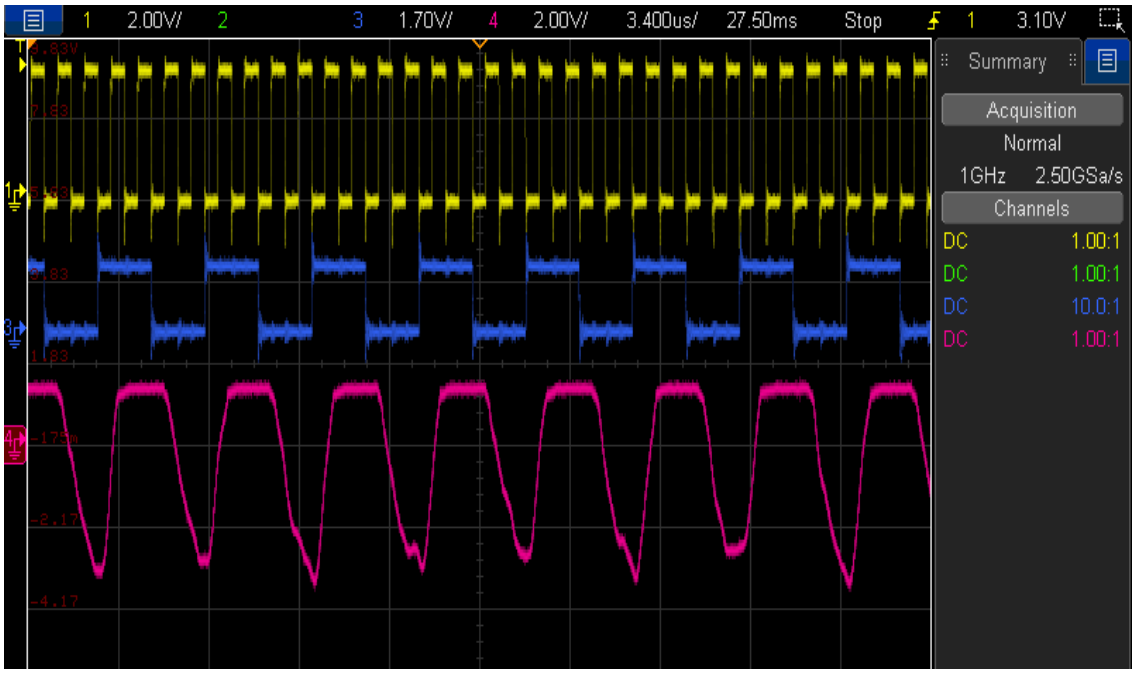

Figure 4.21. 1 Mbps signal transmission through tissue phantom. Yellow: clock, blue: transmitted signal, pink: received signal

4.3.3. Performance on Biological Samples

The next step has been to use my transmitter/receiver system and do the same measurements through biological tissues. Initially, the eye diagrams created by the transmission of signal through my finger, palm of hand and arm are presented in Figures 4.22, 4.23 and 4.24 respectively. Here, the eye is also open, indicating that data is still being transmitted with good scope for a successful decoding.

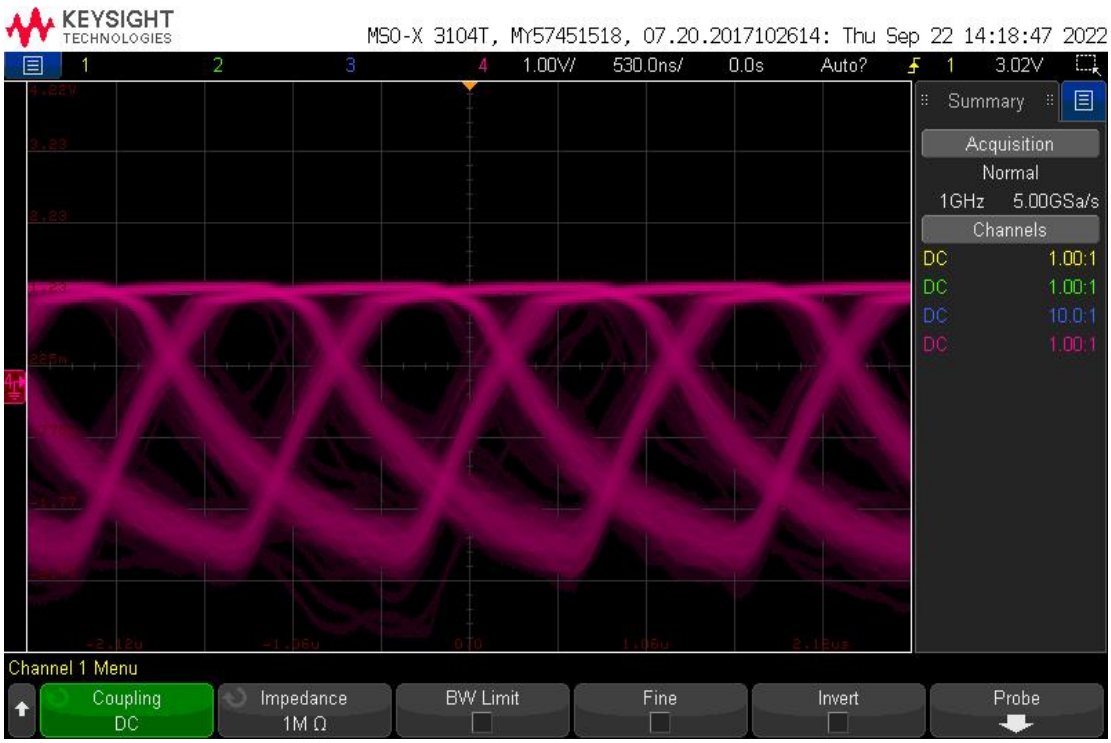

Figure 4.22. Eye Diagram through my finger

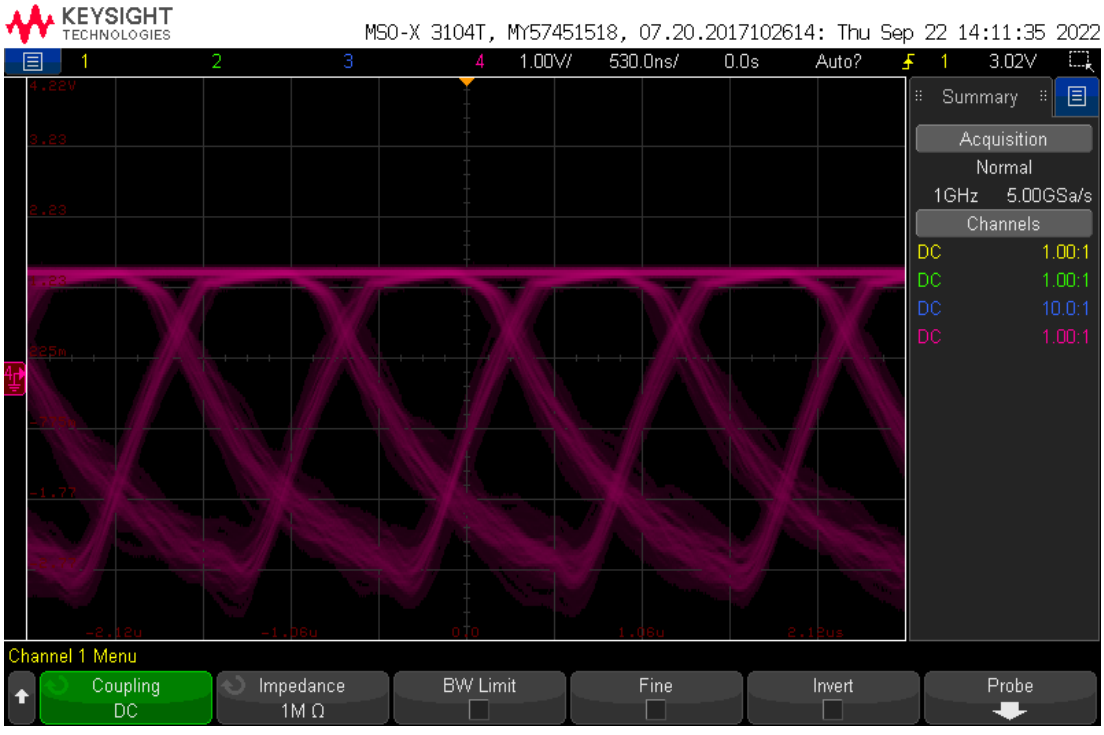

Figure 4.23. Eye Diagram through palm of my hand

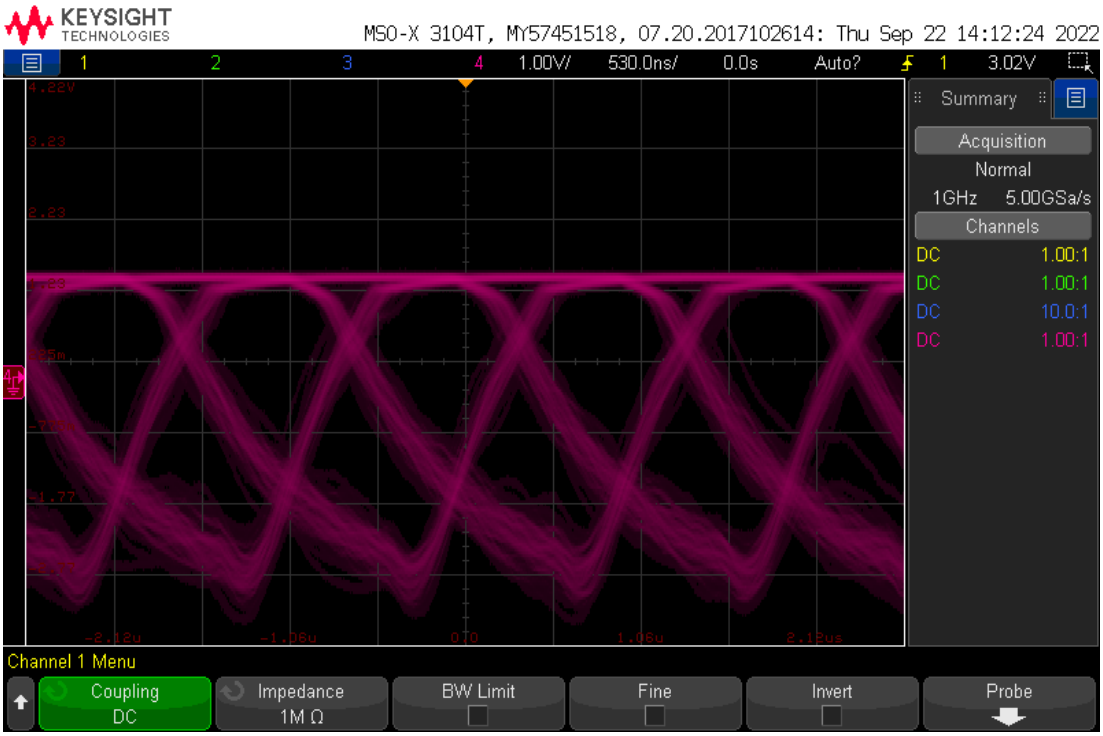

Figure 4.24. Eye Diagram through my arm

Afterwards, the transmission of a 1 Mbps square wave through my finger, palm of my hand and arm are presented in Figures 4.25, 4.26 and 4.27 respectively. Unsurprisingly, given the simulations in Chapter 3, the signal is strong and, indeed, we can see the distortions due to saturation already shown in these Figures. Clearly, an image in these conditions can be decoded.

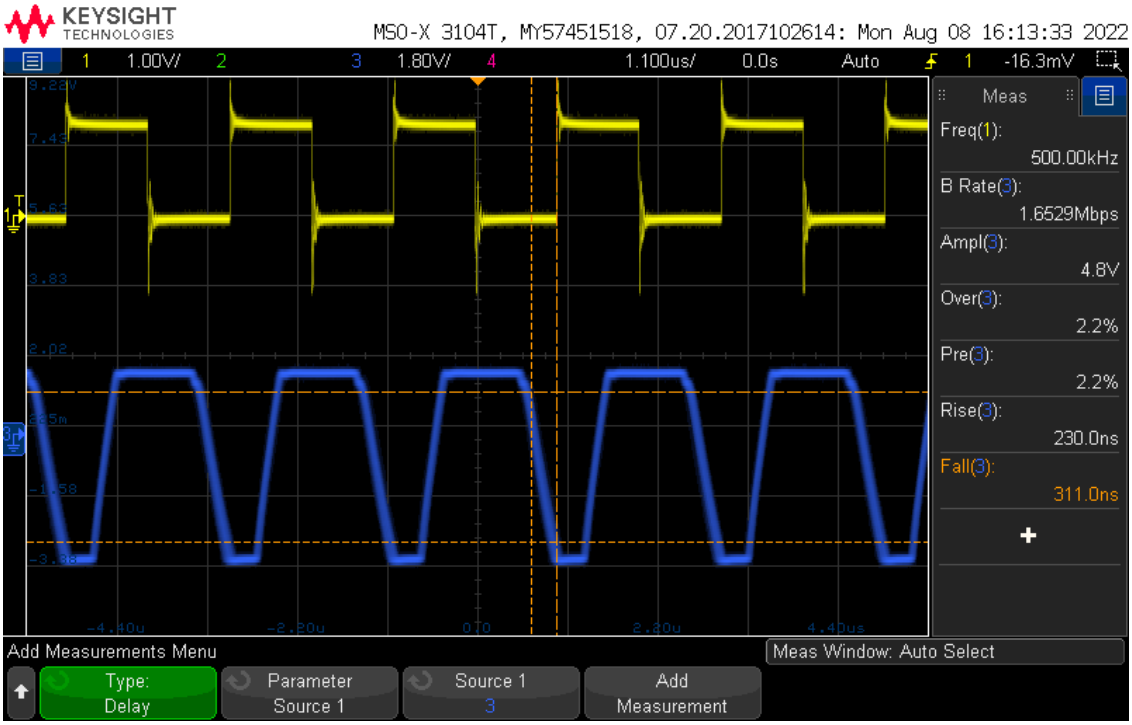

Figure 4.25. 1 Mbps signal transmitted through my finger. Yellow: transmitted signal, blue: received signal

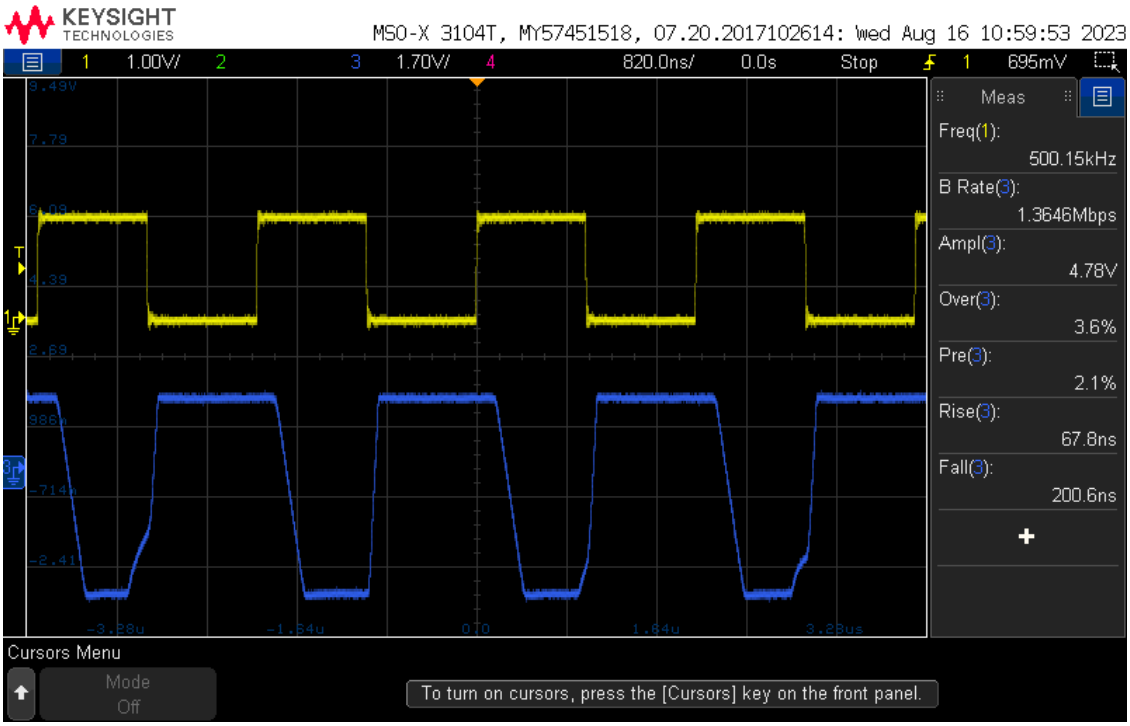

Figure 4.26. 1 Mbps signal transmitted through the palm of my hand. Yellow: transmitted signal, blue: received signal

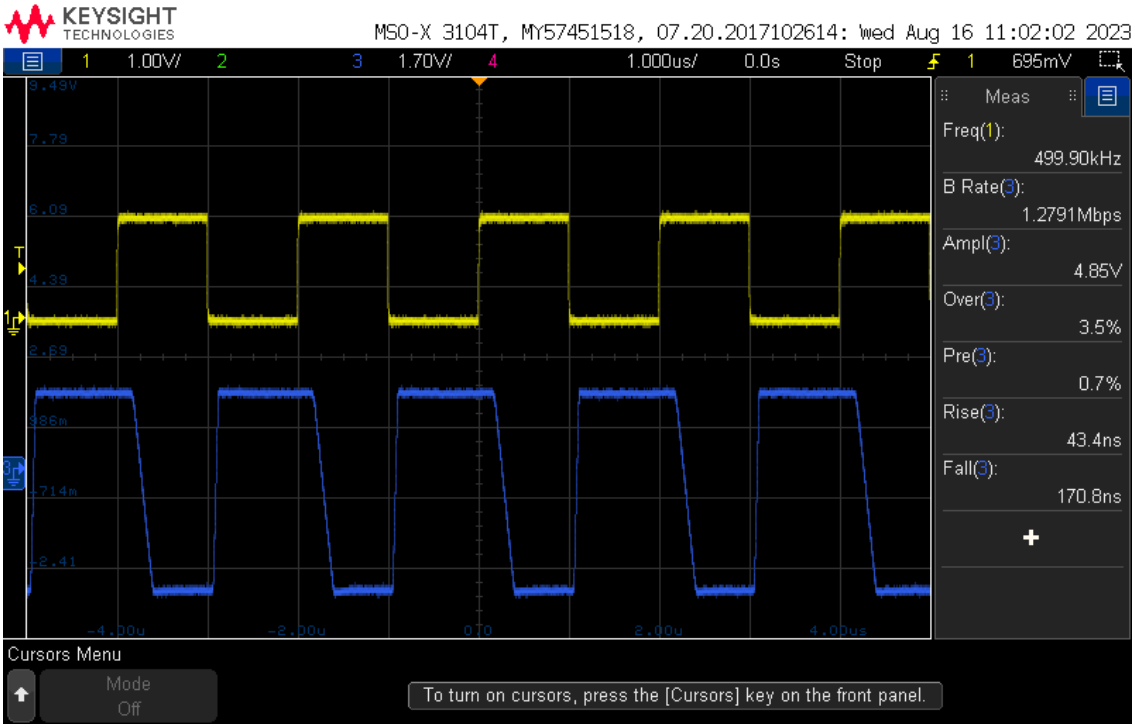

Figure 4.27. 1 Mbps signal transmitted through my arm. Yellow: transmitted signal, blue: received signal

Indeed, the transmission of the Strathclyde logo through the same biological tissues (my finger, palm of hand and arm) are presented in Figure 4.28, demonstrating that a 1 Mbps transmission of signal through biological tissue is occurring without significant impact on the image readability. Qualitative these images seem similar, and their main characteristics are clearly identifiable.

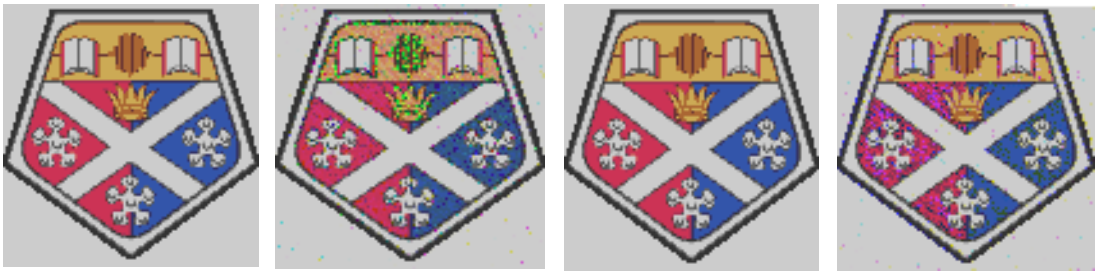

Figure 4.28. Transmission of image. a: transmitted image, b: received image through finger, c: received image through palm of hand, d: received image through arm.

.

After concluding that 1 Mbps data transmission through tissue is feasible, I did a final measurement where I used my ankle as biological tissue, which is a much thicker tissue. The resulted transmitted image is presented in Figure 4.29. It is a more distorted result, but still the main features of the image are identifiable.

Figure 4.29. Transmission of image through my ankle.

4.4. Discussion

A tethered system has been implemented, as a demonstrator of optical data transmission. The size and power follow literature requirements *(Iddan et al, 2000), (Korman et al., 2014)* albeit still tethered. The testing of the system I did follow a progression. Initially I verified that the data transmission occurs correctly in the absence of attenuation by transmitting a signal at a 1 Mbps data rate. Then, the eye diagrams through the tissue phantom and then through the different types of biological tissues have been occurred. Finally, an image has been transmitted through the different types of tissue.

In Figure 4.20, the eye diagram through the tissue phantom is presented. One intersection of the eye diagram has been highlighted from the x1, x2 cursors (the small square region at the bottom of the diagram). This intersection tells us whether the bits of our signal are well separated or whether there is an overlap between following bits. It can be noticed that this intersection is well separated from the previous similar one, they do not overlap. That means that there is a time range in which it is possible to tell apart different bits. Given the time restrictions and the qualitative investigation of this thesis, I consider this as sufficient for the purposes of this work. Indeed, showing *a posteriori* that transmission of an image has been possible, confirms this.

In eye diagram of Figure 4.22 (through finger), the eyes start to overlap with each other. It is still clear that I get well separated bits (distinct intersections), but the separation is not perfect. That means that here I will have some BER, however it is not possible to estimate an exact number from the diagrams. So,

from this eye diagram I have decided for an operational test, attempting to transmit an image and evaluate a posteriori its quality.

The results obtained from the experimental measurements, particularly the comparison of eye diagrams for different tissue types (finger, hand, and arm), show a noticeable difference in signal quality, with the eye diagram through the finger being noisier and more closed. This suggests that the transmitted signal is weaker through the finger compared to the hand or arm. This experimental observation is consistent with the results from my simulations. Specifically, the noisier eye diagram observed when transmitting through the finger, which suggests worse signal quality, aligns with the simulation predictions for muscle tissue, where the signal undergoes significant attenuation. In both the simulations and experiments, muscle tissue was found to reduce the signal strength more than fat tissue, which is reflected in the more closed eye diagram from the finger compared to the hand or arm. This supports the idea that tissue composition plays a crucial role in signal transmission, as muscle absorbs and scatters light more than fat, leading to higher signal loss.

Moreover, the simulations predicted that muscle would cause both signal attenuation and increased multipath effects, which corresponds to the experimental results where the signal through the finger (a tissue with more muscle and less fat compared to hand or arm) was noisier. On the other hand, fat tissue, which the simulations showed would allow for better signal transmission, corresponds to the clearer eye diagrams observed when the signal passed through the hand or arm. Overall, the experimental data and simulation results reinforce each other, indicating that the signal degradation observed through different tissue types is in line with theoretical expectations, and further justifies moving forward with experimental validation.

The next step has been to transmit a 1 Mbps square wave by the Raspberry pi Pico through the tissue phantom and the biological tissues. This has been the initial proof that my system could be used to clearly transmit information. The

transmission through air resulted in a clear square wave with identical frequency with the one transmitted. However, the duty cycle of the received signal has not been the same as the one of the drive signals and also there has been a time delay between the two. This is due to the saturation of the internal stages of the circuits and due to the filtering, I used in my circuits. It is noticed that when I move to transmission through the phantom and then through tissue, the two duty cycles start to approach each other in value and the time delay is decreased. That is because the internal saturation of my circuits is also decreased when I add a transmission channel between my transmitter and receiver.

The next step of my experiments has been to transmit an image through the various types of tissue under investigation. A successful image transmission has been achieved at 1 Mbps. This is at least a factor of 10 higher than the literature *(Ahmed et al., 2020)*. While a definition of quality cannot be found in the literature, it is pragmatically clear that the quality of the image in Figure 4.28 can be considered adequate. When I tried to increase the frequency of the transmitted image, there was also an increase in BER. This is due to a combined effect on the distinguishability of the individual bits, and of the fact that the added noise worsens the clock recovery. The effects on these two cannot be evaluated at this stage, as the recovery and reconstructions are performed offline, in a situation not representative of real-time usage.

4.4.1. Limitations

While the system presented in this thesis demonstrates promising capabilities, there are several important limitations to consider.

First, the extraction of the clock signal from the data is currently a relatively basic process, which, although functional for the purposes of this study, could benefit from further refinement and optimization to improve its accuracy and robustness.

Additionally, the performance of the system has been assessed primarily through qualitative evaluations, relying on subjective assessments of image quality and temporal accuracy. A more rigorous, quantitative analysis would be necessary to fully characterize the system's performance. However, there are significant challenges in achieving this. For instance, establishing repeatable test conditions, such as using a normative phantom model, would improve the consistency and reliability of performance measurements. Unfortunately, there is no established consensus in the literature on what constitutes standardized test conditions for the specific applications explored in this research. Similarly, a quantitative measurement of the Bit Error Rate (BER), which is essential for evaluating system reliability, would require extensive testing, a process that is both time-consuming and beyond the scope of this thesis. Furthermore, the lack of a normative image and an established protocol for evaluating image quality presents another limitation. The absence of standardized benchmarks makes it difficult to assess the system's performance objectively. Future research would benefit from expert input, particularly from capsule endoscopists, to define what constitutes a "high-quality" image and to develop a standardized protocol for evaluation. Without these expert-driven guidelines and reference standards, the current study relies on qualitative judgments, which limits the generalizability and precision of the findings.

CHAPTER 5

CONCLUSIONS

5.1. Brief Summary

In the first chapter of my PhD, I have given a summary of the anatomy of the gastrointestinal tract (which is the main structure under investigation in this research) and the reason that bleeding can occur in its different areas. Then, the diagnostic procedures that are traditionally followed to resolve these causes of bleeding are presented together with the most resent evolution of capsule sensors. The last part of this Chapter focused on the data transmission techniques most commonly used, their advantages and disadvantages and the reasons I chose optical communication for my work.

In the end of Chapter 1 (1.7) and in Chapter 2, I presented a review of the background literature, specifically focusing on issues related to specificity in capsule endoscopy, where many existing systems struggle to detect a broad range of biomarkers due to limited spectral sensitivity. Despite advances in optical communication and lesion detection, significant challenges remain. For example, Khan et al. *(Khan et al., 2020)* and Schostek et al. *(Schostek et al., 2020)* developed systems with limited spectral channels (two LEDs), reducing their ability to detect multiple biomarkers, such as different types of blood or food substances, which are essential for accurate diagnosis. Mohebbian et al. *(Mohebbian et al., 2021)* used a 12-channel sensor, but faced challenges with miniaturization and power efficiency, as well as the limitations of RF communication in terms of signal attenuation and data loss within biological tissues.

In addition to the challenges related to spectral channel limitations, there is also a critical need for higher data throughput to ensure that sufficient information can be transmitted for accurate and comprehensive diagnostics. As capsule endoscopy systems become increasingly advanced, the sheer volume of data generated by high-resolution imaging sensors, multi-spectral channels, and real-time processing demands more robust communication capabilities. Insufficient data throughput can lead to incomplete images or

even missed diagnoses, as some crucial details may not be transmitted in time for analysis.

Kasyanov et al. *(Kasyanov et al., 2021)* highlight the challenges of transmitting large datasets from capsule endoscopes, particularly with current wireless communication technologies, which suffer from issues such as signal degradation and bandwidth constraints. Furthermore, Wang et al. *(Wang et al., 2022)* demonstrated that improving data throughput could significantly enhance the accuracy of lesion detection, especially when using high-definition video or multi-spectral imaging. However, achieving this requires overcoming both technical and practical issues, such as ensuring stable and high-speed data transmission without compromising the power efficiency or miniaturization of the device. Therefore, there is a growing need for novel communication technologies, such as advanced RF modulation techniques, optical communication, or even hybrid solutions, to address these challenges. Addressing the issue of data throughput is crucial for the development of next-generation capsule endoscopy systems capable of delivering more detailed and reliable diagnostic information.

Building on these issues, my research addresses two major areas: expanding spectral channel detection and improving optical communication for higher data throughput. In Chapter 2, I detailed my experiments using the AS7262 sensor, where I successfully increased the number of detectable channels, expanding the system's diagnostic capabilities. I also demonstrated the feasibility of optical communication for high-bandwidth data transmission, overcoming the limitations of RF communication.

The next Chapter (Chapter 3) concentrated on the simulations I conducted to prove that the construction of the optical data link I wanted to design would make sense. Monte Carlo simulations have been chosen as this is the gold standard method for short scale simulations of propagation of light through tissue. Steady-state and time-resolved simulations have been conducted in a geometry that is representative of the positioning of the capsule inside of a

human body. This has been simulated with the capsule placed in the centre of an ellipsoidal prism with appropriate optical properties. There, the simulated receivers have been placed on the full outer surface of the ellipsoid. These simulations led to the conclusion that realistically, I could progress in the experimental phase of physically creating a transmitter and a receiver that would use optical communication to transfer information from the inside of the body to the outside world.

In Chapter 4, this transmitter and receiver have been built and tested. A tethered capsule containing a single infrared LED (850 nm) together with its driver (Raspberry pi Pico) have been used as the transmitter. A series of 40 photodiodes with 4 transimpedance amplifiers together with their amplification circuit are used as my receiver. These two subsystems have been used to successfully transmit a square wave with data rate up to 12 Mbps and then an image through a tissue phantom and through biological tissue (finger, palm of hand and arm).

5.2. Core Contributions

The three main objectives of my thesis have therefore been:

i. to design a sensing system that would be able to overcome the limited number of detection channels of existing capsule sensors.
ii. To perform a computational estimation that optical data transmission through tissue at high bandwidth can happen.
iii. To design and physically build the optical data transmission channel.

The first key challenge I addressed was the limited spectral channels available in existing capsule endoscopy systems. While systems like those developed by Khan et al. *(Khan et al., 2020)* and Schostek et al. *(Schostek et al., 2020)* use a small number of LEDs (typically two), this severely limits their ability to detect a variety of biomarkers. In contrast, I aimed to increase the number of spectral channels without exceeding the size and power budget constraints typical for capsule systems.

To achieve this, I used the commercially available AS7262 sensor, which offers six channels. By selecting a set of carefully chosen LEDs and multiplexing the sensor's channels, I increased the system's detection capacity, effectively doubling the number of channels to at least 11. This enhancement allows for the detection of a wider range of biomarkers, such as both oxygenated and deoxygenated blood, as well as various food types—all essential for accurate gastrointestinal diagnosis. To my knowledge, this is a novel contribution to the field, as no other systems to date have demonstrated such an increase in the number of detectable channels within the size and power constraints of capsule endoscopy systems.

The second objective of my thesis was to computationally estimate the feasibility of high-bandwidth optical data transmission through biological tissues. As highlighted in the literature, systems based on RF communication often struggle with bandwidth limitations and signal attenuation, particularly when transmitting through human tissue. Optical communication offers the potential to overcome these issues, but concerns about signal degradation and data loss have limited its application in capsule endoscopy.

To address these concerns, I conducted Monte Carlo simulations to model light propagation through human tissue. These simulations used a realistic model of the capsule's placement inside the body and provided a strong foundation for understanding how optical communication could be implemented successfully. The results indicated that optical data transmission is not only feasible but could also support higher data rates than current RF systems. This work provides crucial evidence that optical communication could be a viable solution for overcoming the bandwidth limitations faced by RF systems in capsule endoscopy.

The final objective of my thesis was to design, build, and test a functional optical data transmission system for capsule endoscopy. This system consists of a tethered capsule with an 850 nm LED as the transmitter, controlled by a Raspberry Pi Pico, and a receiver array of 40 photodiodes with

transimpedance amplifiers. I successfully demonstrated the transmission of a square wave at data rates of up to 12 Mbps and an image at 1 Mbps through biological tissues such as the human finger, palm, arm, and ankle.

The data rates I achieved are significantly higher than those reported in the literature. For instance, Ahmed et al. *(Ahmed et al., 2020)* demonstrated a maximum data rate of 95.5 kbps using a similar setup for optical transmission through porcine tissue. In comparison, most existing optical communication systems in capsule endoscopes report data rates in the low tens of kbps. My work shows that optical communication can achieve data rates that are an order of magnitude higher, making it a promising alternative to RF communication for real-time, high-quality imaging.

5.3. State-of-the-Art and Contribution Details

While significant advancements have been made in optical communication for capsule endoscopy, the existing literature highlights several key challenges. Systems like those of Khan et al. *(Khan et al., 2020)*, Schostek et al. *(Schostek et al., 2020)*, and Mohebbian et al. *(Mohebbian et al., 2021)* have made progress but still face limitations, particularly regarding spectral sensitivity and data transmission capabilities. For example, Khan et al. *(Khan et al., 2020)* addressed the need for automated bleeding detection in wireless capsule endoscopy (WCE) by integrating an on-chip bleeding sensor that evaluates blood's optical properties. However, their system was limited by a small number of LEDs, which restricted the ability to differentiate a wide range of biological markers. Mohebbian et al. *(Mohebbian et al., 2021)* developed a system with 12 sensors for multispectral imaging to detect gastrointestinal bleeding, but their design faced challenges in miniaturization and power efficiency due to the large number of sensors required and the use of RF communication, which suffers from limited bandwidth and signal attenuation.

To overcome these, I used the commercially available sensors existing in market when my experiments took place, and by using carefully selected LEDs

and multiplexing the source spectrum and the channel spectral sensitivity I designed a spectrometer that is working within the power budget available in capsule sensors but that could detect two times more channels compared to the used sensor alone. My research aims to increase the number of detectable spectral channels, enhancing the ability of capsule systems to discriminate between a wider range of substances, such as oxygenated and deoxygenated blood or different food types, which can serve as diagnostic markers.

To my knowledge, in literature this has not been done before. Khan et al. *(Khan et al., 2020)*, addressed the need for automated bleeding detection in wireless capsule endoscopy (WCE) by integrating an on-chip bleeding sensor. This sensor performs real-time pre-screening based on blood's optical properties. The study evaluated blood's chromatic properties using a spectrophotometer, with specific wavelength reflection ratios being crucial for distinguishing blood from non-blood samples. The lack of detailed information about the sensor design along with the limited detection channels due to the small number of LEDs, makes their work difficult to reproduce. They employed a system with just two LEDs, limiting the ability to accurately detect and differentiate between a wide range of biological markers, such as oxygenated and deoxygenated blood, or blood and various food pigments.

Mohebbian et al. *(Mohebbian et al., 2021)* have developed an innovative approach to detecting gastrointestinal bleeding using on-chip multispectral imaging sensors. Their system employs 12 sensors that capture images across different wavelengths, providing valuable spectral information beyond what conventional endoscopy offers. They created a capsule prototype with diodes operating at 450 nm, 610 nm, and 810 nm, and a PIN diode to collect reflected light. However, the large number of sensors combined in a PCB makes miniaturization challenging. Additionally, the use of RF communication in their capsule presents limitations such as limited bandwidth and data loss due to signal attenuation inside human tissue. They used the same sensor as I did (AS7262) and they conducted in vitro experiments with this sensor as a

receiver and a capsule prototype containing three LEDs (450 nm, 610 nm, 810 nm) as transmitter. This resulted in a system with limited detection bands. By utilizing a 12-channel sensor for multispectral imaging, their system's ability to detect gastrointestinal bleeding had been significantly enhanced. However, their system faced challenges in miniaturization and power efficiency due to the large number of sensors required. These limitations illustrate the ongoing need for systems with increased spectral sensitivity while maintaining a compact and power-efficient design.

In addressing these limitations, my research aims to expand the number of spectral channels detectable by a capsule system, enhancing its ability to discriminate between a wider range of substances and improve diagnostic accuracy. The key to achieving this is the emerging availability of low-power, multi-channel sensors, such as the Adafruit AS7341 10-Channel Light/Colour Sensor, which offers the ability to capture more spectral bands with minimal power consumption (Adafruit, 2023). These sensors are particularly promising for portable and battery-operated devices like capsule endoscopes, where power budget and size constraints are critical considerations.

By leveraging such sensors, it becomes possible to increase the number of detectable wavelengths without significantly increasing the size or power demand of the system. The availability of these multi-channel sensors opens up new possibilities for enhancing the specificity and accuracy of capsule endoscopy, making it possible to capture a broader range of biomarkers that are vital for diagnosing gastrointestinal diseases. For example, detecting both types of blood (oxygenated and deoxygenated) as well as different food types (which can serve as diagnostic indicators for various conditions) would require at least 6–8 spectral bands. By combining these sensors with carefully selected LED wavelengths, it is possible to design a system that can detect a wide array of biomarkers with high specificity, thus addressing the key limitations faced by current systems.

Furthermore, emerging technologies and the availability of affordable, compact multispectral sensors make this approach more feasible than ever. In contrast to older systems that struggled with power consumption and size limitations, these new sensors strike a balance between performance and efficiency, offering a promising solution for improving the specificity of capsule endoscopy systems while maintaining their portability and ease of use.

The core methodology I employed in my experiment can be adapted for use with these advanced sensors. I managed to achieve a channel count that exceeds the state of the art, yet maintaining within size and power budget constraints. This shows promise to improve specificity.

Additionally, my research builds on the potential of optical communication in capsule endoscopes. Studies such as Ahmed et al. *(Ahmed et al., 2020)* demonstrate the potential of optical transmission in capsule endoscopes. In their work, Ahmed et al. *(Ahmed et al., 2020)* used a transmitter-receiver system to optically transmit data through ex vivo porcine tissue, with pieces up to 5 cm thick. The transmitter consisted of an 810 nm LED, while the receiver was a commercially available avalanche photodiode detector. The highest data rate they achieved with this setup was 95.5 kbps, which, at the time, was one of the highest reported data rates in the literature for optical communication in capsule endoscopes. Most other studies report data rates in the low tens of kilobits per second (kbps), indicating that while optical communication holds promise, its data rate potential has not been fully realized in this application.

Although studies like these *(Ahmed et al., 2020)* have shown promise in optical transmission through biological tissue, their achieved data rates are still relatively low for more advanced applications. The bandwidth and signal loss limitations of current systems, especially when transmitting through varying tissue types, are significant. Radio Frequency (RF) communication techniques are also evolving, but they remain expensive, provide limited bandwidth, and suffer from significant signal attenuation inside biological tissue, further

limiting their performance in this context. Additionally, the literature remains divided on the feasibility of optical data transmission through tissue, with many studies raising concerns about signal degradation and low data throughput, which complicates the translation of optical communication from theory to practice in biomedical applications.

To address these limitations, my research aimed to prove that optical communication can be used effectively to transfer data through human tissue, focusing on achieving high data rates. Unlike the state-of-the-art, I focused on optimizing the system to increase the data throughput by improving the system's design, the careful choice of used wavelength and detection methods. I built upon the existing literature by focusing on maximizing the optical signal quality and utilizing advanced simulations to demonstrate the potential of optical communication in practical settings.

Monte Carlo simulations were conducted at this stage. While these techniques are traditional, they provided reassurance that the next stages of my research would be meaningful. This research demonstrates that optical communication can be effectively implemented in capsule endoscopes, even in the presence of complex biological tissue. By improving data rate potential and overcoming real-world tissue conditions, my work advances the field beyond current systems, showing that optical communication can significantly outperform RF-based systems in data throughput. These findings establish a strong foundation for the experimental phase, where the system can be tested and validated in real-world conditions.

Building on these simulations, I developed and tested an optical data transmission channel for capsule endoscopy. The optical system includes a tethered capsule with an 850 nm LED and a Raspberry Pi Pico as the source driver, paired with a receiver system comprising 40 photodiodes connected in parallel, along with transimpedance amplifiers and amplification circuits. Using this setup, I successfully demonstrated the transmission of both a square

wave at up to 12 Mbps and an image at 1 Mbps through various tissue types, including human finger, hand, arm, and ankle.

The data rates achieved in my experiments are significantly higher than those reported in the literature for optical communication through biological tissues. For instance, Ahmed et al. *(Ahmed et al., 2020)* achieved a maximum data rate of 95.5 kbps with a similar system using an 810 nm LED transmitter and avalanche photodiode receiver to transmit through ex vivo porcine tissue. This places my results in the higher range of data rates for optical communication in capsule endoscopes, which typically fall within the low tens of kbps.

It is important to note that while optical communication offers clear advantages, RF communication technologies have also evolved. For example, CapsoVision's CapsoCam Plus uses RF to transmit images at a frame rate of 20 fps, resulting in a data rate of around 20 Mbps *(Product Specifications CapsVision, 2023)*. This performance is comparable to the results achieved in my research, suggesting that RF communication could also be a viable option for high-speed data transmission in capsule endoscopy. However, with limited data comparing the two methods, further investigation is needed to determine which approach offers the best combination of reliability, performance, and cost-effectiveness. A head-to-head comparison of optical and RF communication systems would provide valuable insights into which technology holds the most promise for the future of capsule endoscopy.

5.4. Limitations

5.4.1. COVID-19 and Brexit: Impact on Animal Testing

The initial plan for my research was to develop a fully encapsulated optical capsule system and subsequently conduct animal testing in Germany, in collaboration with Ovesco Endoscopy AG, a medical device company based in Tübingen, Germany. However, due to the unforeseen circumstances caused by the COVID-19 pandemic, access to laboratories was severely restricted for

an extended period, halting experimental progress. These restrictions were further compounded by the regulatory challenges posed by Brexit, which created uncertainties in the approval and execution of overseas animal experiments.

As a result, the animal testing intended for my project could not be carried out, which led to a shift in the scope of my work. Instead of conducting in vivo experiments, I focused on implementing a tethered capsule and demonstrated its performance through human tissue (finger, hand, and arm) in a controlled laboratory setting. While this approach provided valuable insights, it was far from the original goal of testing optical data transmission through live animal tissue.

The impact of these restrictions on my experimental work has been substantial, but future work will aim to complete the animal testing phase once external constraints allow for it. As I will discuss in the following sections, the primary goal of animal testing is to explore the feasibility of optical data transmission through biological tissues and investigate the interaction of light with various tissue types in a realistic, living environment.

5.4.2 Limitations and Future Work

The lack of normative test conditions for capsule endoscopy systems remains a critical gap in the current literature. While animal testing would have been ideal to establish baseline performance data, the absence of standardized protocols for testing optical communication in biological tissues leaves a gap in the literature regarding the expected performance of such systems. Future work should aim to define a set of normative test conditions for optical capsule systems, such as specific tissue types, distances, and light wavelengths, to allow for reliable comparisons between different systems and provide a clear benchmark for performance.

One of the main contributions of my research was the expansion of the number of detectable spectral channels, which has the potential to significantly

improve the diagnostic capabilities of optical capsule systems. In Chapter 2, I describe the experiments I conducted using a commercially available 6-channel sensor (AS7262) and a set of carefully selected LEDs with specific wavelengths. I successfully increased the number of independent multispectral channels from 6 to at least 11, which enables the system to capture a broader range of biomarkers and improve diagnostic specificity.

However, increasing the number of detectable wavelengths is only the first step in a broader development chain. Subsequent research will need to demonstrate that the addition of spectral channels translates into improved specificity. This will require defining a reference set of substances for differentiation, which is not yet established in the literature. Laboratory experiments will be necessary to validate that the new setup can indeed achieve better performance in terms of both specificity and sensitivity.

One other limitation of my work has been the use of milk as a tissue phantom instead of more specialized tissue mimics. Milk served as a reasonable substitute for preliminary testing due to its similar scattering properties to biological tissues. Its uniformity, availability, and cost-effectiveness made it an ideal medium for initial experiments. However, it does not perfectly replicate the optical properties of muscle, fat, or other specific tissues found in the human body.

For more advanced studies and accurate validation of the system's performance, the use of tissue mimics that more closely match the optical properties of muscle, fat, and composite tissue layers is necessary. This limitation must be addressed in future research by utilizing phantoms with more precise tissue characteristics to ensure that the system’s performance is better aligned with real-world applications.

In the conducted Monte-Carlo simulations some further limitations remain. One of these is the lack of analytical data, poorly defined bandwidth cut-off, and uncertainty about the required Bit Error Rate (BER). Further research is needed to determine the optimal BER by simulating image degradation at

different BERs and assessing clinical quality by showing images to doctors in order to determine the level of degradation that can be tolerated. There is no known analytical relationship between BER and clinical quality of images *(Menolotto, 2020)*.

Additionally, from the time-resolved simulations I conducted, it is clear that the frequency response cannot be described with a simple cut-off frequency, necessitating further investigation into the relationship between frequency response and BER. Anatomically correct simulations must also be performed. Currently, my model is adequate for a sanity check but not for quantitative modelling *(Tuchin, 2015)*. This novel work shows that moving forward with experiments makes sense, but it also highlights the need for more detailed studies to set quantitative criteria for future research.

Future work should include using the same tethered system to conduct data transmission experiments on animal models, such as pigs, to assess how optical communication behaves in living tissues. Initially, a square wave could be used to test the transmission and confirm that the optical system can work through animal tissue. Following this, more complex data could be transmitted, such as images, to validate the system's ability to handle higher data rates and more complex signals in a biological setting.

After confirming the feasibility of optical transmission in animal models, the system could be fully encapsulated for in vivo testing. I anticipate that this will involve optimizing the system for miniaturization and power efficiency, which will require evaluating its power budget and considering the use of low-power components such as FPGAs for real-time image transmission. As the system moves toward real-world applications, it would be essential to explore the integration of multiple detectors for a more robust signal acquisition, such as placing detectors around the waist of the animal or patient in a belt configuration.

The real-time testing phase would also require further refinement of the protocols used to recover the clock signal and reconstruct transmitted images.

Currently, crude methods have been used for these purposes, but more sophisticated algorithms could enhance the image quality and improve the overall system performance.

A key future direction would be to establish normative test conditions for capsule systems that would allow for the comparison of different optical communication systems in a standardized manner. This could involve defining ideal tissue models, distances, and test conditions that are representative of human anatomy. As part of this work, the use of advanced tissue mimics—designed to replicate the optical properties of specific human tissues more accurately—would be essential.

Finally, as the research progresses toward human trials, it will be important to ensure that the system is both safe and effective for clinical use. This will involve validating the system in animal models, assessing its performance in a more realistic biological environment, and ultimately conducting human trials to confirm its practical applications.

REFERENCES

Abita, J. and Schneider, W. (2004). *Transdermal Optical Communications. Johns Hopkins Apl Technical Digest*. 25(3), pp. 261-268.

Ackermann, D., Smith, B., Wang, X., Kilgore, K. and Peckham, P. (2008). *Designing the Optical Interface of a Transcutaneous Optical Telemetry Link.* IEEE Transactions on Biomedical Engineering, 55(4), pp. 1365-1373.

Adafruit Industries. *Adafruit AS7341 10-Channel Light / Color Sensor Breakout.* Created by Bryan Siepert, Last Updated: 30-Oct-2020.

Adler, S.N. (2017). *The history of time for capsule endoscopy*. Annals of Translational Medicine. [Online], 5(9), pp. 194–194. doi:https://doi.org/10.21037/atm.2017.03.90.

Anpilogov, A., Bulychev, I. and Tolstaya, A. (2016). *Features of the Data Transmission in the Wireless Capsule Endoscopic Complex*. Procedia Computer Science, 88, pp. 312-317.

Ahmed, I., Halder, S., Bykov, A., Popov, A., Meglinski, I. V., Katz, M. (2020). *In Body Communications Exploiting Light: A Proof-of-Concept Study Using Ex Vivo Tissue Samples.* IEEE Access, 8, pp. 190378-190389, doi: 10.1109/ACCESS.2020.3031574.

Bandorski, D., Hoeltgen, R., Stunder, D. and Keuchel, M. (2014). *Capsule endoscopy in patients with cardiac pacemakers, implantable cardioverter defibrillators and left heart assist devices*. Annals of Gastroenterology, 27(1), pp. 3-8.

Baran, T., Choi, H., Flakus, M. and Sharma, A. (2019). *Photodynamic therapy of deep tissue abscess cavities: Retrospective image-based feasibility study using Monte Carlo simulation.* Medical Physics, 46(7), pp. 3259-3267.

Behera, D., Varshney, S., Srivastava, S. and Tiwari, S. (2011). *Eye Diagram Basics: Reading and applying eye diagrams.* EDN Network.

Bhanu Pillai, R. and Tolia, V. (2008). *Gastrointestinal bleeding in infants and children.* Therapy, 5(4), pp. 465-473.

Bowen, J. (2016). *Having a Push Enteroscopy A guide to the test.* NHS The Leeds Teaching Hospitals.

Bresci, G. (2009). *Occult and obscure gastrointestinal bleeding: Causes and diagnostic approach in 2009.* World Journal of Gastrointestinal Endoscopy, 1(1), pp. 3-6.

Bruaene, C. V. (2015). *Small bowel capsule endoscopy: Where are we after almost 15 years of use?.* World Journal of Gastrointestinal Endoscopy, 7(1), pp. 13-20, doi:10.4253/wjge.v7.i1.13.

Chandrasekhara, V., Elmunzer, B., Khashab, M. and Muthusamy, V. (2019). *Clinical Gastrointestinal Endoscopy.* 3rd ed. Elsevier.

Chatterjee, S., Kyriacou, P. (2019). *Monte Carlo Analysis of Optical Interactions in Reflectance and Transmittance Finger Photoplethysmography*. Sensors, 19, pp. 789-807.

Chauhan, S., Manfredi, M., Abu Dayyeh, B., Enestvedt, B., Fujii-Lau, L., Komanduri, S., Konda, V., Maple, J., Murad, F., Pannala, R., Thosani, N. and Banerjee, S. (2015). *Enteroscopy. Gastrointestinal Endoscopy.* 82(6), pp. 975-990.

Ciuti, G., Dario, P. (2011). *Capsule Endoscopy: From Current Achievements to Open Challenges.* IEEE Reviews in biomedical engineering, 4, pp. 59-72.

Cleveland Clinic medical. 2023. *Colonoscopy: Prep & procedure details.* Cleveland Clinic. [Online]. Available from:

https://my.clevelandclinic.org/health/diagnostics/4949-colonoscopy [accessed: 27 June 2023].

Cui, L., Hu, C., Zou Y., Meng, Q. (2010). *Bleeding detection in wireless capsule endoscopy images by support vector classifier.* The 2010 IEEE International Conference on Information and Automation, Harbin, pp. 1746-1751

Dai, T., Pikkula, B., Wang, L. and Anvari, B. (2004). *Comparison of human skin opto-thermal response to near-infrared and visible laser irradiations: a theoretical investigation*. Physics in Medicine and Biology, 49(21), pp. 4861-4877.

De Bruin, D., Bremmer, R., Kodach, V., de Kinkelder, R., van Marle, J., van Leeuwen, T. and Faber, D. (2010). *Optical phantoms of varying geometry based on thin building blocks with controlled optical properties.* Journal of Biomedical Optics, 15(2), pp. 025001(1-10).

Derraik, J., Rademaker, M., Cutfield, W., Pinto, T., Tregurtha, S., Faherty, A., Peart, J., Drury, P. and Hofman, P. (2014). *Effects of Age, Gender, BMI, and Anatomical Site on Skin Thickness in Children and Adults with Diabetes.* PLoS ONE, 9(1), pp. e86637(1-6).

Di Palma, P., Collin, A., De Caro, F. *et al*. The Role of Fiber Optic Sensors for Enhancing Power System Situational Awareness: A Review. *Smart Grids and Energy* **9**, 2 (2024). https://doi.org/10.1007/s40866-023-00183-0

Donati, S., ed. (1999). *Photodetectors.* Hoboken, New Jersey: Wiley-IEEE Press.

Edelman, A. (1984). *Eigenvalues and condition numbers of random matrices*. SIAM Journal on Matrix Analysis and Applications, 9(4), pp. 543–560, doi:10.1137/0609045.

Ehrlich, K., Kufcsák, A., Krstajić, N., Henderson, R. K., Thomson, R. R. and Tanner, M. G. (2017). *Fibre optic time-resolved spectroscopy using CMOS-SPAD*

arrays. Optical Fibers and Sensors for Medical Diagnostics and Treatment Applications XVII, doi:10.1117/12.2252090.

Ferreira, R.X., Xie, E., McKendry, J., Rajbhandari, S., Chun, H., Faulkner, G., Watson, S., Kelly, A., Gu, E., Penty, R., White, I., O'Brien, D., Dawson, M. (2016). *High bandwidth gan-based Micro-leds for multi-GB/S visible light communications.* IEEE Photonics Technology Letters, 28(19), pp. 2023–2026. doi:10.1109/lpt.2016.2581318.

Ferreira, S.G, Veening-Griffioen, D.H, Boon, W.P.C, Moors, E.H.M, Gispen-de Wied, C.C. (2019) *A standardised framework to identify optimal animal models for efficacy assessment in drug development. PLOS ONE 14(6): e0218014.* https://doi.org/10.1371/journal.pone.0218014.

Figueiredo, I., Kumar, S., Leal, C., Figueiredo, P. (2013). *Computer-assisted bleeding detection in wireless capsule endoscopy images.* Computer Methods in Biomechanics and Biomedical Engineering: Imaging & Visualization, 1(4), pp. 198-210.

Filippone A, Cianci R, Milano A, Valeriano S, Di Mizio V, Storto ML. (2007). *Obscure gastrointestinal bleeding and small bowel pathology: comparison between wireless capsule endoscopy and multidetector-row CT enteroclysis.* Abdom Imaging, 33(4), pp. 398-406.

Firbank, M. and Delpy, D. (1993). *A design for a stable and reproducible phantom for use in near infra-red imaging and spectroscopy.* Physics in Medicine and Biology, 38(6), pp. 847-853.

Fishkin, J. and Gratton E. (1993). *Propagation of photon-density waves in strongly scattering media containing an absorbing semi-infinite plane bounded by a straight edge.* Journal of the Optical Society of America, 10, pp. 127-140

Fox, V. (2000). *Gastrointestinal Bleeding In Infancy And Childhood.* Gastroenterology Clinics of North America, 29(1), pp. 37-66.

Friedman, L.M. *et al.* (2015) *Fundamentals of Clinical Trials*. Cham: Springer International Publishing. Available at: https://doi.org/10.1007/978-3-319-18539-2.

Giordano, S., Dilisi, J., Banwait, K., Wild, D., Infantolino, A., Miranda, L. and Conn, M. (2009). *Is There a Role for Sonde Enteroscopy in Patients with Obscure Gastrointestinal Bleeding? A Comparison with Capsule Endoscopy.* Gastroenterology Research, 2, pp. 86-90.

Goenka, M., Majumder, S. and Goenka, U. (2014). *Capsule endoscopy: Present status and future expectation.* World Journal of Gastroenterology, 20(29), pp. 10024-10037.

Gómez, S.Q., Lafuente, M.P., Abadia, M.A.-S., Conesa, J.C. (2010). *Gastrointestinal bleeding: The role of radiology.* Radiologia, 53(5). pp. 406–420.

Gralnek, I., Dumonceau, J., Kuipers, E., Lanas, A., Sanders, D., Kurien, M., Rotondano, G., Hucl, T., Dinis-Ribeiro, M., Marmo, R., Racz, I., Arezzo, A., Hoffmann, R., Lesur, G., de Franchis, R., Aabakken, L., Veitch, A., Radaelli, F., Salgueiro, P., Cardoso, R., Maia, L., Zullo, A., Cipolletta, L. and Hassan, C. (2015). *Diagnosis and management of nonvariceal upper gastrointestinal hemorrhage.* European Society of Gastrointestinal Endoscopy (ESGE) Guideline. Endoscopy, 47(10).

Hara, K., Leighton, J., Sharma, V., Heigh, R., Fleischer, D. (2005). *Imaging of small bowel disease: comparison of capsule endoscopy, standard endoscopy, barium examination, and CT.* Radiographics, 25(3), pp. 697-718.

Harris, L., Hansel, S., Rajan, E., Srivathsan, K., Rea, R., Crowell, M., Fleischer, D., Pasha, S., Gurudu, S., Heigh, R., Shiff, A., Post, J. and Leighton, J. (2013).

Capsule Endoscopy in Patients with Implantable Electromedical Devices is Safe. Gastroenterology Research and Practice, pp. 1-5.

Hartwig, W. (2008). *Fundamental Anatomy.* 1st ed. Lippincott Williams & Wilkins. pp. 157-182

Hazewinkel, Y. and Dekker, E. (2011). *Colonoscopy: basic principles and novel techniques.* Nature Reviews Gastroenterology & Hepatology, 8(10), pp. 554-564.

He, Z., P. Wang, and X. Ye. (2021). *Novel endoscopic optical diagnostic technologies in medical trial research: Recent advancements and future prospects.* BioMedical Engineering OnLine, 20(1), doi:10.1186/s12938-020-00845-5.

Hebden, J., Price, B., Gibson, A. and Royle, G. (2006). *A soft deformable tissue-equivalent phantom for diffuse optical tomography.* Physics in Medicine and Biology, 51(21), pp. 5581-5590.

Iddan, G., Meron, G., Glukhovsky, A. and Swain, P. (2000). Wireless capsule endoscopy. *Nature*, 405(6785), pp.417-418.

Jacques, S. (2009). *Chapter 5: Monte Carlo Modelling of Light Transport in Tissue (Steady State and Time of Flight).* [online] Springer. Available at: http://www-star.st-and.ac.uk/~kw25/teaching/mcrt/Ch5_Jacques_Welch2009.pdf.

Jacques, S. (2013). *Optical properties of biological tissues: a review.* Physics in Medicine and Biology, 58(11), pp. R37-R61.

Kamil N. A. I., Zakaria I. H., Ismail W. Z., Ismail I., Jamaludin J., Balakrishnan S. A., Sahrim M. (2020). *Investigating Light Propagation in full and skimmed milk based on spectroscopy and monte carlo analysis.* Journal of Engineering and Applied Science, 67(8), pp. 2265-2278

Katsafadou, M., Giardini, M. E. (2022). *Source multiplexing enhances the number of channels of a multispectral sensor.* Annu Int Conf IEEE Eng Med Biol Soc. 2022 Jul;2022:2455-2458. doi: 10.1109/EMBC48229.2022.9871570. PMID: 36086097.

Kasyanov, D., Shishkin, M., & Vasilenko, A. (2021). *Challenges in wireless data transmission for capsule endoscopy systems: A review*. Journal of Medical Devices, 15(3), pp. 45-58.

Keeton, W. T., Hightower, N. C., Sircus, W., and Dworken, H. J. (2023). *Human digestive system.* Encyclopedia Britannica. [Online]. Available from: https://www.britannica.com/science/human-digestive-system. [accessed 28 June 2023].

Keuchel, M., Hagenmüller, F. and Tajiri, H. (2015). *Video Capsule Endoscopy.* Berlin, Heidelberg: Springer Berlin Heidelberg.

Khiao In, M., Richardson, K., Loewa, A., Hedtrich, S., Kaessmeyer, S. and Plendl, J. (2019). *Histological and functional comparisons of four anatomical regions of porcine skin with human abdominal skin.* Anatomia, Histologia, Embryologia, 48(3), pp. 207-217.

Knuth, D.E. (1981). *Seminumerical Algorithms.* The Art of Computer Programming. 2nd ed., 2 (Reading, MA: Addison-Wesley), paragraphs 3.2–3.3

Korman, L., Sahlstrand-Johnson, P. and Husberg, P. (2014). Power and size optimization for capsule endoscopes. *Journal of Micromechanics and Microengineering*, 24(12), p.125003.

Kim, J., Lim, H., Lee, S. and Kim, Y. (2012). *Thickness of Rectus Abdominis Muscle and Abdominal Subcutaneous Fat Tissue in Adult Women: Correlation with Age, Pregnancy, Laparotomy, and Body Mass Index.* Archives of Plastic Surgery, 39(05), pp. 528-533.

Kim, J. (2020). *Management and Prevention of Upper GI Bleeding.* Semanticscholar.org. [Online]. Available from: https://www.semanticscholar.org/paper/Management-and-Prevention-of-Upper-GI-Bleeding-Kim/b2cc56c38bf0e51f6350d067e9400343a40da167 [accessed 12 June 2020].

Kohli, D.R. and Baillie, J. (2019). *How endoscopes work.* Clinical Gastrointestinal Endoscopy [Preprint]. doi:10.1016/b978-0-323-41509-5.00003-7.

Koprowski, R. (2015). *Overview of technical solutions and assessment of clinical usefulness of capsule endoscopy.* BioMedical Engineering OnLine, 14(1).

Labsphere (2022). *LabSphere Resources - articles, tech guides, & more.* [Online]. Available from: https://www.labsphere.com/resource/?r_type%5B%5D=146. [accessed 2 May 2022]

Landi, B., Tkoub, M., Gaudric, M., Guimbaud, R., Cervoni, J., Chaussade, S., Couturier, D., Barbier, J. and Cellier, C. (1998). *Diagnostic yield of push-type enteroscopy in relation to indication.* Gut, 42(3), pp. 421-425.

Lee, Y., Yoon, G. (2012). *Improvement of Blood Detection Accuracy using Image Processing Techniques suitable for Capsule Endoscopy.* International Journal of Biomedical and Biological Engineering, 6(5), pp. 168-171

Lemaillet, P., Bouchard, J-P., Hwang, J., Aller, D. (2015). *Double-integrating-sphere system at the National Institute of Standards and Technology in support of measurement standards for the determination of optical properties of tissue-mimicking phantoms.* Journal of Biomedical Optics, 20(12), pp. 1-8

Leonhardt, H., Kahle, W. and Platzer, W. (1986). *Color Atlas and Textbook Of Human Anatomy.* Stuggart: Georg Thieme Verlag. 3rd ed., 2, pp. 174-249

Li, Z., Carter, D., Eliakim, R., Zou, W., Wu, H., Liao, Z., Gong Z. (2014). *The current Main Types of Capsule Endoscopy.* Handbook of Capsule Endoscopy, pp. 5-45

Lindon, J., Tranter, G. and Holmes, J. (2000). *Encyclopedia Of Spectroscopy And Spectrometry Part 1 (A-L).*

Lualdi, M., Colombo, A., Farina, B., Tomatis, S. and Marchesini, R. (2001). *A phantom with tissue-like optical properties in the visible and near infrared for use in photomedicine.* Lasers in Surgery and Medicine, 28(3), pp. 237-243.

Lundström, R., Dahlqvist, H., Hagberg, M. and Nilsson, T. (2018). *Vibrotactile and thermal perception and its relation to finger skin thickness.* Clinical Neurophysiology Practice, 3, pp. 33-39.

Mackiewicz, M., Fisher, M., Jamieson, C. (2008). *Bleeding detection in Wireless Capsule Endoscopy using adaptive colour histogram model and Support Vector Classification.* Proceeding of SPIE – The International Society for Optical Engineering

Mader, S. and Longenbaker, S. (2004). *Understanding Human Anatomy & Physiology.* New York: McGraw-Hill Higher Education. 5th ed., pp. 295-322

Mar Athanasius College. (2020). *Colorimeter, I Semester Zoology – Tools and Techniques.* Available at: http://macollege.in/UserFiles/UG%20Syllabus%20-MAC%20Botany.pdf. [Accessed 28 Jun. 2020].

Martini, F., Nath, J., Bartholomew, E. and Ober, W. (2015). *Fundamentals of Anatomy & Physiology.* Pearson. 10th ed., pp. 906-960

Matas, J., Asteinza, M., Loscos, J., Fernández, S., Ramírez-Armengol, J., Díaz-Rubio, M. (2006). *Diagnostic yield and safety of capsule endoscopy.* Revista Espanola de Enfermedades Digestivas, 98(9), pp. 666-673

McNaught, A. D., Wilkinson, A., (1997). *Compendium of Chemical Technology*. Blackwell Scientific Publication. 2nd ed.

Mendoza-Trejo, S., Ruiz-Martinez, V. and Domínguez-Herrera, J. (2018). *Evaluation of Gastric Diseases Using Segmentation RGB Interface in Video Endoscopy Images*. International Journal of Advanced Engineering, Management and Science, 4(6), pp. 474-478.

Menolotto, M. (2020). *Artifact removal in digital retinal images*. [online] STAX. Available at: https://stax.strath.ac.uk/concern/theses/6108vb275 [Accessed 1 Sep. 2024].

Miah, S., Khan, A., Icheln, C., Heneda, K. (2018). *Antenna Systems for Wireless Capsule Endoscope: Design, Analysis and Experimental Validation*. IEEE Transactions on antennas and propagation.

Millar, I., Beale, M., Donoghue, B., Lindstrom, K., Williams, S. (1998). *The IrDA Standards for High-Speed Infrared Communications*. The Hewlett-Packard Journal. Article 2.

Moglia, A., Menciassi, A., Dario, P. et al. (2009). *Capsule endoscopy: progress update and challenges ahead*. Nature Reviews Gastroenterology & Hepatology, 6(6), pp.353–361. Available at: https://doi.org/10.1038/nrgastro.2009.69

Mohebbian, M. R., Sohag, M. H., Vedaei, S. S., and Wahid, K. A. (2021). *Automated detection of bleeding in capsule endoscopy using on-chip multispectral imaging sensors*. IEEE Sensors Journal, 21(13), pp. 14121–14130, doi:10.1109/jsen.2020.3034831.

Moon, Y., Lee, J., Park, H., Cho, J. and Choi, H. (2014). *Implemented a wireless communication system for VGA capsule endoscope*. Bio-Medical Materials and Engineering, 24(6), pp.3539-3547.

Morimoto, A., Suga, T., Tottori, N., Wachi, M., Misaki, J., Tsuchikane, R. and Isaka, T. (2017). *Association between hand muscle thickness and whole-body skeletal muscle mass in healthy adults: a pilot study.* Journal of Physical Therapy Science, 29(9), pp.1644-1648.

NHS. (2020). *Angiography.* [Online]. Available from: https://www.nhs.uk/conditions/angiography/ [Accessed 22 June 2020].

Onsemi.com. (2015). *Understanding Data Eye Diagram Methodology For Analyzing High Speed Digital Signals.* [Online]. Available from: https://www.onsemi.com/pub/Collateral/AND9075-D.PDF. [accessed 29 September 2020].

Palmer, K. (2002). *Non-variceal upper gastrointestinal haemorrhage: guidelines.* Gut, 51, pp. iv1-iv6.

Pan, G., Wang, L. (2012). *Swallowable Wireless Capsule Endoscopy: Progress and Technical Challenges.* Gastroenterology Research and Practice.

Pandey, A. (2020). *Enteroscopy: Procedure, purpose, results, cost, price.* myUpchar. [Online]. Available from: https://www.myupchar.com/en/test/enteroscopy. [accessed: 27 June 2023].

Park, M., Kang, T., Lim, I., Oh, K., Kim, S., Lee, J. and Park, H. (2018). *Low-Power, High Data-Rate Digital Capsule Endoscopy Using Human Body.* Applied Sciences, 8(9), pp. 1414(1-17).

Peura, D., and NIDDK scientists. (2020). *Gastrointestinal (GI) Bleeding.* NIDDK. National Institute of Diabetes and Digestive and Kidney Diseases. [Online[. Available from: https://www.niddk.nih.gov/health-information/digestive-diseases/gastrointestinal-bleeding [accessed 12 June 2020].

Pogue, B. and Patterson, M. (2006). *Review of tissue simulating phantoms for optical spectroscopy, imaging and dosimetry*. Journal of Biomedical Optics, 11(4), pp. 041102(1-16).

Prahl, S. (2017). *Monte Carlo Light Scattering Programs*. Scott Prahl's website [Online]. Available from: https://omlc.org/software/mc/ [accessed 27 June 2019]

Product specifications. (2023). *Capsovision*. [Online]. Available from: https://capsovision.com/physicians/product-specifications/#:~:text=The%20CapsoCam%20Plus%20small%20bowel,(5%20FPS%20per%20camera). [accessed: 17 August 2023)].

Ritter, R., Handwerker, J., Liu, T. and Ortmanns, M. (2014). *Telemetry for Implantable Medical Devices: Part 1 - Media Properties and Standards*. IEEE Solid-State Circuits Magazine, 6(2), pp. 47-51.

Rockey, D. (1999). *Occult Gastrointestinal Bleeding*. New England Journal of Medicine, 341(1), pp. 38-46.

Rodger, A., Wormell, P. (2013). *Absorption Spectroscopy: Practical Aspects*. In: Roberts, G.C.K. (eds) Encyclopedia of Biophysics. Springer, Berlin, Heidelberg. https://doi.org/10.1007/978-3-642-16712-6_779

Rohatgi, A. (2023). *Webplotdigitizer - copyright 2010-2022 Ankit Rohatgi.* [Online]. Available from: https://apps.automeris.io/wpd/ [accessed 18 January 2023]

Rossini, F. and Gay, G. (1998). *Atlas Of Enteroscopy.* Milan: Springer.

Rouse, M. (2011). *Optical Communication. Techopedia.* [Online]. Available from: https://www.techopedia.com/definition/24942/optical-communication [accessed 22 February 2021]

Saygili, F., Saygili, S. and Oztas, E. (2015). *Examining the whole bowel, double balloon enteroscopy: Indications, diagnostic yield and complications.* World Journal of Gastrointestinal Endoscopy, 7(3), pp. 247-252.

Schostek, S., Schurr, M.O. (2013). *European research on wireless endoscopy--the VECTOR project.* Stud Health Technol Inform. 2013;189:193-9. PMID: 23739381.

Schostek, S., Zimmermann, M., Keller, J., Fode, M., Melbert, M., Schurr, M. O., Gottwald, T. and Prosst, R. L. (2016). *Telemetric real-time sensor for the detection of acute upper gastrointestinal bleeding:* Biosensors and Bioelectronics, 78, pp. 524–529, doi:10.1016/j.bios.2015.11.073.

Seddik, A. and Benkirane, H. (2017). *Upper Gastrointestinal Bleeding (UGB): Causes and Treatment.* Journal of Hepatology and Gastrointestinal disorders, 03(03).

Seeley, R., Stephens, T. and Tate, P. (2001). *Essentials of Anatomy & Physiology.* New York: McGraw-Hill Education. 4th ed., pp. 430-463

Sekuboyina, A., Devarakonda, S., Seelamantula, C. (2017). *A convolutional neural network approach for abnormality detection in Wireless Capsule Endoscopy.* IEEE 14th International Symposium on Biomedical Imaging (ISBI 2017), Melbourne, VIC, pp. 1057-1060

Sherwood Scientific Ltd. (2020). *A Guide to Colorimetry.* Datasheet

Singeap, A.M., Stanciu, C., Trifan, A. (2016). *Capsule Endoscopy: The road ahead.* World Journal of Gastroenterology, 22(1), pp. 369-378. doi:10.3748/wjg.v22.i1.369.

Stevenson, M. (2009). *Human Skin And Tissue Phantoms In Optical Software: Engineering Design And Future Medical Applications.* Bachelor's degree with Honours in Molecular and Cellular Biology. University of Arizona. [Online]

Hdl.handle.net. Available from: http://hdl.handle.net/10150/146219 [accessed 9 September 2020].

Suman, S., Hussin, F., Malik, A., Pogorelov, K., Riegler, M., Ho, S., Hilmi, I., Goh, K. (2017). *Detection and Classification of Bleeding Region in WCE Images using Color Feature.* CBMI 2017, Florence, Italy.

Sunada, K. and Yamamoto, H. (2008). *Double balloon enteroscopy: Techniques.* Techniques in Gastrointestinal Endoscopy. 10(2), pp. 46–53. doi:10.1016/j.tgie.2008.01.002.

Sung, J., Kuipers, E. and Barkun, A. (2012). *Gastrointestinal Bleeding*. Wiley-Blackwell.

Sushma, B. and Aparna, P. (2022). *Recent developments in wireless capsule endoscopy imaging: compression and summarization techniques.* Computers in Biology and Medicine, 149.

Swinehart, D. (1962). *The Beer-Lambert Law.* Journal of Chemical Education, 39(7), pp. 333-335.

Taylor-Williams M, Spicer G, Bale G, Bohndiek SE. Noninvasive hemoglobin sensing and imaging: optical tools for disease diagnosis. J Biomed Opt. 2022 Aug;27(8):080901. doi: 10.1117/1.JBO.27.8.080901

Toennies, T., Tortora, G., Simi, M., Valdastri, P., Webster III, R. (2009). *Swallowable medical devices for diagnosis and surgery: the state of the art.* Mechanical Engineering Science, 224, pp. 1397-1414.

Tuchin, V. (2015). *Tissue Optics.* Bellingham: SPIE Press.

Usman, M., Satrya, G., Usman, M., Shin, S. (2016). *Detection of small colon bleeding in wireless capsule endoscopy videos.* Computerized Medical Imaging and Graphics, 54, pp. 16-26.

Van de Bruaene, C., De Looze, D., Hindryckx, P. (2015). *Small bowel capsule endoscopy: Where are we after almost 15 years of use?*. World Journal of Gastrointestinal Endoscopy, 7(1), pp. 13-36.

Van Leerdam, M. (2008). *Epidemiology of acute upper gastrointestinal bleeding.* Best Practice & Research Clinical Gastroenterology, 22(2). pp. 209-224.

Van Turenhout, S., Jacobs, M., van Weyenberg, S., Herdes, E., Stam, F., Mulder, C., Bouma, G. (2010). *Diagnostic yield of capsule endoscopy in a tertiary hospital in patients with obscure gastrointestinal bleeding.* Journal of Gastrointestinal and Liver Diseases, 19(2), pp. 141-145

Varotsos, G., Nistazakis, H., Aidinis, K., Jaber, F. and Rahman, K. (2019). *Transdermal Optical Wireless Links with Multiple Receivers in the Presence of Skin-Induced Attenuation and Pointing Errors.* Computation, 7(33), pp. 1-19.

Vernava, A., Moore, B., Longo, W., Johnson, F. (1997). *Lower gastrointestinal bleeding.* Diseases of the Colon & Rectum, 40, pp. 846–858

Wagnières, G., Cheng, S., Zellweger, M., Utke, N., Braichotte, D., Ballini, J. and Bergh, H. (1997). *An optical phantom with tissue-like properties in the visible for use in PDT and fluorescence spectroscopy.* Physics in Medicine and Biology, 42(7), pp. 1415-1426.

Wang, L., Jacques, S. and Zheng, L. (1995). *MCML – Monte Carlo modelling of light transport in multi-layered tissues.* Computer Methods and Programs in Biomedicine, 47(2), pp. 131-146. [Online]. Available from: https://omlc.org/classroom/ece532/class3/gdefinition.html#:~:text=The%20anistoropy%2C%20g%20%5Bdimensionless%5D,shown%20in%20the%20figure%20below.

Wang, J., Wang, Z., Leach, M., Lee, S., Lim, E. and Huang, Y. (2016). *RF characteristics of wireless capsule endoscopy in human body.* Journal of Central South University, 23(5), pp. 1198-1207.

Wang, Y., Li, J., Zhang, Z., & Liu, X. (2022). *Improving data throughput for high-definition and multi-spectral capsule endoscopy: The role of advanced communication technologies*. Journal of Biomedical Engineering, 39(2), pp. 122-135.

Ward's Data Hub. (2012). *Beer-Lambert Law: Measuring Percent Transmittance of Solutions at Different Concentrations (Teacher's Guide).* WARD's Science, 11/12

Waugh, A. and Grant, A. (2001). *Ross & Wilson Anatomy and Physiology.* 9th ed. pp. 281-328

Waye, J., Rex, D. and Williams, C. (2003). *Colonoscopy.* Somerset: Blackwell.

Whelan, C., Chen, C., Kaboli, P., Siddique, J., Prochaska, M. and Meltzer, D. (2010). *Upper versus lower gastrointestinal bleeding: A direct comparison of clinical presentation, outcomes, and resource utilization.* Journal of Hospital Medicine, 5(3), pp. 141-147.

Wilkins, T., Khan, N., Nabh, A., Schade, R. (2012). *Diagnosis and management of upper gastrointestinal bleeding.* Am Fam Physician, 85(5), pp. 469-476

Wormell, P., Rodger, A. (2013). *Absorbance Spectroscopy: Overview*. Roberts, G.C.K. (eds) Encyclopedia of Biophysics. Springer, Berlin, Heidelberg. https://doi.org/10.1007/978-3-642-16712-6_784

Zhang, F. and Li, J. (2016). *A note on double Henyey–Greenstein phase function*. Journal of Quantitative Spectroscopy and Radiative Transfer, 184, pp. 40–43. doi:https://doi.org/10.1016/j.jqsrt.2016.06.016.

Zuckerman, G. R., and Prakash, C. (1998). *Acute lower intestinal bleedingpart I: Clinical presentation and diagnosis.* Gastrointestinal Endoscopy, 48(6), pp. 606–616, doi:10.1016/s0016-5107(98)70043-4.

APPENDICES

Appendix 1 – Code to drive the AS7262 sensor

```
# SPDX-FileCopyrightText: 2020 ladyada for Adafruit Industries
# SPDX-License-Identifier: MIT

import time
import board
import busio
import storage

# for I2C use:
from adafruit_as726x import AS726x_I2C

# for UART use:
# from adafruit_as726x import AS726x_UART

# maximum value for sensor reading
max_val = 16000

# max number of characters in each graph
max_graph = 80

def graph_map(x):
    return min(int(x * max_graph / max_val), max_graph)

# for I2C use:
i2c = busio.I2C(board.GP9, board.GP8) #uses GP9: SCL & GP8: SDA
sensor = AS726x_I2C(i2c)

sensor.conversion_mode = sensor.MODE_2

while True:
    # Wait for data to be ready
    while not sensor.data_ready:
        time.sleep(0.01)

    # plot plot the data
    print("\n")
   # print("V: " + graph_map(sensor.violet) * "=")
   # print("B: " + graph_map(sensor.blue) * "=")
   # print("G: " + graph_map(sensor.green) * "=")
   # print("Y: " + graph_map(sensor.yellow) * "=")
   # print("O: " + graph_map(sensor.orange) * "=")
   # print("R: " + graph_map(sensor.red) * "=")


# def get_calibrated_values(self, timeout=10):
```

```
#         """Return an instance of CalibratedValues containing
the 6 spectral bands."""
#         t_start = time.time()
#         while self._as7262.get('CONTROL').data_ready == 0 and
(time.time() - t_start) <= timeout:
#             pass
#         data = self._as7262.get('CALIBRATED_DATA')
#       return CalibratedValues(data.r, data.o, data.y, data.g,
data.b, data.v)

#CalibratedValues(data.r,  data.o,  data.y,  data.g,  data.b,
data.v)

    print (sensor.violet)
    print (sensor.blue)
    print (sensor.green)
    print (sensor.yellow)
    print (sensor.orange)
    print (sensor.red)

   # time.sleep(1)
```

Appendix 2 – Code to drive the LEDs

```
void setup() {
  // put your setup code here, to run once:
  // initialize digital pins as outputs.

  pinMode(22, OUTPUT);
  pinMode(24, OUTPUT);
  pinMode(26, OUTPUT);
  pinMode(28, OUTPUT);
  pinMode(30, OUTPUT);
  pinMode(32, OUTPUT);
  pinMode(34, OUTPUT);
  pinMode(36, OUTPUT);
}

void loop() {
  // put your main code here, to run repeatedly:
  digitalWrite(22, HIGH); //red 8 616nm
  digitalWrite(24, HIGH); //IR 7 890nm
  digitalWrite(26, HIGH); //IR 6 830nm
  digitalWrite(28, HIGH); //white 5
  digitalWrite(30, HIGH); //amber 4 600nm
  digitalWrite(32, HIGH); //green 3 525nm
  digitalWrite(34, HIGH); //blue-green 2 498nm
  digitalWrite(36, HIGH); //blue 1 465nm
  delay(2000);

// each LED
  digitalWrite(36, LOW);    // turn the LED on (HIGH is the
voltage level)
  delay(1000);
  digitalWrite(36, HIGH);    // turn the LED on (HIGH is the
voltage level)
  delay(500);
  digitalWrite(34, LOW);    // turn the LED on (HIGH is the
voltage level)
  delay(1000);
  digitalWrite(34, HIGH);    // turn the LED on (HIGH is the
voltage level)
  delay(500);
  digitalWrite(32, LOW);    // turn the LED on (HIGH is the
voltage level)
  delay(1000);
  digitalWrite(32, HIGH);    // turn the LED on (HIGH is the
voltage level)
  delay(500);
  digitalWrite(30, LOW);    // turn the LED on (HIGH is the
voltage level)
  delay(1000);
  digitalWrite(30, HIGH);    // turn the LED on (HIGH is the
voltage level)
  delay(500);
```

```
  digitalWrite(28, LOW);    // turn the LED on (HIGH is the
voltage level)
  delay(500000);
  digitalWrite(28, HIGH);    // turn the LED on (HIGH is the
voltage level)
  delay(500);

}
```

Appendix 3 – Steady State MC Code

Steady-state-mc.cpp

```
#define _CRT_SECURE_NO_WARNINGS

#include <stdio.h>
#include <vector>
#include <thread>
#include <time.h>
#include "simulate.h"

#include"steady-state-mc.h"


int main(void) {
	printf("-------------------------------------------------
----------\n");

	int seed[NUM_THREADS];
	Simulation sim[NUM_THREADS];
	std::vector<std::thread> threads;

	// decide how many threads to allocate
	printf("Hardware concurrency: %i\n",
std::thread::hardware_concurrency());
	printf("%i threads allocated to the simulation\n",
NUM_THREADS);

	// allocate a different seed for each thread, for random
number generation
	for (unsigned i = 0; i < NUM_THREADS; i++)
		seed[i] = i;

	// initialise the simulations
	for (unsigned i = 0; i < NUM_THREADS; i++)
		sim[i].Init();

	// time stamp the beginning of the simulation
	time_t startTime = time(NULL);
	printf("Launching the simulation on %s",
ctime(&startTime));

	// launch the simulation threads
	for (unsigned i = 0; i < NUM_THREADS; i++)
		threads.push_back(std::thread(std::ref(sim[i]),
NUM_PHOTON_BATCHES / NUM_THREADS, BATCH_SIZE, seed[i]));

	// wait for the simulation threads to finish
	for (unsigned i = 0; i < NUM_THREADS; i++)
		threads[i].join();
	time_t endTime = time(NULL);

	// time stamp the end of the simulation
```

```
      printf("Simulation complete on %s", ctime(&endTime));
      long elapsedTime = long(difftime(endTime, startTime));
      long elapsedMinutes = elapsedTime / 60;
      int elapsedSeconds = elapsedTime % 60;
      printf("%lim %lis elapsed\n", elapsedMinutes,
elapsedSeconds);

      // compute the simulation results
      Simulation::Bundle(sim, NUM_THREADS);

      printf("-------------------------------------------------
----------\n");

} // end main()


Photoprop.cpp
#include "photoprop.h"
#include <math.h>

#define PI  3.14159265359
#define PI2 6.28318530718
#define ONE_MINUS_COSZERO 1.0E-12

Photon::Photon(void) {
      this->x = 0.0;
      this->y = 0.0;
      this->z = 0.0;
      this->ux = 0.0;
      this->uy = 0.0;
      this->uz = 1.0;
      this->w = 1.0;
      this->path = 0.0;
}

void Photon::Isotropize(RandomGen &rg) {
      double costheta = 2.0*rg.Uniform() - 1.0;
      double sintheta = sqrt(1.0 - costheta * costheta);
      double psi = PI2*rg.Uniform();

      this->ux = sintheta * cos(psi);
      this->uy = sintheta * sin(psi);
      this->uz = costheta;
}

void Photon::Hop(double mua, double mus, RandomGen &rg)
{
      double rnd;
      while ((rnd = rg.Uniform()) <= 0);     // avoids rnd=0
      double s = -log(rnd) / (mua + mus);
      this->x += s * this->ux;
      this->y += s * this->uy;
      this->z += s * this->uz;
```

```
	this->path += s;
}

double Photon::Absorb(double mua, double mus, RandomGen & rg)
{
	double albedo = mus / (mua + mus);
	double loss = this->w * (1 - albedo);
	this->w -= loss;

	return loss;
}

void Photon::Spin(double mua, double mus, double g, RandomGen
& rg)
{
	// sample theta
	double cosTheta;
	if (g == 0.0)
		cosTheta = 2.0*rg.Uniform() - 1.0;
	else {
		double temp = (1.0 - g * g) / (1.0 - g + 2 * g *
rg.Uniform());
		cosTheta = (1.0 + g * g - temp * temp) / (2.0 * g);
	}
	double sinTheta = sqrt(1.0 - cosTheta * cosTheta);

	// sample psi
	double psi = PI2*rg.Uniform();
	double cosPsi = cos(psi);
	double sinPsi = sin(psi);

	// define new trajectory
	double uxx, uyy, uzz;
	if (1 - fabs(uz) <= ONE_MINUS_COSZERO) {
		uxx = sinTheta * cosPsi;
		uyy = sinTheta * sinPsi;
		uzz = copysign(cosTheta, this->uz);
	}
	else {
		double temp = sqrt(1.0 - uz * uz);
		uxx = sinTheta * (ux * uz * cosPsi - uy * sinPsi) /
temp + ux * cosTheta;
		uyy = sinTheta * (uy * uz * cosPsi + ux * sinPsi) /
temp + uy * cosTheta;
		uzz = -sinTheta * cosPsi * temp + uz * cosTheta;
	}
	this->ux = uxx;
	this->uy = uyy;
	this->uz = uzz;
}

void Photon::Roulette(double threshold, double probability,
RandomGen & rg)
```

```
{
      if (this->w < threshold) {
            if (rg.Uniform() < probability)
                  this->w /= probability;
            else
                  this->w = 0.0;
            }
}
```

Random.cpp

```
#include "random.h"


#define MBIG 1000000000
#define MSEED 161803398
#define MZ 0
#define FAC 1.0E-9

RandomGen::RandomGen(long seed) {
      this->Seed(seed);
}

void RandomGen::Seed(long seed) {

      long mj, mk;
      int i, ii;

      mj = MSEED - (seed < 0 ? -seed : seed);
      mj %= MBIG;
      ma[55] = mj;
      mk = 1;
      for (i = 1; i <= 54; i++) {
            ii = (21 * i) % 55;
            ma[ii] = mk;
            mk = mj - mk;
            if (mk < MZ)
                  mk += MBIG;
            mj = ma[ii];
      }
      for (ii = 1; ii <= 4; ii++)
            for (i = 1; i <= 55; i++) {
                  ma[i] -= ma[1 + (i + 30) % 55];
                  if (ma[i] < MZ)
                        ma[i] += MBIG;
            }
      i1 = 0;
      i2 = 31;

      return;
}

double RandomGen::Uniform(void) {
```

```
	int mj;

	if (++i1 == 56)
		i1 = 1;
	if (++i2 == 56)
		i2 = 1;
	mj = ma[i1] - ma[i2];
	if (mj < MZ)
		mj += MBIG;
	ma[i1] = mj;
	return (mj * FAC);
	}


Simulate.cpp
#define _CRT_SECURE_NO_WARNINGS

#include <math.h>
#include <stdio.h>
#include "photoprop.h"
#include "random.h"
#include "simulate.h"

void Simulation::operator()(unsigned long numPhotonBatches,
unsigned long batchSize, int uid) {

	// create the stats dump file
	FILE* stats;
	char fileName[80];

	sprintf(fileName, "%i.txt", uid);
	stats = fopen(fileName, "w+");

	// seed the random number generator on the unique thread
id
	RandomGen rg;
	rg.Seed(uid);

	// precompute useful constants
	double a2 = ELLIPSE_A * ELLIPSE_A;
	double b2 = ELLIPSE_B * ELLIPSE_B;
	double a2b2 = a2 * b2;

	// this is the actual simulation
	for (unsigned long m = 0; m < numPhotonBatches; m++) {
		// simulations are in batches of photons
		for (unsigned long i = 0; i < batchSize; i++) {
			Photon p;

			p.x = 0;
			p.y = 0;
			p.z = 0;
			p.w = 1;
```

```
                p.Isotropize(rg);

                while (p.w > 0) {
                     p.Hop(MU_A, MU_S, rg);

                     // check if the photon is outside an
elliptical cylinder body model
                     if ((a2*p.x*p.x + b2 * p.y*p.y) > a2b2)
{
                          if (rg.Uniform() < REFLECTIVITY)
                          {
                               double rnd;
                               while ((rnd = rg.Uniform())
<= 0);     // avoids rnd=0
                               double s = -log(rnd) / (MU_A
+ MU_S);
                               p.x = 0;
                               p.y = ELLIPSE_B - s;
                          }
                          else {
                               if (fabs(p.z) <=
DETECTOR_HALF_HEIGHT) {
                                    this->capturedPhotons++;
                                    this->signal += p.w;
                                    fprintf(stats, "%lf
%lf\n", p.w, p.path);
                               }
                               p.w = 0;
                          }
                          break;
                     }

                     p.Absorb(MU_A, MU_S, rg);

                     p.Spin(MU_A, MU_S, G, rg);

                     p.Roulette(ROULETTE_THRESHOLD,
ROULETTE_PROBABILITY, rg);
                }
           }
     }

     // normalise the signal
     this->signal /= (double) numPhotonBatches;
     this->signal /= (double) batchSize;

     // store the number of photon batches actually simulated
     simulatedPhotonBatches = numPhotonBatches;

     // close the stats file
     fclose(stats);
}
```

```
void Simulation::Init(void) {
	this->signal = 0;
	this->capturedPhotons = 0;
}



void Simulation::Bundle(Simulation * simvec, unsigned long
numSimulations)
{
	// accumulate the number of batches of photons actually
simulated
	unsigned long totalNumberOfBatches = 0;
	unsigned long photonsContributingToSignal = 0;
	double totalSignal = 0.0;


	for (unsigned i = 0; i < numSimulations; i++) {
		totalNumberOfBatches +=
simvec[i].simulatedPhotonBatches;
		photonsContributingToSignal +=
simvec[i].capturedPhotons;
		totalSignal += simvec[i].signal;
		printf("Simulation %u: signal = %le\n", i,
simvec[i].signal); // uncomment if individual signals are
needed
	}
	totalSignal /= (double)numSimulations;

	double totalDeviationSquared = 0.0;
	for (unsigned i = 0; i < numSimulations; i++) {
		totalDeviationSquared += (simvec[i].signal -
totalSignal) * (simvec[i].signal - totalSignal);
	}
	double standardDeviation = sqrt(totalDeviationSquared /
(numSimulations - 1));

	printf("%le photon packets contributed to the total
signal\n", (double)photonsContributingToSignal);
	printf("Total normalised signal: %le\n", totalSignal);
	printf("Standard deviation: %le\n", standardDeviation);
}
```

Appendix 4 – Time Resolved MC Code

Time-resolved-mc.cpp

```
#define _CRT_SECURE_NO_WARNINGS

#include <stdio.h>
#include <vector>
#include <thread>
#include <time.h>
#include "simulate.h"

#include"time-resolved-mc.h"



int main(void) {
	printf("-----------------------------------------------
----------\n");

	int seed[NUM_THREADS];
	Simulation sim[NUM_THREADS];
	std::vector<std::thread> threads;

	// decide how many threads to allocate
	printf("Hardware concurrency: %i\n",
std::thread::hardware_concurrency());
	printf("%i threads allocated to the simulation\n",
NUM_THREADS);

	// allocate a different seed for each thread, for random
number generation
	for (unsigned i = 0; i < NUM_THREADS; i++)
		seed[i] = i;

	// initialise the simulations
	for (unsigned i = 0; i < NUM_THREADS; i++)
		sim[i].Init();

	// time stamp the beginning of the simulation
	time_t startTime = time(NULL);
	printf("Launching the simulation on %s",
ctime(&startTime));

	// launch the simulation threads
	for (unsigned i = 0; i < NUM_THREADS; i++)
		threads.push_back(std::thread(std::ref(sim[i]),
NUM_PHOTON_BATCHES / NUM_THREADS, BATCH_SIZE, seed[i]));

	// wait for the simulation threads to finish
	for (unsigned i = 0; i < NUM_THREADS; i++)
		threads[i].join();
	time_t endTime = time(NULL);
```

```
      // time stamp the end of the simulation
      printf("Simulation complete on %s", ctime(&endTime));
      long elapsedTime = long(difftime(endTime, startTime));
      long elapsedMinutes = elapsedTime / 60;
      int elapsedSeconds = elapsedTime % 60;
      printf("%lim %lis elapsed\n", elapsedMinutes,
elapsedSeconds);

      // compute the simulation results
      Simulation::Bundle(sim, NUM_THREADS);

      printf("-----------------------------------------------
----------\n");

} // end main()


Photoprop.cpp
#include "photoprop.h"
#include <math.h>

#define PI  3.14159265359
#define PI2 6.28318530718
#define ONE_MINUS_COSZERO 1.0E-12

Photon::Photon(void) {
      this->x = 0.0;
      this->y = 0.0;
      this->z = 0.0;
      this->ux = 0.0;
      this->uy = 0.0;
      this->uz = 1.0;
      this->w = 1.0;
      this->path = 0.0;
}

void Photon::Isotropize(RandomGen &rg) {
      double costheta = 2.0*rg.Uniform() - 1.0;
      double sintheta = sqrt(1.0 - costheta * costheta);
      double psi = PI2*rg.Uniform();

      this->ux = sintheta * cos(psi);
      this->uy = sintheta * sin(psi);
      this->uz = costheta;
}

void Photon::Hop(double mua, double mus, RandomGen &rg)
{
      double rnd;
      while ((rnd = rg.Uniform()) <= 0);    // avoids rnd=0
      double s = -log(rnd) / (mua + mus);
      this->x += s * this->ux;
      this->y += s * this->uy;
```

```
	this->z += s * this->uz;
	this->path += s;
}

double Photon::Absorb(double mua, double mus, RandomGen & rg)
{
	double albedo = mus / (mua + mus);
	double loss = this->w * (1 - albedo);
	this->w -= loss;

	return loss;
}

void Photon::Spin(double mua, double mus, double g, RandomGen
& rg)
{
	// sample theta
	double cosTheta;
	if (g == 0.0)
		cosTheta = 2.0*rg.Uniform() - 1.0;
	else {
		double temp = (1.0 - g * g) / (1.0 - g + 2 * g *
rg.Uniform());
		cosTheta = (1.0 + g * g - temp * temp) / (2.0 * g);
	}
	double sinTheta = sqrt(1.0 - cosTheta * cosTheta);

	// sample psi
	double psi = PI2*rg.Uniform();
	double cosPsi = cos(psi);
	double sinPsi = sin(psi);

	// define new trajectory
	double uxx, uyy, uzz;
	if (1 - fabs(uz) <= ONE_MINUS_COSZERO) {
		uxx = sinTheta * cosPsi;
		uyy = sinTheta * sinPsi;
		uzz = copysign(cosTheta, this->uz);
	}
	else {
		double temp = sqrt(1.0 - uz * uz);
		uxx = sinTheta * (ux * uz * cosPsi - uy * sinPsi) /
temp + ux * cosTheta;
		uyy = sinTheta * (uy * uz * cosPsi + ux * sinPsi) /
temp + uy * cosTheta;
		uzz = -sinTheta * cosPsi * temp + uz * cosTheta;
	}
	this->ux = uxx;
	this->uy = uyy;
	this->uz = uzz;
}
```

```
void Photon::Roulette(double threshold, double probability,
RandomGen & rg)
{
      if (this->w < threshold) {
            if (rg.Uniform() < probability)
                  this->w /= probability;
            else
                  this->w = 0.0;
            }
}


Random.cpp
#include "random.h"


#define MBIG 1000000000
#define MSEED 161803398
#define MZ 0
#define FAC 1.0E-9

RandomGen::RandomGen(long seed) {
      this->Seed(seed);
}

void RandomGen::Seed(long seed) {

      long mj, mk;
      int i, ii;

      mj = MSEED - (seed < 0 ? -seed : seed);
      mj %= MBIG;
      ma[55] = mj;
      mk = 1;
      for (i = 1; i <= 54; i++) {
            ii = (21 * i) % 55;
            ma[ii] = mk;
            mk = mj - mk;
            if (mk < MZ)
                  mk += MBIG;
            mj = ma[ii];
      }
      for (ii = 1; ii <= 4; ii++)
            for (i = 1; i <= 55; i++) {
                  ma[i] -= ma[1 + (i + 30) % 55];
                  if (ma[i] < MZ)
                        ma[i] += MBIG;
            }
      i1 = 0;
      i2 = 31;

      return;
}
```

```
double RandomGen::Uniform(void) {

      int mj;

      if (++i1 == 56)
            i1 = 1;
      if (++i2 == 56)
            i2 = 1;
      mj = ma[i1] - ma[i2];
      if (mj < MZ)
            mj += MBIG;
      ma[i1] = mj;
      return (mj * FAC);
      }


Simulate.cpp
#define _CRT_SECURE_NO_WARNINGS

#include <math.h>
#include <stdio.h>
#include "photoprop.h"
#include "random.h"
#include "simulate.h"

void Simulation::operator()(unsigned long numPhotonBatches,
unsigned long batchSize, int uid) {

      // create the stats dump file
      FILE* stats;
      char fileName[80];

      sprintf(fileName, "%i.txt", uid);
      stats = fopen(fileName, "w+");

      // seed the random number generator on the unique thread
id
      RandomGen rg;
      rg.Seed(uid);

      // precompute useful constants
      double a2 = ELLIPSE_A * ELLIPSE_A;
      double b2 = ELLIPSE_B * ELLIPSE_B;
      double a2b2 = a2 * b2;

      // this is the actual simulation
      for (unsigned long m = 0; m < numPhotonBatches; m++) {
            // simulations are in batches of photons
            for (unsigned long i = 0; i < batchSize; i++) {
                  Photon p;

                  p.x = 0;
```

```
                p.y = 0;
                p.z = 0;
                p.w = 1;

                p.Isotropize(rg);

                while (p.w > 0) {
                     p.Hop(MU_A, MU_S, rg);

                     // check if the photon is outside an
elliptical cylinder body model
                     if ((a2*p.x*p.x + b2 * p.y*p.y) > a2b2)
{
                          if (fabs(p.z) <=
DETECTOR_HALF_HEIGHT) {
                               this->capturedPhotons++;
                               this->signal += p.w;
                               fprintf(stats, "%lf %lf\n",
p.w, p.path);
                          }
                          p.w = 0;
                          break;
                     }

                     p.Absorb(MU_A, MU_S, rg);

                     p.Spin(MU_A, MU_S, G, rg);

                     p.Roulette(ROULETTE_THRESHOLD,
ROULETTE_PROBABILITY, rg);
                }
           }
     }

     // normalise the signal
     this->signal /= (double) numPhotonBatches;
     this->signal /= (double) batchSize;

     // store the number of photon batches actually simulated
     simulatedPhotonBatches = numPhotonBatches;

     // close the stats file
     fclose(stats);
}



void Simulation::Init(void) {
     this->signal = 0;
     this->capturedPhotons = 0;
}
```

```
void Simulation::Bundle(Simulation * simvec, unsigned long
numSimulations)
{
	// accumulate the number of batches of photons actually
simulated
	unsigned long totalNumberOfBatches = 0;
	unsigned long photonsContributingToSignal = 0;
	double totalSignal = 0.0;


	for (unsigned i = 0; i < numSimulations; i++) {
		totalNumberOfBatches +=
simvec[i].simulatedPhotonBatches;
		photonsContributingToSignal +=
simvec[i].capturedPhotons;
		totalSignal += simvec[i].signal;
		printf("Simulation %u: signal = %le\n", i,
simvec[i].signal); // uncomment if individual signals are
needed
	}
	totalSignal /= (double)numSimulations;

	double totalDeviationSquared = 0.0;
	for (unsigned i = 0; i < numSimulations; i++) {
		totalDeviationSquared += (simvec[i].signal -
totalSignal) * (simvec[i].signal - totalSignal);
	}
	double standardDeviation = sqrt(totalDeviationSquared /
(numSimulations - 1));

	printf("%le photon packets contributed to the total
signal\n", (double)photonsContributingToSignal);
	printf("Total normalised signal: %le\n", totalSignal);
	printf("Standard deviation: %le\n", standardDeviation);
}
```

Appendix 5 – Code to drive my transmitter.

```
from machine import Pin
from rp2 import PIO, StateMachine, asm_pio
import utime

FiveVolt1=Pin(4, Pin.OUT)
FiveVolt2=Pin(5, Pin.OUT)
FiveVolt3=Pin(6, Pin.OUT)
FiveVolt4=Pin(7, Pin.OUT)

FiveVolt1.low()
FiveVolt2.low()
FiveVolt3.low()
FiveVolt4.low()

@asm_pio(set_init=PIO.OUT_LOW)\


def square():
    wrap_target()
    set(pins, 1)
    set(pins, 0)
    wrap()


sm     =     rp2.StateMachine(0,     square,     freq=1000000,
set_base=Pin(21))
sm.active(1)

#sm2     =     rp2.StateMachine(0,     square,     freq=1000000,
set_base=Pin(22)) # to synchronise signal
#sm2.active(1)

FiveVolt1.high()
FiveVolt2.high()
FiveVolt3.high()
FiveVolt4.high()
#utime.sleep(100)
#FiveVolt1.low()
#FiveVolt2.low()
#FiveVolt3.low()
#FiveVolt4.low()
#utime.sleep(100)
```

Appendix 6 – Code to convert endoscopic videos into bitstream and add noise to them.

```
#pragma warning(disable : 4996)

#include <opencv2/core/core.hpp>
#include <opencv2/highgui/highgui.hpp>
#include <opencv2/imgproc/imgproc.hpp>
#include <opencv2/calib3d/calib3d.hpp>
#include <chrono>
#include <cstdlib>

#define VIDEO_IN "c:\\io\\in.avi"
#define VIDEO_OUT "c:\\io\\out.avi"
#define VIDEO_IMG "c:\\io\\out.jpg"

#define BER 0.1
#define MAX_FRAMES 150

double dRand(void)
{
	return (double)rand() / (double)RAND_MAX;
}


int main(void)
{
	// buffers

	cv::Mat rawFrame;
	cv::Mat slicedFrame;
	char s[1000];
	cv::Vec3b pixel;
	int r, g, b;

	cv::waitKey(50);


	// Say hello

	printf("Hello\n");

	// open input video

	cv::VideoCapture inVideo(VIDEO_IN);

	// open output video

	// possible codecs: FFV1, MJLS (slow), 0 (raw,fast)
DIVX, DX50, WMV2, DIV2, MPG3 (fast & compact)
	sprintf(s, VIDEO_OUT);
```

```
	//cv::VideoWriter outVideo(s, CV_FOURCC('M', 'P', 'G',
'3'), (double)25.0, cv::Size(512, 512), true);;
	cv::VideoWriter outVideo(s, 0, (double)25.0,
cv::Size(512, 512), true);;


	printf("Slicing");

	int dly = 0;

	while (true)
	{
		// read frame from input video. Exit loop if no
more frames to read.

		if (!inVideo.read(rawFrame)) break;
		if (dly++ == MAX_FRAMES) break;

		// slice frame

		slicedFrame = rawFrame(cv::Rect(32, 32, 512, 512));

		// add noise

		int x, y;
		for (x=0; x<512; x++)
			for (y = 0; y < 512; y++)
			{
				// extract the pixel

				pixel = slicedFrame.at<cv::Vec3b>(y, x);
				b = pixel.val[0];
				g = pixel.val[1];
				r = pixel.val[2];

				// add bit errors

				if (dRand() <= BER) b = b ^ 0x01;
				if (dRand() <= BER) b = b ^ 0x02;
				if (dRand() <= BER) b = b ^ 0x04;
				if (dRand() <= BER) b = b ^ 0x08;
				if (dRand() <= BER) b = b ^ 0x10;
				if (dRand() <= BER) b = b ^ 0x20;
				if (dRand() <= BER) b = b ^ 0x40;
				if (dRand() <= BER) b = b ^ 0x80;

				if (dRand() <= BER) g = g ^ 0x01;
				if (dRand() <= BER) g = g ^ 0x02;
				if (dRand() <= BER) g = g ^ 0x04;
				if (dRand() <= BER) g = g ^ 0x08;
				if (dRand() <= BER) g = g ^ 0x10;
				if (dRand() <= BER) g = g ^ 0x20;
				if (dRand() <= BER) g = g ^ 0x40;
```

```
                        if (dRand() <= BER) g = g ^ 0x80;

                        if (dRand() <= BER) r = r ^ 0x01;
                        if (dRand() <= BER) r = r ^ 0x02;
                        if (dRand() <= BER) r = r ^ 0x04;
                        if (dRand() <= BER) r = r ^ 0x08;
                        if (dRand() <= BER) r = r ^ 0x10;
                        if (dRand() <= BER) r = r ^ 0x20;
                        if (dRand() <= BER) r = r ^ 0x40;
                        if (dRand() <= BER) r = r ^ 0x80;


                        // write back the pixel

                        slicedFrame.at<cv::Vec3b>(y, x) =
cv::Vec3b(b, g, r);
                }

            // write frame to output video

            outVideo.write(slicedFrame);
            printf(".");
      }

      inVideo.release();


      return outVideo.release();

      printf("done\n");


0;

}
```

Appendix 7 – Code to recover the clock and decode bits into an image.

Decoder.cpp

```
#include <iostream>
#include <fstream>
#include <string>
#include <vector>
#include <algorithm>
#include <numeric>
#include <cmath>
#include "utilities.h"


using namespace std;


int main(int argc, char* argv[])
{
    ///// Display a help message if the number of parameters
is wrong /////
    if (argc != 4) {
        cout << "Usage: decode <input file> <output file>
<configuration file>" << endl;
    }


    ///// Start the programme /////
    Utilities::Timer timer;
    cout << "Program starting on " << __DATE__ << " at " <<
__TIME__ << endl;
    cout << "System MAX_SIZE (maximum length of trace): " <<
SIZE_MAX << endl << endl;
    cout << "Reading " << argv[1] << " to generate " <<
argv[2] << " using configuration " << argv[3] << endl << endl;


    ///// Read the configuration /////
    cout << "Reading the configuration... ";

    string inputFileName = argv[1];
    string outputFileName = argv[2];
    string configurationFileName = argv[3];

    ConfigurationParser cp(configurationFileName, "=", '#');
    int numberOfHeaderLines = cp.GetInt("HEADER_LINES");
    int dataColumNumber = cp.GetInt("DATA_COLUMN");
    int separatorIndex = cp.GetInt("SEPARATOR");
    long baselineWindow = cp.GetLong("BASELINE_WINDOW");
    double noiseMargin = cp.GetFloat("NOISE_MARGIN");
    bool activeHigh = cp.GetBool("ACTIVE_SIGNAL");
    int leadingZeros = cp.GetInt("LEADING_ZEROS");
    double samplingTime = cp.GetFloat("SAMPLING_TIME");
```

```
    double bitRate = cp.GetFloat("BIT_RATE");
    long frameSize = cp.GetLong("FRAME_SIZE");
    string headerFileName = cp.GetString("HEADER_FILE");
    string separator;
    switch (separatorIndex) {
    case 0:
        separator = ",";
        break;
    case 1:
        separator = "\t";
        break;
    default:
        cerr << "Configuration error: invalid SEPARATOR" <<
endl;
        abort();
    }
    cout << " Done." << endl;


    ///// Read the trace /////
    cout << "Reading the trace... " << endl;
    ifstream inputFile(inputFileName);
    vector<double> trace;
    int lineNumber = 0;
    for (string line; getline(inputFile, line);) {
        lineNumber++;
        if (lineNumber > numberOfHeaderLines) {
            // Remove any separators from columns
            for (int i = 2; i < dataColumNumber; i++) {
                size_t separatorPosition =
line.find(separator);
                line[separatorPosition] = '0';
            }
            size_t separatorPosition = line.find(separator);

            // Do not add eventual empty lines at the end.
            if (separatorPosition != string::npos) {

trace.push_back(stod(line.substr(separatorPosition +
separator.length(), string::npos)));
            }
        }
    }
    inputFile.close();
    cout << "    " << lineNumber << " lines read." << endl;


    ///// Here begins the actual reconstruction of the frame
/////
    cout << "Identifying the start of the frame... " << endl;
```

```
    ///// Determine the minimum and the maximum of the trace
(noise) in the baseline window /////
    double noiseMinimum = *min_element(trace.begin(),
trace.begin() + baselineWindow);
    cout << "    Noise minimum: " << noiseMinimum << endl;
    double noiseMaximum = *max_element(trace.begin(),
trace.begin() + baselineWindow);
    cout << "    Noise maximum: " << noiseMaximum << endl;


    ///// Expand the noise extrema by the noise margin /////
    double noiseCentre = (noiseMinimum + noiseMaximum) / 2.0;
    noiseMinimum = noiseCentre + (noiseMinimum - noiseCentre)
* noiseMargin;
    noiseMaximum = noiseCentre + (noiseMaximum - noiseCentre)
* noiseMargin;


    ///// When the trace jumps out of the expanded noise
extrema, this is the start of the frame. /////
    size_t startOfFrame = 0;
    while (startOfFrame < trace.size()) {
        if (trace[startOfFrame] < noiseMinimum) break;
        if (trace[startOfFrame] > noiseMaximum) break;
        startOfFrame++;
    }
    cout << "    Start of the frame identified at point " <<
startOfFrame << "." << endl;


    ///// Slice the trace from the beginning of the frame.
/////
    cout << "Slicing the trace at the start of the frame..."
<< endl;
    vector<double> frameTrace(trace.begin() + startOfFrame,
trace.end());
    cout << "    Done." << endl;


    ///// Determine an adaptive threshold by averaging the
trace over a sliding window, and binarise by comparing with
the threshold.                                          /////
    cout << "Binarising the frame..." << endl;
    vector<int> binaryTrace;
    for (size_t i = 0; i < (frameTrace.size() -
baselineWindow); i++) {
        double threshold = accumulate(frameTrace.begin() + i,
frameTrace.begin() + i + baselineWindow, 0.0) /
baselineWindow;
        bool bit = (frameTrace[i] > threshold);
        if (!activeHigh)
            bit = !bit;
        if (bit)
```

```
            binaryTrace.push_back(1);
        else
            binaryTrace.push_back(0);
    }
    cout << "    Done." << endl;


    ///// Compute the bitstream by checking the average bit
value where bits are expected from the data rate timing. /////
    cout << "Computing the bitstream..." << endl;
    double pointsPerBitExact = 1000000.0 / (samplingTime *
bitRate);
    int pointsPerBitRounded = (int)round(pointsPerBitExact);
    vector<bool> bitstream;
    for (size_t i = 0; i < leadingZeros; i++) {
        bitstream.push_back(false);
    }
    for (size_t i = 0; i < (8 * frameSize) - leadingZeros;
i++) {
        size_t seekIndex = (size_t)(i * pointsPerBitExact);
        double bitSignal = accumulate(binaryTrace.begin() +
seekIndex, binaryTrace.begin() + seekIndex +
pointsPerBitRounded, 0.0) / pointsPerBitRounded;
        bitstream.push_back(bitSignal > 0.5);
    }
    cout << "    Done." << endl;


    ///// Compute the output file. /////
    cout << "Creating the output file..." << endl;
    ofstream outputFile(outputFileName, ios::binary);
    long byteCount = 0;

    // Copy the header from the header file.
    ifstream headerFile(headerFileName, ios::binary);
    for (char b; headerFile.read(&b, 1);) {
        outputFile.write(&b, 1);
        byteCount++;
    }
    headerFile.close();

    // Build the bytestream from the bitstream.
    for (long i = byteCount * 8; i < bitstream.size(); i += 8)
{
        char b = 0;
        b += 128 * bitstream[i];
        b += 64 * bitstream[i + 1];
        b += 32 * bitstream[i + 2];
        b += 16 * bitstream[i + 3];
        b += 8 * bitstream[i + 4];
        b += 4 * bitstream[i + 5];
        b += 2 * bitstream[i + 6];
        b += 1 * bitstream[i + 7];
```

```
        outputFile.write(&b, 1);
        byteCount++;
    }

    outputFile.close();
    cout << "    Done." << endl << endl;


    ///// End messages /////
    cout << byteCount << " bytes written to " <<
outputFileName << "." << endl;
    cout << "Finished in " << timer.MillisecondsElapsed()  <<
" milliseconds." << endl << endl;
}
```

Utilities.cpp

```
#include "utilities.h"
#include <regex>
#include <iostream>
#include <vector>
#include <fstream>



using namespace std;


// String utilities

string Utilities::Ltrim(const string& s) {
     return regex_replace(s, regex("^\\s+"), string(""));
}

string Utilities::Rtrim(const string& s) {
     return regex_replace(s, regex("\\s+$"), string(""));
}

string Utilities::Trim(const string& s) {
     using namespace Utilities;
     return Ltrim(Rtrim(s));
     }


// Timer utilities

Utilities::Timer::Timer() {
     Utilities::Timer::Reset();
}

void Utilities::Timer::Reset() {
     _startTimePoint = chrono::high_resolution_clock::now();
}
```

```
double Utilities::Timer::MillisecondsElapsed() const {
      std::chrono::time_point<std::chrono::high_resolution_clo
ck> endTimePoint = chrono::high_resolution_clock::now();
      std::chrono::duration<double, std::milli> milliseconds =
endTimePoint - _startTimePoint;
      return milliseconds.count();
     }


// Configuration utilities

ConfigurationParser::ConfigurationParser(const string
fileName, const string delimiterString, const char commentTag)
{
      ifstream configurationFile(fileName);
      _delimiter = delimiterString;
      _commentTag = commentTag;

      while (!configurationFile.eof()) {
            string line;
            getline(configurationFile, line);

            // Ignore the comments.
            if (line[0] == _commentTag) continue;

            size_t delimiterPosition =
line.find(delimiterString);

            // Ignore lines without delimiters
            if (delimiterPosition == string::npos) continue;

            string key = Utilities::Trim(line.substr(0,
delimiterPosition));
            string value =
Utilities::Trim(line.substr(delimiterPosition +
_delimiter.length(), string::npos));
            if (key == "") continue;
            _configuration.insert_or_assign(key, value);
      }
      configurationFile.close();
}


int ConfigurationParser::GetInt(const string key) {
      string valueString = _configuration.at(key);
      return stoi(valueString);
}


long ConfigurationParser::GetLong(const string key) {
      string valueString = _configuration.at(key);
      return stol(valueString);
}
```

```
float ConfigurationParser::GetFloat(const string key) {
	string valueString = _configuration.at(key);
	return stof(valueString);
}


string ConfigurationParser::GetString(const string key) {
	string valueString = _configuration.at(key);
	return valueString;
}


bool ConfigurationParser::GetBool(const string key) {
	string valueString = _configuration.at(key);

	vector<string> t{ "1", "T", "t", "TRUE", "true", "True",
"H", "h" };
	if (find(begin(t), end(t), valueString) != end(t))
		return true;
	else
		return false;
}
```